Optimized discharge excitation techniques for short pulse gas lasers: TEA CO_2 laser

by

Farooq Kyeyune

Thesis presented in partial fulfilment of the requirements for the degree of ***Master of Science*** *at the University of Stellenbosch*

Departement of Physics,
University of Stellenbosch,
Private Bag X1, Matieland 7602, South Africa.

Supervisors:

Prof. Hubertus M. von Bergmann
Prof. Erich G. Rohwer

December 2013

Stellenbosch University http://scholar.sun.ac.za

Declaration

By submitting this thesis electronically, I declare that the entirety of the work contained therein is my own, original work, that I am the sole author thereof (save to the extent explicitly otherwise stated), that reproduction and publication thereof by Stellenbosch University will not infringe any third party rights and that I have not previously in its entirety or in part submitted it for obtaining any qualification.

Date: December 2013 .....

Copyright © 2013 Stellenbosch University
All rights reserved.

Stellenbosch University http://scholar.sun.ac.za

Abstract

Optimized discharge excitation techniques for short pulse gas lasers: TEA CO_2 laser

F. Kyeyune

Departement of Physics,
University of Stellenbosch,
Private Bag X1, Matieland 7602, South Africa.

Thesis: MSc

December 2013

Transversely excited atmospheric (TEA) CO_2 lasers have found numerous established and potential applications in both industry and research. However, the development of laser systems which can meet the demands of these applications is usually hampered by two key issues: the excitation circuit and the method of preionization. For example, the conventional thyratron-based exciters can no longer meet the requirements in high repetition rate applications. Therefore, new technologies and improved excitation techniques should be developed. In this thesis the development of an efficient all solid-state switched exciter for pumping a TEA CO_2 laser and the evaluation of a miniature TEA CO_2 laser preionized by corona discharge are presented. The excitation circuit consists of an insulated gate bipolar transistor (IGBT) as the primary switch, two stages of magnetic pulse compression (MPC) and a fast pulse transformer. Three magnetic core candidates that can be used in the MPC network and the pulse transformer were experimentally investigated. Fe-based nanocrystalline ferromagnetic material, FINEMET was found to have the best properties for the current application and was subsequently used in the development of the exciter. A surface-wire corona preionized miniature TEA CO_2 laser was evaluated and the results were compared to those of an earlier spark array preionized laser. The corona preionizer was constructed from a ceramic tube (Al_2O_3) and a fine wire stretched along the surface of the tube. When this extremely efficient yet comparatively inexpensive preionizer was applied to the laser, output pulse energy of 230 mJ with pulse duration of FWHM $\sim$ 70 ns was obtained from a small discharge volume of 50 cm^3. This energy output was found to be higher than that obtained from a spark preionized laser with the same discharge volume. Moreover the discharge stability was also found to improve drastically. These results can therefore be used as a reference when developing full scale corona preionized laser systems.

Stellenbosch University http://scholar.sun.ac.za

Uittreksel

Geoptimeerde opwekkingstegnieke deur ontlading vir kort puls gas lasers: TOA CO_2 laser

F. Kyeyune

Departement Fisika,
Universiteit van Stellenbosch,
Privaatsak X1, Matieland 7602, Suid Afrika.

Tesis: MSc

Desember 2013

Transversaal opgewekte atmosferiese (TOA) CO_2 lasers het breë toepassing in industrie en-navorsing en toon baie potensiaal. Die gebruik van hierdie lasers word egter ingeperk deur twee kern probleme: die opwekkingstroombaan en die metode waarmee die lasermedium vooraf geïoniseer word. Byvoorbeeld kan die algemene "thyratron" gebaseerde opwekkers nie byhou wanneer die herhalingstempo te hoog raak nie. Sodoende is daar 'n behoefte vir die ontwikkeling van nuwe tegnologie en beter opwekkingstegnieke. In hierdie tesis word die ontwikkeling van 'n effektiewe opwekker, met slegs vaste toetstand skakelaars, vir 'n TOA CO_2, asook die evaluering van 'n miniatuur TOA CO_2 laser wat met 'n vooraf geïoniseer word deur 'n korona ontlading voorgelê. Die opwekkerstroombaan bestaan uit 'n geïnsuleerde hek bipolêre transistor (IHBT) as die primêre skakelaar, twee vlakke van magnetiese puls kompressie (MPK) en 'n vinnige puls transformator. Drie tipes magnetiese kerne wat gebruik kan word in die MPK netwerk en die transformator is eksperimenteel ondersoek. Die yster gebaseerde nanokristalyne ferromagnetiese materiaal, FINEMET het die beste eienskappe getoon vir hierdie toepassing en is gevolglik gebruik in die ontwikkeling van die opwekker. 'n Miniatuur TOA CO_2 laser met 'n oppervlak-geleier korona vir vooraf ionisasie is ondersoek en die resultate is vergelyk met die van 'n vorige TOA CO_2 sisteem wat werk met 'n reeks vonkgapings vir vooraf ionisasie. Die korona vooraf ionisasie sisteem bestaan uit 'n keramiek buis (Al_2O_3) en 'n fyn geleier wat gespan is oor die oppervlak van die buis. Wanneer hierdie hoogs effektiewe dog eenvoudige vroeë ioniseerder aangewend word het ons puls energieë gemeet van 230 mJ met 'n pulslengte van ~ 70 ns uit 'n ontladings volume van 50 cm^3. Ons het bevind dat hierdie energie hoër is as die energie verkrygbaar vanaf die laser met dieselfde ontladings volume wat die vonkgapings gebruik vir vooraf ioniseering . Verder is bevind dat die ontladingstabiliteit drasties beter was. Hierdie resultate kan vervolgens gebruik word as 'n verwysing wanner volskaal laser sisteme met korona vooraf ionisasie ontwikkel word.

Stellenbosch University http://scholar.sun.ac.za

Acknowledgements

All praise is for **Allah**, the Exalted, without whom the completion of this work would have not been possible.

Certainly, I owe an enormous depth of gratitude and appreciation to my supervisor Prof. Hubertus M. von Bergmann, for his guidance, support and patience during my study.

To my co-supervisor, Prof. Erich G. Rohwer, I wish to express my sincere appreciation for his advice and financial support.

I would also like to thank all the colleagues at the LRI for their help and friendship.

Lastly, I would like to thank all my friends who have been there for me during my stay in South Africa. To you all, I owe you my sincerest and most heartfelt thanks.

Stellenbosch University http://scholar.sun.ac.za

Dedications

This thesis is dedicated to my family.

Stellenbosch University http://scholar.sun.ac.za

Contents

Stellenbosch University http://scholar.sun.ac.za

Stellenbosch University http://scholar.sun.ac.za

List of Figures

Stellenbosch University http://scholar.sun.ac.za

Stellenbosch University http://scholar.sun.ac.za

Stellenbosch University http://scholar.sun.ac.za

Stellenbosch University http://scholar.sun.ac.za

List of Tables

Stellenbosch University http://scholar.sun.ac.za

Chapter 1

Introduction

This chapter describes the theoretical background of transversely excited atmospheric (TEA) CO_2 lasers from which the motivation of this study has been derived. In the ensuing sections, the main objectives and organization of the thesis are outlined.

1.1 General introduction

The TEA CO_2 laser is a gas laser pumped by an electrical discharge operating in the pulsed mode. The electrical discharge is produced between a pair of parallel electrodes mounted in line with the optical axis of the laser. The discharge is initiated at an operating pressure equal to or more than one atmosphere by a fast rising high-voltage pulse. This type of laser is capable of producing extremely high peak power (several megawatts), high pulse energy (as high as hundred joules per pulse), wide wavelength range (9.35 to 10.85 μm in the infrared region) and high energy conversion efficiency (more than 10% for some systems). The operation of a TEA CO_2 laser was first demonstrated by a Canadian scientist Beaulieu [1] using a $He-CO_2-N_2$ gas mixture at atmospheric pressure. The action of the laser is based on the transitions that occur between the low-lying vibrational-rotational levels of the ground electronic $^1\Sigma$ state of the CO_2 molecule. The nitrogen gas in the mixture improves the pumping efficiency of the laser through collisional energy transfer from the excited N_2 molecules to the upper level CO_2 molecules. Helium gas extends the glow-to-arc transition time and effectively cools down the hot laser gas components.

Today, because of their capacity to produce high energy and high peak power output, TEA CO_2 lasers have numerous established and potential applications in science, industry and medicine. These applications include: laser-induced plasma source on solid targets [2, 3, 4], molecular laser isotope separation [5], optical pumping of molecular gas lasers [6], remote sensing and meteorology [7], non-destructive testing and characterization of composite materials used in the aerospace industry [8, 9], laser plasma extreme ultraviolet generation (EUV) for semiconductor photo-lithography [10, 11], paint removal and laser marking [12], laser skin resurfacing [13], etc. To realize each of these applications, a reliable, efficient and high repetition rate laser system capable of operating for long periods of time is required. The development of such systems has been pursued for many years. The extensively studied areas on a TEA CO_2 laser are the laser discharge unit and the pulsed power supply for exciting the laser.

Stellenbosch University http://scholar.sun.ac.za

The laser discharge unit consists of an uniform field discharge electrode structure, gas flow loop and preionizer. The discharge electrode structure [14, 15] is responsible for generating a uniform field distribution across the active volume. This is necessary to produce a uniform glow discharge. The function of the preionizer is to create a suitable initial electron density of $\sim 10^5 \text{cm}^{-3}$. The electrons have to be uniformly distributed over the entire discharge volume prior to the initiation of the main discharge to avoid the glow-to-arc transition and ensure a homogeneous glow discharge of the laser.

In order to obtain high quality and reliable performance of a TEA CO_2 laser, an efficient pulsed power supply is needed. The pulsed power supply should be capable of generating fast-rising and stable high-peak voltage pulses [16]. Depending on the laser gas mixture, pressure and inter-electrode separation, the peak voltage can be as high as 50 kV with a required voltage rise time between 100 and 150 ns and peak currents of tens of kA. In its simplest form, the power supply consists of a storage capacitor bank which is commonly charged by a DC high-voltage power supply. The energy stored in the capacitor bank is transferred by a fast high voltage and high current switch to the peaking capacitor usually connected directly to the discharge electrodes, and from there into the laser discharge. The main challenge of designing such high-voltage power supplies is choosing an efficient switch which can operate at the required high voltage and current. The switch has to fulfil both long-term reliability as well as high repetition rate operation. In addition, other factors such as capital investment and availability have also to be considered. To this end, spark gaps have been used as high voltage switches because of their cost effectiveness and capability to handle very high peak currents and high rates of rise of current [16]. Their main disadvantage, however, is limited lifetime especially at high repetition rate. Thyratron switches seemed promising because of their capacity to operate at high repetition rate and high voltage. Nevertheless, they are expensive and have limited lifetime as well due to electrode erosion and fill gas degradation.

Tremendous efforts have been devoted to extending the lifetime of spark gaps and thyratrons in high repetition rate TEA CO_2 lasers. This is evident from the number of reports in the literature in which different circuit topologies have been utilized, notably [17, 18, 19, 20]. On the other hand, the development of semiconductor switches in conjunction with magnetic pulse compression (MPC) networks has facilitated the use of all solid-state switching technology (ASST) in gas discharge lasers in general. Due to their practically unlimited lifetime and reliable operation, ASST is already quite matured and has been investigated in the past years as a potential replacement for the thyratron and spark gap-driven exciters [20, 21, 22]. However, no semiconductor switch is able yet to withstand the required high voltage and peak current as well as high rate of current rise. This therefore, necessitates new strategies in which the advantages of semiconductor switches can be fully exploited. One way to do this is by use of a fast step-up pulse transformer together with a magnetic pulse compression network as will be presented in this thesis.

Stellenbosch University http://scholar.sun.ac.za

1.2 Aim of the thesis

The main aims or objectives of this study are to:

- *Study the novel discharge stabilization techniques in TEA CO_2 lasers.*
- *Evaluate and compare different circuit topologies capable of generating fast rising high-voltage pulses.*
- *Measure the dynamic magnetic properties of ferromagnetic core materials suitable for constructing magnetic pulse compression networks.*
- *Characterize the performance and operating conditions of the pulsed power supply for pumping a TEA CO_2 laser.*
- *Evaluate the performance of a mini TEA CO_2 laser preionized by surface wire corona discharge.*

1.3 Outline of the thesis

This thesis has been organised as follows: In the following **Chapter 2**, the key issues associated with the development of stable glow discharges in TEA CO_2 lasers are discussed. The circuit topologies capable of generating fast rising high-voltage pulses required for the excitation of gas lasers are evaluated and compared in **Chapter 3**. In addition, a magnetic core volume optimization strategy for designing efficient magnetic pulse compression networks is presented. To design an optimised pulsing circuit, magnetic core materials with desirable characteristics are required. Three magnetic core materials which can be used in magnetic pulse compressor networks have been studied. The experimental setup and procedures, results and discussion are given in **Chapter 4**. The design outline of an efficient all-solid-state switched pulsed power supply for exciting a TEA CO_2 laser is developed in **Chapter 5**. The measurements (and discussion) of the pulsed power supply and its characterisation with the laser head are also provided in this chapter. In **Chapter 6**, we describe the experimental evaluation of a mini TEA CO_2 laser preionized by surface-wire corona discharge. The output measurements of the laser and discussion of the results are presented in this chapter. Lastly, the main conclusion of the thesis is given in **Chapter 7**.

Stellenbosch University http://scholar.sun.ac.za

Chapter 2

Discharge stability in TEA CO_2 lasers

2.1 Introduction

For an efficient operation of Transversely Excited (TE) gas discharge lasers, the laser is required to operate in a stable glow discharge mode [23, 24]. However, at high gas pressures (close to 1 atm and above), the glow discharge is unstable and thus develops into arcs after a short time. This behaviour is undesirable as it results in inefficient energy transfer into the laser discharge and potential damage of the system components. A stable glow discharge at high gas pressure can be achieved by introducing a uniformly distributed electron density throughout the discharge volume prior to the initiation of the main discharge [24]. This process is called preionization and can be accomplished in a number of ways. In this chapter, we will discuss the key issues associated with the glow discharge development in high pressure gas lasers. The commonly employed preionization techniques in TEA CO_2 lasers in particular are also addressed.

2.2 Electric breakdown in gases

Electric breakdown refers to the process of converting a non-conducting medium to a conducting one by applying a sufficiently strong electric field to it [25]. The primary process starts with the formation of an electron avalanche. An avalanche is the multiplication of the primary seed electrons that may be introduced between a pair of parallel electrodes. The seed electrons can be produced through external effects such as photoelectric effect or cosmic radiation. For example, the medium or the cathode may be illuminated with uv radiation to produce photoelectrons [25]. Figure 2.1 shows a schematic diagram illustrating the formation of an electron avalanche initiated by a single electron. In the figure, the electron is accelerated by an electric field towards the anode. When the electron gains energy higher than the ionization potential, it ionizes a gas atom through inelastic collision, thereby giving rise to two electrons and an ion. The two electrons are again accelerated by the field, each ionizing a gas atom, resulting in four electrons and two ions. The process continues until the gas breakdown takes place, which is characterized by a light flash. Gas breakdown depends on a number of factors such as gas pressure and composition, inter-electrode separation, electrode profile, etc. Generally, the gas breakdown at moderate to high gas pressures can occur by two mechanisms, namely: Townsend (or Paschen) breakdown and streamer breakdown.

Stellenbosch University http://scholar.sun.ac.za

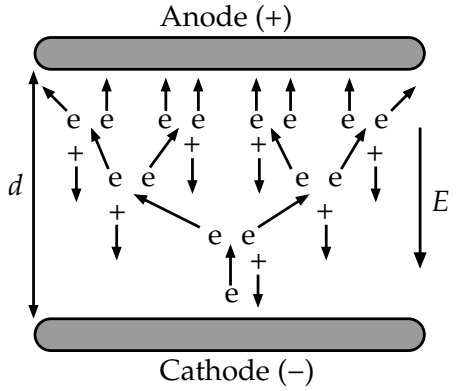

Figure 2.1: *Illustration of electron-ion multiplication resulting in an electron avalanche formation: where d is the inter-electrode separation and E is the electric field.*

2.2.1 Townsend breakdown

The discharge mechanism which takes place at low values of the product of pressure and inter-electrode separation is known as Townsend [24]. Its occurrence is explained as follows: consider two parallel electrodes separated by a distance d (see Figure 2.1). When a DC voltage is applied to the electrodes, an electric field $E = V/d$ is generated. The field transports the electrons produced at the cathode surface towards the anode. Note that if the field is strong enough, a large number of electrons will reach the anode. Assuming that the electrons undergo ionizing collisions as they travel across the electrode gap, their number will increase by:

$$\mathrm{d}n = \alpha n \mathrm{d}y \longrightarrow n(y) = n_0 e^{\alpha y}, \tag{2.2.1}$$

where n is the number of electrons travelling a distance of y from the cathode, n_0 is the initial number of electrons generated at the cathode and α is the first Townsend ionization coefficient, which describes the average number of ionizing collisions caused by a single free electron travelling a distance of 1 cm under the influence of the applied electric field. From Equation (2.2.1), the number of electrons that strikes the anode per second is $n_d = n_0 e^{\alpha d}$. If we consider the secondary processes that take place as a result of the primary process of ionizing collision, the number of secondary electrons generated at the cathode is expressed as $\gamma n_0 (e^{\alpha d} - 1)$ [25]. γ is the second Townsend ionization coefficient, which describes the average number of secondary electrons emitted at the cathode surface per ionizing collision in the electrode gap. If for each electron that leaves the cathode at least one secondary electron is generated, the discharge then becomes self-sustained. This can also be interpreted as the onset of the breakdown. The condition for Townsend breakdown to take place in an electrode gap, also known as Paschen breakdown law can be expressed as follows [24, 25]:

$$pd = \frac{p}{\alpha} \ln\left(1 + \frac{1}{\gamma}\right), \tag{2.2.2}$$

where p is the gas pressure.

Stellenbosch University http://scholar.sun.ac.za

2.2.2 Streamer breakdown

At large *pd* values and fast rising high-voltages, the breakdown mechanism that takes place is called a streamer. Streamer breakdown is characterized by a highly conducting filamentary channel (or spark discharge) which bridges the inter-electrode gap in a time much faster (few nanoseconds) than the time it takes the secondary electrons to cross the gap [24]. The streamer development is as a result of the additional electric field created by an individual avalanche. The field causes distortion of the applied field, whereby the secondary electrons produced by photoionization move towards the avalanche head. In the process, the secondary avalanches generated converge towards the primary as illustrated in Figure 2.2(a). Since electrons are lighter than ions, they move very fast towards the avalanche head, leaving behind the positive ions in form of a slowly moving tail. The resultant field in front of the avalanche head is enhanced. However, that just behind the head (i.e. between the electrons and the tail) is weaker. The field between the tail and the cathode is also enhanced. Therefore since the fields at both the cathode and anode are enhanced, the entire electron gap will be covered by the streamer plasma as shown in Figure 2.2(b).

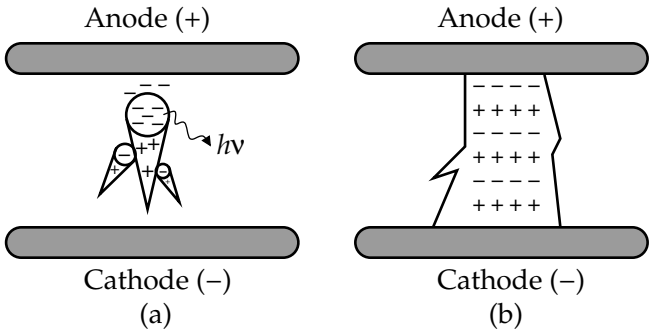

Figure 2.2: *Schematic diagrams illustrating streamer breakdown: (a) initiated by a single primary electron avalanche, and (b) when the entire electrode gap is bridged by the streamer plasma [24].*

The condition for streamer breakdown to take place, usually attributed to Raether is given by the equality of the radial space charge field to the applied electric field and in air (m.k.s.units), it can be expressed as [24]:

$$pd = \frac{p}{\alpha}\left(\ln d + 20\right). \tag{2.2.3}$$

For a typical TEA laser discharge, Equation (2.2.3) is easily satisfied. Therefore, such a discharge would favour streamer (or arc) discharge mode over the desired Townsend (or glow) discharge mode. Streamer breakdown should be avoided because it results in inefficient energy transfer into the laser discharge and damaging of the laser electrodes.

2.2.3 Preionized breakdown

Stable glow discharges at high gas pressure can be generated by introducing a suitable number of seed electrons uniformly distributed over the entire discharge volume prior to the onset

Stellenbosch University http://scholar.sun.ac.za

of the main discharge [24, 26]. The level of preionization electron density required to obtain stable glow discharges is dependent upon electrode profile, electrode surface finish, type of gas and pressure, voltage rise-time, duration of preionization, etc. Preionization of the gas volume generates a large number of avalanche initiating electrons uniformly distributed throughout the gap. The resulting electron avalanches overlap (Figure 2.3), thus limiting their growth to a value lower than the critical value for streamer formation.

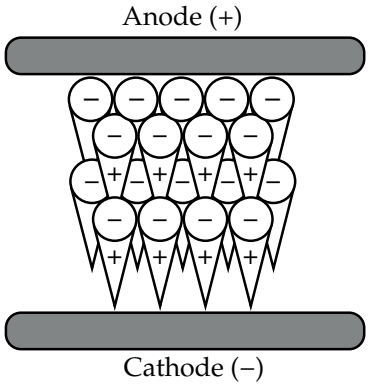

Figure 2.3: *Schematic illustration of preionized breakdown: the avalanche heads and tails overlap, resulting in a homogeneous charge carrier density and thus a homogeneous discharge plasma [26].*

The initial electron density required to generate stable discharges has been estimated to [24]:

$$n_0 \geq \left(\bar{\lambda} x_{\text{crit}}\right)^{-\frac{3}{2}}, \tag{2.2.4}$$

wherein $\bar{\lambda}$ is the electron mean free path and x_{crit} is the critical distance for streamer development. The product $\bar{\lambda} x_{\text{crit}}$ in Equation (2.2.4) scales as p^{-2} and therefore n_0 as a third power of pressure, thus emphasizing the demand for preionization at high gas pressure. The preionozation electron density required to generate uniform arc-free discharges in a typical TEA CO_2 laser is estimated to be in the range 10^5–$10^8\,\text{cm}^{-3}$. However, electron densities of more than $10^{10}\,\text{cm}^{-3}$ have been measured, and proved to be beneficial in producing higher laser output [27]. The increase in initial electron density results in a larger number of overlapping primary avalanches and hence very homogeneous discharge plasma.

2.3 Preionization techniques

Preionization of TE gas discharge lasers can be effected by means of several techniques, for example, ultraviolet (uv) preionization [28, 29], x-ray preionization [30], and electron beam preionization [31]. Both x-ray and electron beam preionization techniques have an advantage of providing large volumetric discharges. In fact, pulse energies of several 100 joules can be achieved with these techniques [32]. However, x-ray and electron beam controlled laser systems considerably increase the system operating costs and technological complexity. In addition, there have not yet been x-ray sources and foil windows capable of demonstrating reliable long

Stellenbosch University http://scholar.sun.ac.za

time operation at high repetition rates. Even then, the high x-ray fluxes required will necessitate strong x-ray shielding. Although it has low penetration depth in high pressure gas discharge mixtures, uv preionization is simple to realise and very convenient. This technique can be broadly classified into two categories depending on the method of generating the uv radiation, for example, by a spark or corona discharge. In this thesis, uv preionization was employed in a mini TEA CO_2 laser. Therefore, it is this technique that will be explored in more details.

2.3.1 The physics of uv preionization

The process of uv preionization takes place as a result of photoionization of the gas components by uv radiation emitted by an auxiliary discharge. The discharge is commonly generated by either spark or corona, which are both efficient emitters of hard uv radiation [33]. For a typical CO_2 laser gas mixture, the ionization potentials of the gas components are listed in Table 2.1.

Gas component	Ionization energy [eV]	Ionization wavelength [nm]
He	24.5	50.6
CO_2	13.8	89.9
N_2	15.6	79.5
CO	14.0	88.6
O_2	12.1	102.5

Table 2.1: *Ionization potentials of the typical CO_2 laser gas components.*

Photoionization of the active CO_2 laser gas mixture is, however, very difficult because of the strong absorption in the vacuum uv by CO_2 [34]. This necessitates that for effective photoionization, the largest portion of the ionizing radiation spectrum should lie within the spectral transmission windows of CO_2, i.e. in the range 117–124 nm and approximately above 160 nm [34]. It has also been shown [33] that helium is transparent to radiation of wavelength greater than 115 nm, while nitrogen also absorbs poorly in this range. Thus, photoionization in the CO_2 laser can not be effected by direct single-photon ionization of one of the primary gas components in the CO_2 laser gas mixture as can be seen from the values in Table 2.1. Therefore, it is believed that photoionization occurs from low ionization potential impurities contained in the gas mixture or easily ionizable organic compounds intentionally added to the mixture. Photoionization of the background impurities in the gas mixture, with ionization potentials of less than 10.5 eV (> 120 nm) takes place according to the following equation [35]:

$$M + h\nu \longrightarrow M^+ + e^-, \quad \text{where } h\nu > 10.5\,eV. \tag{2.3.1}$$

2.3.2 Spark preionization

Spark discharge is the most common method of generating uv radiation, at least for the laboratory and some commercial laser systems [28]. Generally, there are two types of spark

Stellenbosch University http://scholar.sun.ac.za

discharges. The conventional spark discharge generated between two spark electrodes and that generated over the surface of a dielectric material [30]. Figure 2.4 shows the different constructions of spark sources. The spark array construction shown in Figure 2.4(a) is the simplest and most widely employed in TEA CO_2 lasers [17, 21, 36]. It consists of several two electrode pins facing each other. When a fast-rising high-voltage pulse is applied to the pin electrodes, spark discharges are initiated between the pin gaps. These discharges produce uv radiation which is enough to provide good preionization levels in the discharge volume. Another variation of the spark source construction is the surface spark rod shown in Figure 2.4(b). It consists of several series connected spark gaps arranged along the surface of a dielectric material. Upon application of a fast high voltage pulse, the breakdown of the first gap is initiated which causes an increase in voltage across the second gap triggering its rapid breakdown. The process continues until all the gaps are closed resulting in spark discharges along the surface of the dielectric. Dielectric materials used in surface spark rods are mainly alumina ceramics and Pyrex glass because of their high dielectric constants and very good wear properties.

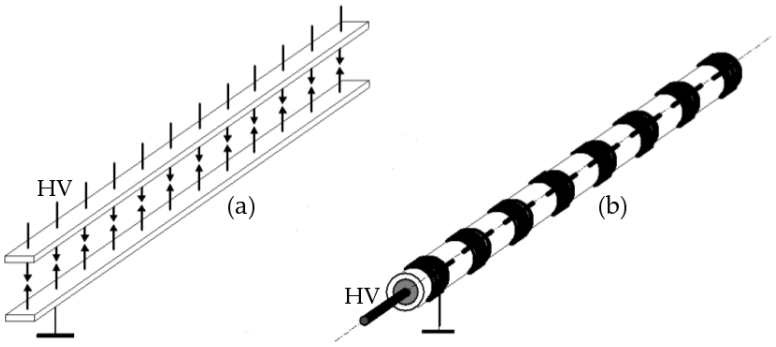

Figure 2.4: *Schematic construction of spark preionization sources: (a) pin-to-pin spark arrays and (b) surface spark rod [37].*

Surface spark rods have advantages of bright illumination of the discharge volume as well as lower breakdown voltage. However, in higher repetition rate applications, conventional spark arrays seem to be the preferred technique. Generally, there is a longstanding concern about the long term performance of spark electrodes. These electrodes suffer from burn-off resulting in erosion which does limit the electrode lifetime. In addition, the sputtered electrode materials contaminate the working gas mixture and the discharge cell. Thus limiting the lifetime of the gas mixture as well. The lifetime of the gas mixture can be sustained by frequent replenishment-evacuation, however, the process can be expensive.

Another problem associated with spark arrays is dissociation of CO_2 molecules into CO and O_2 due to high temperature and high current density that can be reached in the spark discharge. The generated molecular oxygen forms negative ions through dissociative attachment mechanism, which takes place at the cost of an electron in the discharge volume. This affects the laser discharge stability and ultimately reduces the laser output. To stabilize the discharge, gaseous additives and catalysts are often used, however, these make the system more complicated and expensive. In addition, gaseous additives have a tendency of depositing coatings on the inside

Stellenbosch University http://scholar.sun.ac.za

walls of the discharge cell and optics. Once introduced in the system, these coatings cannot easily be removed. All these shortcomings can be relieved by making use of surface corona discharges which will be discussed in Subsection 2.3.3. Unlike in spark arrays, corona preionization is known to cause less dissociation of CO_2 molecules due to lower current density and it also provides significantly reduced gas contamination.

The various schematic configurations of spark preionization are shown in Figure 2.5. In general, spark array sources are arranged close to the main discharge gap either on both sides (Figures 2.5(a) and Figure 2.5(b)) or only one side of the main discharge electrodes as shown in Figure 2.5(c). Double side preionization has the advantage of more uniform illumination as compared to single side preionization where the discharge tends to shift to the preionization side. The spark preionization sources are usually placed centrally in order to achieve optimal illumination of the discharge volume. However, in high repetition rate applications, centrally placed preionization sources tend to provide greater perturbation to the gas flow. This problem can be reduced by moving the preionization source closer to one of the main discharge electrodes, while maintaining its distance from the discharge centre very small.

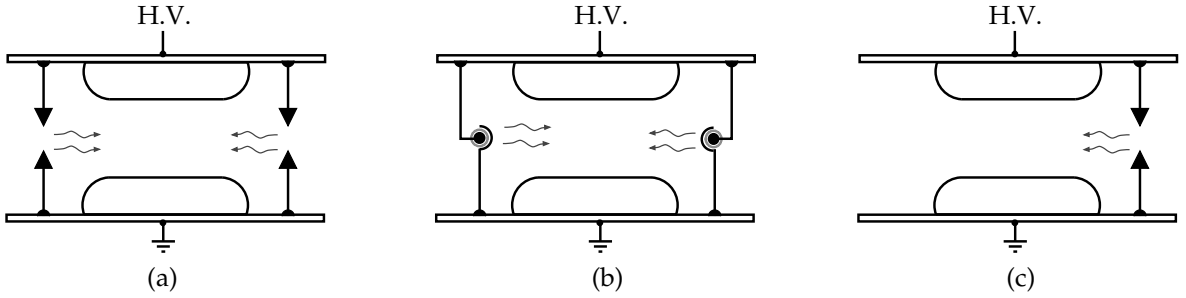

Figure 2.5: *Schematic configurations of spark preionization: (a) double side spark arrays, (b) double side surface spark rods, and (c) single side spark arrays.*

For large systems with large discharge cross-section, this approach is not feasible. This is because the distance from the preionization source to the discharge centre is such that large preionization gradients transverse to the discharge electrode axis are caused and hence uniform discharges can not be generated [37]. In large area, large volume systems, the preionization sources can be placed behind or inside one or both of the main discharge electrodes. The ionizing radiation is then transmitted through a semitransparent electrode surface. The advantage of this configuration is that the preionization sources are placed in the closest proximity to the discharge region without causing any disturbance to the gas flow in the discharge gap. It is, however, not well suited to high repetition rate laser systems, where fragile electrode structures are used because of their high transmission for the ionizing radiation. In addition, it becomes difficult to get sufficient gas exchange behind the screen electrode to avoid absorption of ionizing radiation by the contaminated gas.

Stellenbosch University http://scholar.sun.ac.za

2.3.3 Corona preionization

A corona discharge is a highly non-thermal plasma which occurs in the gas medium in close vicinity to an electrode with a small radius of curvature, such as a fine wire or a pin, at a high potential. The resultant electric field distribution along the electrode surface is usually non-uniform. If this field is sufficiently high, it can cause ionization of the surrounding gas. The use of uv radiation generated by a corona discharge as a preionization source has been proposed by Laflamme [38] and Lamberton and Person [39] in a TEA CO_2 laser. In the latter, the corona prionizer was formed by a fine wire placed parallel to the main electrodes and connected to the anode. Upon application of a high voltage pulse, the field emission from the wire induced a corona discharge between the wire and the cathode. This discharge was sufficient to initiate very uniform and repeatable discharges in the electrode gap. Although very simple and effective, the major disadvantage of this configuration is that the fragile wire can easily be destroyed through arcing. Improved corona preionization sources (corona rods) utilize a thin wire or a fine wire mesh stretched along the surface of a thin-walled dielectric tube as shown in Figures 2.6(a) and 2.6(b). If a high voltage pulse is applied to the corona rod, very dense corona discharges are generated along the surface of the dielectric tube. The uv radiation generated by these discharges is very uniform along the surface of the corona rod. Thus, they are capable of providing very uniform preionization densities in the discharge volume. As spark array sources suffer from electrode wear, corona rods are affected by dielectric breakdown especially at high voltages. Dielectric materials that are usually employed for corona rods are mainly alumina ceramics, Pyrex glass and Sapphire because of their high breakdown strength as well as high dielectric constant.

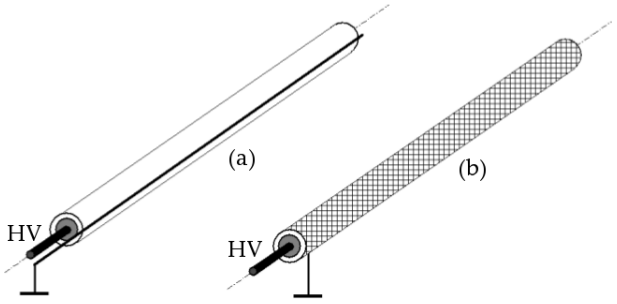

Figure 2.6: *Schematic construction of corona preionization sources: (a) wire electrode rod and (b) wire mesh electrode rod [37].*

The various schematic configurations of corona preionization are shown in Figure 2.7. The corona rods or boards can be arranged as double side preionization (Figures 2.7(a) and 2.7(b)) or single side preionization (Figure 2.7(b)). Surface corona boards are most commonly employed in large discharge volumes. Their major disadvantage, however, is that transverse gas flow into the discharge gap may be difficult due the preionizer geometry, making the design unsuitable in high repetition rate applications. Improved designs have a cut-out in the middle of the preionizer board to allow gas flow.

Stellenbosch University http://scholar.sun.ac.za

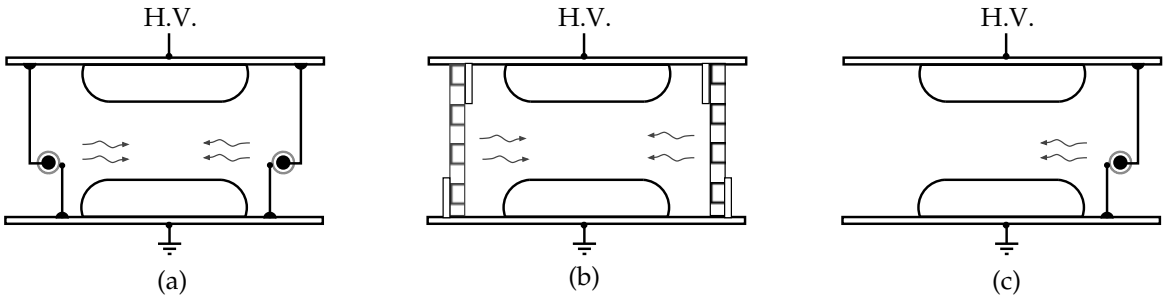

Figure 2.7: *Schematic configurations of corona preionization: (a) double side corona rods, (b) double side corona boards, and (c) single side corona rod.*

Corona preionization is also possible in the behind screen electrode configuration. It is most likely the common arrangement, especially in large area, large volume laser systems.

2.4 Summary

In this chapter, we have discussed the different mechanisms of electric gas breakdown at moderate to high gas pressures. It has been noted that for a typical TEA laser discharge, electric gas breakdown takes place in the form of streamers. This kind of discharge is undesirable and results in inefficient energy transfer into the laser discharge. As a mechanism of suppressing streamer formation, a minimum electron density (10^5–$10^8\,\mathrm{cm}^{-3}$ for a typical TEA CO_2 laser) is usually introduced in the discharge volume prior to the initiation of the main discharge. This process is called preionization and the different techniques have been discussed. The physics of uv preionization has been discussed whereby the wavelength range suitable for preionization corresponds to the two transmission windows of CO_2, i.e. at 120 nm and 175 nm. The radiation is efficiently emitted by both spark and corona discharges. Although it is difficult to directly compare the different preionization techniques, the impression from the discussions in Section 2.3 is that corona preionization is the best technique for the excitation of TEA CO_2 lasers. Corona preionization does produce superior discharge stability as well as excellent pulse-to-pulse reproducibility. In addition, corona preionization seems to offer the least gas contamination and it is likely to cause less dissociation of CO_2 molecules.

Stellenbosch University http://scholar.sun.ac.za

Chapter 3

Pulsed power supply components and circuit topologies

3.1 Introduction

This chapter focuses on the different circuit topologies capable of generating fast rising high-voltage pulses required to pump TE gas discharge lasers. The circuits are designed using different circuit elements and hardware. Some of these elements such as switches and magnetic core materials used for fabricating magnetic switches and pulse transformers are described. Special attention is placed on the analysis of a lossy resonant energy transfer scheme to better understand the dynamics of a magnetic pulse compression (MPC) network. The concept of MPC is explained in more detail. Additional focus is put on the optimization of magnetic core volume with the viewpoint of reducing core losses as well as cutting down capital investment of a given pulsed power supply design.

3.2 High voltage switching devices

Switches are the most important part in a pulsed power supply for exciting a laser. The energy stored in storage devices is transferred between these devices and the laser discharge by a high voltage switch. The switches commonly used in gas discharge lasers are mainly closing switches, which include: electric discharge switches like spark gaps and thyratrons, semiconductor switches like thyristors, metal-oxide-semiconductor field-effect transistors (MOSFETs), insulated gate bipolar transistors (IGBTs), and magnetic switches. The choice of a particular switch used in high voltage switching depends on the following parameters: the voltage hold-off, the peak current of the switched pulse, the pulse rise time, the required repetition rate, the time jitter (shot-to-shot pulse stability) of the switched pulse and the switch operation lifetime [40]. It should be noted that despite the broad diversity of high-voltage switching devices, there is not a single switch yet which is able to simultaneously fulfil all the above parameters. Gas discharge switches like thyratrons and spark gaps which can switch high voltages and high currents have limited lifetime. Semiconductor switches which have a long lifetime and low time jitter, have low voltage and current capacity.

Stellenbosch University http://scholar.sun.ac.za

3.2.1 Spark gap switch

A spark gap switch can be either gas or liquid-filled. The insulating medium (gas for example air or liquid) is typically contained between two main electrodes. The breakdown of the spark gap is generally effected by a high-voltage pulse applied at an auxiliary electrode. The advantages of spark gap switches are: high hold-off voltage (up to MV), high peak current capacity (up to MA) as well as extreme rates of current rise, low-cost and high energy efficiency [40]. The disadvantages of spark gap switches are limited lifetime (typically 10^7 shots or less) and repetition rate (a few tens of pulses per second). In addition, the timing jitter of spark gap switches is high.

3.2.2 Thyratron switch

Like spark gap switches, thyratrons are also gas-filled switches. The working gas can be either hydrogen or deuterium. Deuterium thyratrons are the most common because of their higher operating voltage of more than 30 kV. Hydrogen thyratrons are used in high repetition rate applications ($>$ 3 kHz) because of their faster deionization time. Thyratrons operate at a low gas pressure. Although their rate of rise of current is lower compared to spark gap switches, the repetition rate operation of thyratron switches is comparatively inspiring. They can operate at repetition rates up to thousands of pulses per second, and moreover, their timing jitter can be quite low (down to a few ns). However, they have their own drawbacks. For example they are more expensive and have limited lifetime. In addition, due to the presence of a heated cathode and gas reservoir, thyratron switches are vulnerable to insulating gas degradation.

3.2.3 Semiconductor switches

For a more reliable, longer lifetime, compact and high repetition rate pulsed power supply, semiconductor switches are used as an appropriate substitute for electric discharge switches [20, 22]. In this family (of semiconductor switches), thyristors have comparatively high voltage (several kV) and peak current (kA) capability. However, they are limited by slow switching time, usually of the order of microseconds. On the other hand, MOSFETs have the fastest switching characteristics, but they are limited to low voltage and current ratings (up to 1kV and 100A). IGBTs have advantages of relatively high peak voltage (up to 6.5 kV) and current ratings, and can operate at high switching speed. The typical performance map of semiconductor switches commonly employed in the gas discharge laser systems is shown in Figure 3.1.

In general, all the available semiconductor switches are limited to low peak power capacity and slower switching times which are not suitable for pulsed power applications like excitation of gas discharge lasers. However, there are several circuit configurations and techniques in which semiconductor switches can be used in high voltage switching. For example series and parallel stacking of several semiconductor switch modules, magnetic pulse compression

Stellenbosch University http://scholar.sun.ac.za

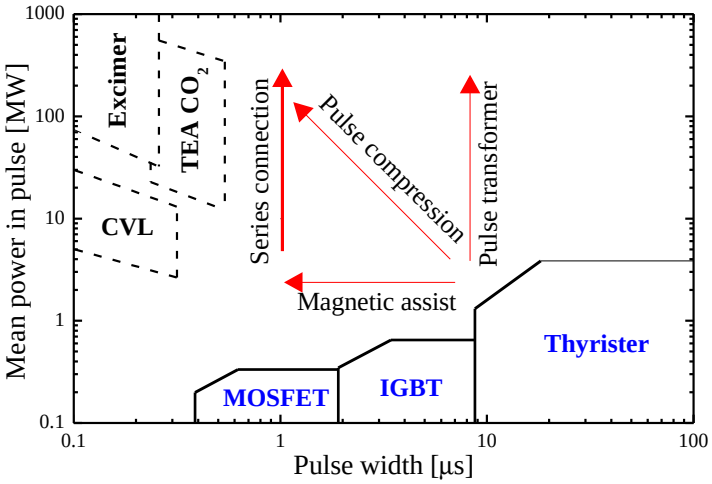

Figure 3.1: *Typical performance map of the semiconductor switches commonly employed in power supplies for exciting gas discharge lasers.*

(MPC) techniques, fast step-up voltage pulse transformers, etc. The magnetic pulse compression networks utilize magnetic switches to compress pulses to the required pulse width. The principle of operation of these switches is explained in the next subsection.

3.2.4 Magnetic switches

Most pulsed power supplies capable of operating at high repetition rate are based on the energy compression capability of magnetic switches. A magnetic switch is a saturable inductor usually constructed as a winding around a ferromagnetic material. It makes use of the nonlinear characteristics of the magnetization BH-curve of ferromagnetic materials to induce a change in inductance. Figure 3.2 shows a typical saturable inductor wound using a toroidal magnetic core.

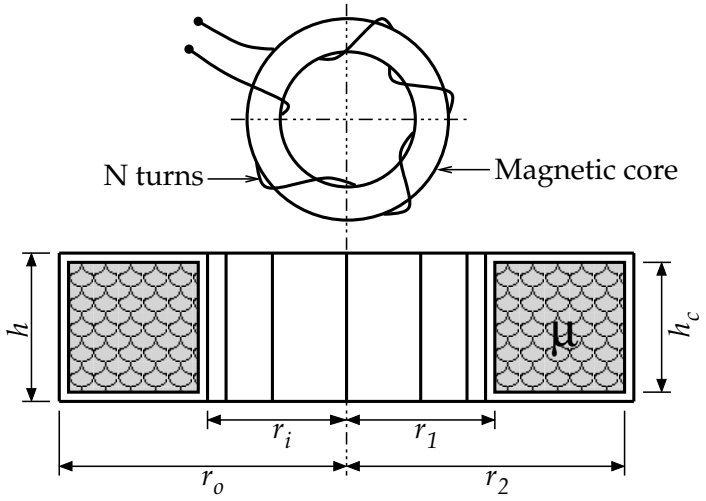

Figure 3.2: *Schematic diagram of a wound saturable inductor.*

Stellenbosch University http://scholar.sun.ac.za

Magnetic switches have two main functions in the circuit: the first one is to compress pulses, and the other is pulse shaping and sharpening. However, they can also be used as a magnetic assist for either a thyratron or semiconductor switch in the circuit. In that case, their function is to delay the conduction of current within the switch until the switch voltage has dropped to a value. This reduces the turn-on losses in the switch. The use of magnetic switches in pulsed power systems was proposed by Melville [41], who demonstrated that long pulses of low peak power can actually be compressed to shorter higher power pulses suitable for radar applications. Magnetic switches are robust and have no problems of electrode deterioration and deionization, thus very long service time (more than 10^{11} shots) even at higher repetition rates can be realised.

3.2.4.1 Characteristics of magnetic switches

The two possible states of the switch, the "ON" state and the "OFF" state correspond to the saturated (low inductance) state and the unsaturated (high inductance) state of the magnetic core, respectively. In the saturated state, the switch presents a conduction path to the flow of current depending on the value of the saturated inductance. During the unsaturated state, the magnetic core has a high relative permeability, thus it presents a very high impedance to the flow of current. The saturated inductance (L_s) and unsaturated inductance (L_u) of a toroidal-shaped magnetic switch with no leakage fields can be respectively expressed as follows:

$$L_\mathrm{s} = \frac{\mu_0 \mu_\mathrm{s} A N_t^2}{l_e} \quad \text{and} \quad L_\mathrm{u} = \frac{\mu_0 \mu_\mathrm{u} A N_t^2}{l_e}, \tag{3.2.1}$$

where μ_0, μ_u and μ_s are the free space, unsaturated and saturated relative permeabilities respectively, A is the cross-sectional area of the magnetic core, N_t is the number of inductor turns around the core and l_e is the effective magnetic field path length, $l_e = 2\pi(r_o - r_i)/[\ln(r_o/r_i)]$, where r_o and r_i are the outer and inner radii of the core respectively. From the Equations in (3.2.1), the ratio of unsaturated to saturated inductances is given by

$$\frac{L_\mathrm{u}}{L_\mathrm{s}} = \frac{\mu_\mathrm{u}}{\mu_\mathrm{s}}. \tag{3.2.2}$$

Typical values of μ_u and μ_s depend on the magnetic material employed in fabricating the core. Generally, the unsaturated relative permeability is of the order of thousands to hundreds of thousands and the saturated relative permeability is close to unity [42]. From Equation (3.2.2), it can be noticed that the performance of a magnetic switch is strongly influenced by the μ_u and μ_s values of the magnetic core.

It is important to know the shape of the magnetization BH-curve (hysteresis loop) which describes the behaviour of ferromagnetic materials. The schematic diagram of such a curve is shown in Figure 3.3. It is produced when the magnetization force H is changed and the corresponding magnetic flux B of the material is measured. A ferromagnetic material initially demagnetized will follow the virgin magnetization (red dashed) curve as H increases.

As the magnetization force increases, the magnetic domains in the material align themselves with the applied field. When almost all the domains are aligned, additional increases in H does

Stellenbosch University http://scholar.sun.ac.za

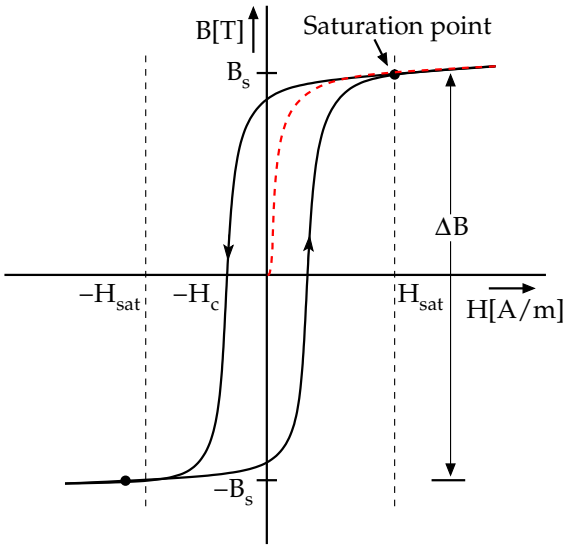

Figure 3.3: *Schematic representation of the magnetization BH-curve of ferromagnetic materials.*

not produce significant changes in B. At this point, the magnetic flux saturates, and this value is denoted by B_s . When the magnetization force is reduced to zero, some magnetic flux remains in the material. In order to demagnetize the material completely, the magnetizing force has to be reversed. The force required to completely demagnetize the material is called coercive force, denoted by H_c . The material will again be driven into saturation in the negative direction by increasing the negative magnetization force. In this case, a maximum magnetic flux swing (ΔB) is obtained, which is given by [42]

$$\Delta B = B_s - (-B_s) = 2B_s. \tag{3.2.3}$$

The parameter ΔB is characteristic to the material and is important for designing magnetic switches.

The switching behaviour of a magnetic switch is illustrated by example of the simple circuit shown in Figure 3.4. It consists of a capacitor, a magnetic switch, stray inductance and a resistive load. The simulated voltage and current waveforms of the circuit are shown in Figure 3.5.

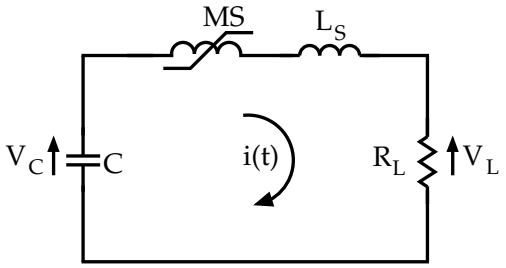

Figure 3.4: *Example of a simple circuit illustrating the switching behaviour of a magnetic switch.*

Initially, a sinusoidal voltage rise is applied across the capacitor. During this time, only a small magnetization current flows through the magnetic switch to the resistive load. This is due to the

Stellenbosch University http://scholar.sun.ac.za

fact that the magnetic switch presents a large impedance (unsaturated) which blocks the flow of current. After the voltage across the capacitor has reached a maximum value, the magnetic switch saturates and changes from large impedance to a small impedance, i.e. at saturation. The magnetization current starts to increase rapidly and the energy stored in the capacitor is dissipated into the resistive load. The saturable inductor therefore acts as a switch.

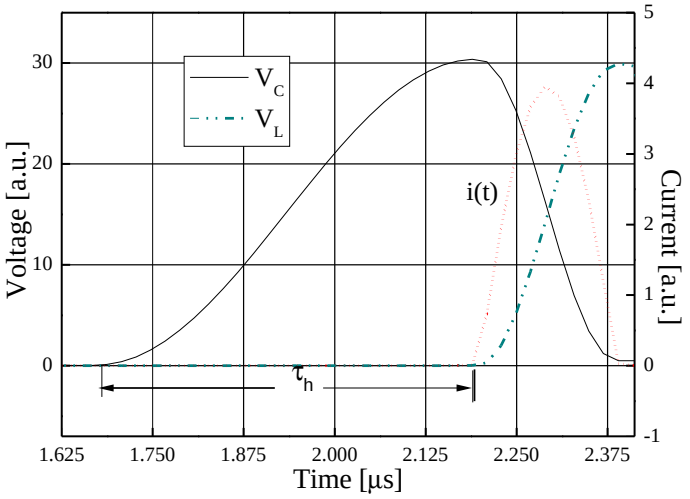

Figure 3.5: *Simulated voltage and current waveforms of the circuit in Figure 3.4: where τ_h is the voltage hold-off time of MS.*

3.2.4.2 Relevant equations in magnetic switching

The current through and the voltage across the winding of a magnetic switch is governed by Maxwell's equations, i.e. induction equation and Ampere's law, respectively, expressed as follows:

$$\oint_C \vec{E} \cdot \vec{\tau} \mathrm{d}s = -\frac{\partial}{\partial t} \iint_A \vec{B} \cdot \vec{n} \, \mathrm{d}A, \tag{3.2.4}$$

$$\oint_C \vec{H} \cdot \vec{\tau} \mathrm{d}s = \iint_A \left(\vec{J} + \varepsilon \frac{\partial \vec{E}}{\partial t} \right) \cdot \vec{n} \, \mathrm{d}A, \tag{3.2.5}$$

where E is the applied electric field, J is the current density, τ is the vector tangent to a contour C, n is the vector normal to the surface area A, and ε is the permittivity of the material. If we neglect any leakage fields, and by applying Equation (3.2.4) to a contour described by a toroidal magnetic core, the voltage-time product of the magnetic switch is expressed as follows:

$$V \cdot \tau_{\mathrm{h}} = \int_0^{\tau_{\mathrm{h}}} V(t) \mathrm{d}t = N_t A_c \Delta B, \tag{3.2.6}$$

where $V(t)$ is the applied voltage, τ_{h} is the voltage hold-off time, defined as the time taken before the magnetic core saturates, A_c is the effective cross-sectional area of the magnetic material. Equation (3.2.6) indicates that the voltage hold-off time is determined by the voltage applied

Stellenbosch University http://scholar.sun.ac.za

across the magnetic switch, the parameters of the magnetic core and the number of inductor turns.

From Equation (3.2.5), we can derive an expression for the current which drives the magnetic core into saturation. This current is called magnetization current I_m of the switch, expressed in the following way:

$$Hl_e = N_t I_m. \tag{3.2.7}$$

In magnetic core parameter studies, Equations (3.2.6) and (3.2.7) are very useful in deriving the BH-curves of the magnetic core materials. The slope of the BH-curve in the unsaturated region gives the total permeability from which the relative permeability μ_r of the magnetic core material can be obtained. The linear relationship between the two magnetic quantities B and H is given by

$$B = \mu H, \quad \text{where } \mu = \mu_0 \mu_r. \tag{3.2.8}$$

Since a magnetic switch is a passive switch which utilises the nonlinear characteristics of the magnetic material, the inductance of the switch is determined by the geometry of the magnetic core shown in Figure 3.2, and is given by [42]

$$L \cong \mu_0 \mu_r \frac{N_t^2 A_c}{2\pi(r_o - r_i)} \ln \frac{r_o}{r_i}. \tag{3.2.9}$$

Equation (3.2.9) is only valid if μ_r is very high because in that case, the leakage field is negligible. If the magnetic core is driven into saturation, and assuming that the relative permeability drops close to unity ($\mu_{r,\text{sat}} \approx 1$), the saturated inductance can be expressed as follows:

$$L_{\text{sat}} \cong \mu_0 \frac{N_t^2 A_c}{2\pi(k-1) r_i} \ln k, \tag{3.2.10}$$

where $k = r_o/r_i$ and $\mu_0 = 4\pi \times 10^{-7}$.

3.2.4.3 Losses in magnetic switches

In designing pulsed power systems using magnetic switches, one must be aware of the losses in these switches. The losses affect the reliability, efficiency and thermal performance of the magnetic switch. Therefore, they must be minimised to achieve high efficiency and for the system to be able to operate at high repetition rates. However, accurate prediction of these losses is amazingly complex because of their dependence on a number of factors. The problem is further complicated by the fact the magnetic core manufacturer's data is also undependable since their measurements and analyses are based on standardized conditions. The losses in magnetic switches are divided into two categories:

- *Copper losses.*
- *Magnetic losses.*

Stellenbosch University http://scholar.sun.ac.za

Copper losses

The copper losses arise from the power dissipated by the resistance of the copper wire winding, as given by the following Equation:

$$P_c = R_w \cdot I_{rms}^2 \,, \tag{3.2.11}$$

wherein I_{rms} is the RMS value of the current through the winding and R_w is the resistance of the winding, which for a circular conductor, can be obtained from

$$R_w = \rho \frac{l}{A} = \frac{4\rho N_t l_T}{\pi d^2} \,, \tag{3.2.12}$$

wherein ρ is the resistivity of the material (e.g for copper $\rho_c(20^\circ) = 1.7 \times 10^{-8}\,\Omega$m), l_T is the average length of one turn and d is the diameter of the bare winding conductor. At higher frequencies, the values of R_w can be very large. The reason is that the effective cross-sectional area of the wire is reduced due to proximity and skin effects. The skin effect is expressed in terms of penetration depth, denoted as δ. It is defined as the depth into a conductor at which the field penetrating the material is reduced by a factor of "e", and is given by [43]

$$\delta = \sqrt{\frac{\rho}{\pi \mu f}} \,, \tag{3.2.13}$$

where μ is the permeability of the medium and f is the operation frequency. It is clear from Equation (3.2.13) that skin effect can be reduced at high frequency by making use of a very thin (small diameter) wire, i.e. litz wire. That said, the geometry of the windings is also important in reducing the proximity effect.

Magnetic losses

Magnetic losses also known as core losses are a combination of three components: eddy current losses, hysteresis losses and residual losses. If a changing magnetic field is applied to the magnetic core, eddy currents are induced in the core. These currents introduce heat in the core, which is often refereed to as eddy current losses, expressed as follows [43]:

$$P_e = \frac{(\pi \hat{B} f t')^2}{6\rho} V_{\text{eff}} \,, \tag{3.2.14}$$

wherein $\hat{B}$ is the peak flux density, t' is the lamination thickness and V_{eff} is the effective magnetic core volume. From Equation (3.2.14), it can be seen that eddy current losses can be minimized by selecting a magnetic core material with high resistivity such as ferrites and/or using very thin lamination material. However, materials with high resistivity are usually associated with low permeability and flux density. Therefore, trade-offs are almost inevitable in selecting suitable materials for designing magnetic switches.

Hysteresis losses on the other hand are determined by the magnetic core material and amplitude of the applied magnetic field. These losses are caused by the frictional resistance encountered by

Stellenbosch University http://scholar.sun.ac.za

the magnetic domains during motion. The energy dissipated in the magnetic core material per unit volume for the magnetization BH-curve (Figure 3.3) is given by

$$U = \int H\mathrm{d}B = \int B\mathrm{d}H. \tag{3.2.15}$$

Since hysteresis losses are dissipated in the magnetic core each time it saturates, these losses are directly proportional to the operation frequency according to the Steinmetz Equation [43]

$$P_h = \chi_h \hat{B}^n f, \tag{3.2.16}$$

where χ_h is a constant determined by the characteristics of the core material and n is the Steinmetz exponent which takes on values from 1.5 to 2.5 and is material dependent. Hysteresis losses can be reduced by choosing the right material. Almost 95% of the total magnetic losses is a combination of eddy current and hysteresis losses. The remainder is normally what is refereed to as residual losses. Although in the literature [43], residual losses are believed to be proportional to f and $\hat{B}$, these losses are very complex and thus not well understood.

3.3 Magnetic core materials

The magnetic core material is a key element in fabricating magnetic switches and pulse transformers. The following are the desirable characteristics of magnetic core materials which can help us in selecting a material for a particular application.

- *Very large ratio of unsaturated to saturated permeabilities.*
- *Large saturation and remanent magnetic flux densities.*
- *Rectangular magnetization BH-curve.*
- *Low magnetic core losses.*

We often expect to find a "perfect" magnetic core material with all the above characteristics. Unfortunately such a "perfect" material has yet to be fabricated. Therefore, tradeoffs of some of these characteristics at the cost of the others is usually unavoidable. There are a large number of magnetic core materials available on the market. The two most investigated categories are the ferrite and metallic materials. Ferrite materials can be easily moulded into odd shapes. They are a class of ceramic compounds with the chemical formula $ABFe_2O_4$, where Fe_2O_4 is iron oxide and AB is a combination of two or more divalent metals, i.e. nickel, zinc, manganese and copper. The two most common ferrites are Nickel–Zinc (NiZn) and Manganese–Zinc (MnZn) [44]. The available magnetic flux density swing of NiZn ferrites is less than 0.8 T and that of MnZn ferrites can exceed 1.2 T. NiZn ferrite magnetic cores exhibit insulation properties (high resistivity) at higher frequency which lead to reduction in magnetic core losses. In addition, they have an advantage of suppressing electromagnetic interference (EMI) and are thus used in

Stellenbosch University http://scholar.sun.ac.za

high frequency applications. MnZn ferrite magnetic cores are highly conductive (low resistivity) leading to leakage due to eddy currents causing high losses at higher frequency operation.

Metallic materials are subdivided into three categories. These include:

- *Amorphous materials e.g Fe or Co based.*
- *Nanocrystalline materials e.g Fe-based nanocrystalline soft magnetic materials, Finemet.*
- *Crystalline materials (permalloy) e.g Fe-Al-Si.*

Fe-based amorphous magnetic cores have high saturation flux density. This makes them ideal candidates for magnetic switches since the required core volume becomes smaller compared to Co-based amorphous materials which have lower saturation flux density. However, Fe-based amorphous magnetic cores have higher losses and magnetostriction compared to Co-based cores [45]. Moreover, their relative permeability is comparatively low. By magnetostriction, we refer to the field induced dimensional changes in ferromagnetic materials. With the continued search for materials with high flux density swing as well as low core losses, nanocrystalline magnetic materials have been developed. These materials have saturation flux density almost as high as Fe-based amorphous materials and core losses as low as Co-based amorphous materials [46]. In addition, they exhibit high relative permeability, which is an important factor in magnetic switching. Crystalline materials are not suitable for pulsed power applications and are therefore not discussed in this thesis.

The commonly employed material because of its very fine grain structure and grain size of 10–15 nm is the Fe-based nanocrystalline material Finemet. Finemet is the trade name for Fe-based nanocrystalline soft magnetic material from the Japanese company Hitachi. Table 3.1 gives a summary of the magnetic and physical properties of magnetic core materials commonly used in designing pulsed power systems. These are Fe-based nanocrystalline alloy, Co-based amorphous alloy, Fe-based amorphous alloy and NiZn ferrite.

Material	**Fe-based nanocrystal**	**Co-based amorphous**	**Fe-based amorphous**	**NiZn ferrite**
Saturation flux density B_s [T]	1.35	0.60	1.56	0.38
Squareness ratio B_r/B_s	0.90	0.80	0.83	0.71
Unsaturated permeability	5000	9000	2500	350
Core loss at 20 kHz [W/kg]	12	5.8	30	40
Curie temperature T_C [°C]	570	365	415	200
Magnetostriction λ_s $(\times 10^{-6})$	+2.3	< 1	+27	-7.8
Electrical resistivity ρ [¯Ωm]	1.1	1.3	1.23	1×10^{12}

Table 3.1: *Comparison of magnetic and physical characteristics of the different magnetic core materials [46, 47].*

Stellenbosch University http://scholar.sun.ac.za

In general, magnetic core materials for fabricating magnetic switches and pulse transformers cannot be chosen by considering only relative permeability or flux density. Other factors such as frequency of operation, required compression ratio, cost optimization, acceptable magnetic core losses, core lamination, construction and size, etc., have to be considered. Nevertheless, some of these factors are sometimes in conflict, thus tradeoffs can be tolerated. In that case, the choice of the material is purely based upon achieving the best performance at the cost of compromising on the other factors.

3.4 Pulse transformers

A sufficiently high peak voltage pulse between 15 kV and 50 kV is needed to excite a TEA CO_2 laser depending on the laser design. As already indicated, such high voltages can be switched directly using electric discharge switches like spark gaps and thyratrons. However, both of them often have lifetime problems. Electric discharge switches can be replaced by semiconductor switches to obtain long-term reliable operation of the laser. Unfortunately the blocking voltage of semiconductor switches like IGBTs and thyristors are only a few kilovolts. Therefore, the gap between the maximum blocking voltage of either IGBTs or Thyristors and the required laser excitation voltage has to be bridged. Sometimes many IGBT modules are stacked together in series to achieve high blocking voltage. However, this can be very expensive and the failure of one module, can lead to overvolting and loss of the remaining switch modules. So mostly, one or two switches are used in combination with a pulse transformer.

3.4.1 Pulse transformer model

Since the real model of pulse transformers is complicated, rather a simplified circuit model is described. The simple equivalent circuit model of a pulse transformer is given in Figure 3.6.

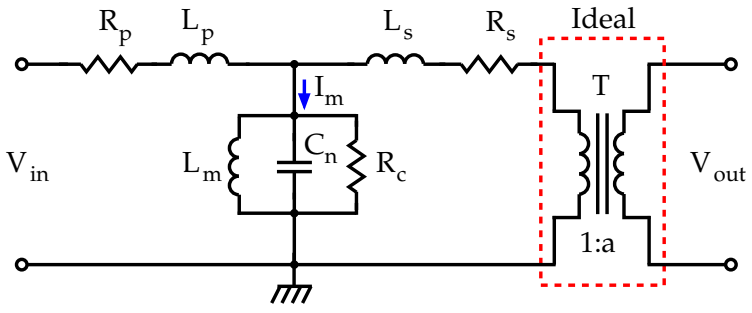

Figure 3.6: *The schematic circuit diagram of the equivalent pulse transformer model.*

In Figure 3.6, R_p and R_s represents the copper wire winding resistances in the primary and secondary windings, respectively. L_p and L_s represents the leakage inductance in the primary and secondary windings which form the total leakage inductance, and C_N represents the total stray capacitance. The transformer losses and magnetizing inductance are represented as R_c

Stellenbosch University http://scholar.sun.ac.za

and L_m. The magnetization current is seen as I_m, which should in principle be smaller than the transfer current. For simplicity, all the parameters are shown as lumped circuit elements. However, they are distributed throughout the region occupied by the windings [48]. In designing a pulse transformer, the effect of transformer parameters has to be well addressed to achieve maximum efficiency. The estimation of each of the transformer parameters is difficult. However, a network analyzer for example in a short circuited pulse transformer can be used to estimate the losses in the windings. The stray capacitance in the windings can be best estimated from the geometry of the transformer.

3.4.2 Leakage inductance

In designing pulse transformers for high repetition rate applications, it is required to keep the leakage inductance of the transformer as low as possible. Leakage inductance affects the voltage output of the transformer due to some energy that can be stored in the leakage flux (i.e. $E_{leak} = L_{leak}(I)^2/2$). However, reducing this inductance is the most difficult part in the design of a pulse transformer. The leakage inductance results from the magnetic flux which does not link the primary and secondary windings of the transformer. In all practical transformers, leakage inductance is inevitable because total flux linkage between the primary and secondary windings would imply spatially overlapping them. In order to minimize the leakage inductance, therefore, the geometry of the primary and secondary windings of the transformer have to be carefully considered. In addition, it is a good practice to estimate the leakage inductance of the transformer before the final design and construction. The total primary equivalent leakage inductance can be estimated using the following Equation [48]:

$$L_{\text{leak}} = \frac{\int_{V_t} \mu_0 H^2 \mathrm{d}V}{I_p^2}, \tag{3.4.1}$$

where I_p is the current through the primary windings and V_t is the total volume of the transformer winding over which the overall volume integration is performed.

3.5 Resonant energy transfer

Almost all pulsing circuits are based on the principle of resonant energy transfer between two or more successive capacitors in a pulsing circuit. The circuit can be either a directly switched C–C transfer circuit or a C–C transfer circuit coupled with a magnetic pulse compression unit. In a directly switched C–C transfer circuit, the circuit has to be able to generate voltage pulses which have sufficiently fast rise-times to efficiently excite the laser discharge. However, under normal circumstances, rise-times of the switched voltage pulse are too low. In that case, a magnetic pulse compression unit is used to temporally compress the voltage pulse. This results in a fast voltage rise-time required for stable and efficient laser excitation. The magnetic pulse compressor can consist of several pulse compression stages. Matching between two successive stages of the

Stellenbosch University http://scholar.sun.ac.za

compressor is very important in the design of a laser pulsed power supply. While optimization of the energy transfer efficiency can significantly reduce capital investment of the power supply design, matching is a pre-requisite for proper functioning of the pulse compression circuit. However, to meet these two requirements in the same circuit design is not straightforward, as it requires some trade-offs. For that, we need to adopt a theoretical understanding of the resonant energy transfer in a loop with resistive losses. The resonant energy transfer circuit consisting of a series connection of an input capacitor C_1, an inductor L, a resistor R which represents the losses in the loop and output capacitor C_2, is shown in Figure 3.7.

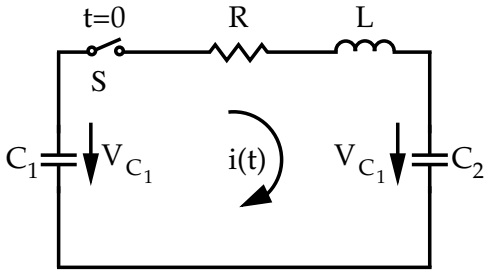

Figure 3.7: *Basic schematic circuit diagram representing a lossy resonant energy transfer scheme.*

It is tempting to think that the circuit in Figure 3.7 is very simple since it consists of only five components. However, its behaviour and energy transfer optimization is not trivial and often misunderstood. The C-C energy transfer loop with losses is of particular importance in the design of multi-stage series pulse compressors, commonly employed in the excitation of gas discharge lasers, where optimal matching of the pulsing circuit is imperative. In fact it has been shown [49] that the treatment of a resonant energy transfer without considering resistive losses in the circuit has lead to mismatch between simulated and experimental results.

By applying the principle of conservation of energy, the loop differential equation of the equivalent lossy resonant energy transfer circuit illustrated in Figure 3.7 is expressed as:

$$L\frac{\mathrm{d}i(t)}{\mathrm{d}t} + i(t)R + \frac{1}{C}\int i(t)\mathrm{d}t = V_0, \tag{3.5.1}$$

where $C = C_1C_2/(C_1 + C_2)$, and V_0 is the initial peak voltage across C_1. Differentiating Equation (3.5.1), we obtain the second-order differential equation

$$LC\frac{\mathrm{d}^2i(t)}{\mathrm{d}^2t} + RC\frac{\mathrm{d}i(t)}{\mathrm{d}t} + i(t) = 0. \tag{3.5.2}$$

Using Laplace transform and applying the initial conditions $i(0) = 0$ and $\frac{\mathrm{d}i(t)}{\mathrm{d}t}|_{t=0} = \frac{V_0}{L}$ to Equation (3.5.2), one can show that the current flowing in the loop can be expressed as:

$$i(t) = \frac{V_0}{\omega L}e^{-\gamma t}\sin\omega t, \tag{3.5.3}$$

where $\gamma = \frac{R}{2L}$, $\omega = \sqrt{\omega_0^2 - \gamma^2}$ and $\omega_0 = \frac{1}{\sqrt{LC}}$. Mathematically, the voltage across C_1 is given as:

$$V_{C_1}(t) = V_0 - \frac{1}{C_1}\int i(t)\mathrm{d}t. \tag{3.5.4}$$

Stellenbosch University http://scholar.sun.ac.za

Substituting Equation (3.5.3) into Equation (3.5.4) and making use of $V_{C_1}(0) = V_0$, Equation (3.5.4) can then be simplified to:

$$V_{C_1}(t) = V_0 - \frac{V_0}{\omega L C_1(\gamma^2+\omega^2)}\left\{\omega - (\gamma \sin\omega t + \omega\cos\omega t)e^{-\gamma t}\right\}. \tag{3.5.5}$$

Since $\gamma\sin\omega t + \omega\cos\omega t$ can be written as $(\gamma^2+\omega^2)^{\frac{1}{2}}\cos(\omega t+\phi)$, where $\phi = \arctan(\frac{\gamma}{\omega})$ and by substituting for ω and ω_0 where necessary, one can express Equation (3.5.5) in the following way:

$$V_{C_1}(t) = V_0\left\{1 - \frac{C_2}{C_1+C_2}\left(1 - \frac{\omega_0}{\omega}e^{-\gamma t}\cos(\omega t+\phi)\right)\right\}. \tag{3.5.6}$$

The voltage across C_2 is mathematically given as:

$$V_{C_2}(t) = \frac{1}{C_2}\int i(t)\mathrm{d}t. \tag{3.5.7}$$

In a similar way, by inserting Equation (3.5.3) into Equation (3.5.7) and again using Laplace transform, one can show that the voltage across C_2 can be expressed as follows:

$$V_{C_2}(t) = V_0\frac{C_1}{C_1+C_2}\left\{1 - \frac{\omega_0}{\omega}e^{-\gamma t}\cos(\omega t+\phi)\right\}, \tag{3.5.8}$$

Equations (3.5.3), (3.5.6) and (3.5.8) are very essential in describing the principle of resonant energy transfer in pulsed power supplies.

3.5.1 Ideal energy transfer

In an ideal energy transfer situation, there are no losses $(R = 0)$. Equations (3.5.3), (3.5.6) and (3.5.8) can then be expressed as:

$$i(t) = \frac{V_0}{\omega_0 L}\sin\omega_0 t, \tag{3.5.9}$$

$$V_{C_1}(t) = V_0\left\{1 - \frac{C_2}{C_1+C_2}(1-\cos\omega_0 t)\right\}, \tag{3.5.10}$$

$$V_{C_2}(t) = V_0\frac{C_1}{C_1+C_2}(1-\cos\omega_0 t). \tag{3.5.11}$$

The energy transfer cycle is complete after a time τ, for which $i(t)$ in Equation (3.5.9) is zero, thus $\tau = \pi/\omega_0$. If we define the ratio of input to output capacitor values as $\alpha = C_1/C_2$, we can express the voltages across C_1 and C_2 after the time τ as follows:

$$V_{C_1}(\tau) = V_0\frac{\alpha-1}{\alpha+1} \quad \text{and} \quad V_{C_2}(\tau) = \frac{2V_0\alpha}{\alpha+1}. \tag{3.5.12}$$

We can also define energy transfer efficiency η as the ratio of the energy transferred to C_2 after time $t = \tau$ to the initial energy stored on C_1 before closure of the switch (t = 0). In case of a lossless transfer, η is given by [50]

$$\eta = \frac{E_2(\tau)}{E_1(0)} = \frac{4C_1C_2}{(C_1+C_2)^2} = \frac{4\alpha}{(\alpha+1)^2}. \tag{3.5.13}$$

Stellenbosch University http://scholar.sun.ac.za

Figure 3.8 shows the calculated energy transfer efficiency η, voltage across C_1 and C_2, expressed as a function of the ratio of the input to output capacitor values α. The energy transfer efficiency reaches 100% under the matched condition $\alpha = 1$, when all the energy initially stored in C_1 is transferred to C_2.

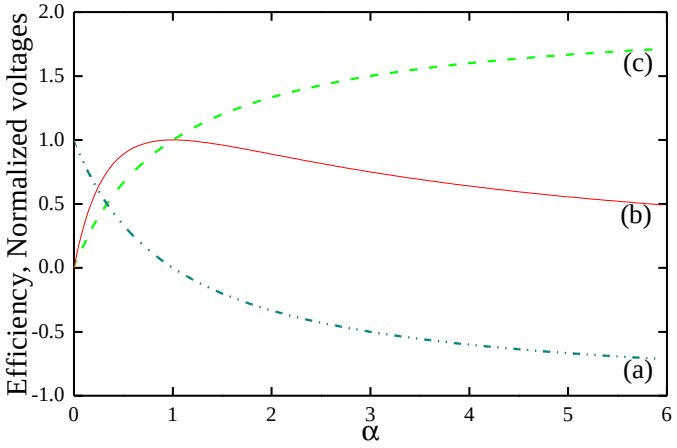

Figure 3.8: *Calculated energy transfer efficiency and voltage ratios across C_1 and C_2 in terms of the ratio of the input to output capacitor values α. (a) V_{C_1}/V_0, (b) Efficiency η and (c) V_{C_2}/V_0. The voltages and energy transfer efficiency are calculated using Equations (3.5.10), (3.5.11) and (3.5.13), with $V_0 = 20\,\text{kV}$ and $L = 2\,\text{nH}$.*

For $\alpha > 1$, there is a voltage residue on C_1 at the end of the transfer cycle as is shown by the curve (a). The voltage on C_2 is increased beyond V_0 (voltage ring-up) as shown by the curve (c): however, at the expense of energy transfer efficiency (transfer efficiency reduces, see the curve (b)). In the limit $\alpha \gg 1$, voltage doubling across C_2 can be achieved, while for $\alpha \ll 1$, voltage undershoot on C_1 at the expense of reduced voltage on C_2 is obtained.

3.5.2 Energy transfer with resistive losses

If we consider resistive losses ($R > 0$), the situation becomes totally different from what we have discussed so far and of course more complicated. Using Equations (3.5.6) and (3.5.8), and considering a weekly damped C-C resonant transfer loop ($\phi \cong 0$ and $\omega \cong \omega_0$), the voltages across C_1 and C_2 at the end of the energy transfer cycle can be expressed as follows:

$$V_{C_1}(\tau) = V_0 \frac{(\alpha - e^{-\gamma\tau})}{\alpha + 1} \quad \text{and} \quad V_{C_2}(\tau) = V_0 \frac{\alpha\,(1 + e^{-\gamma\tau})}{\alpha + 1}. \tag{3.5.14}$$

The maximum energy transfer can be achieved if C_1 is completely discharged at the end of the transfer cycle ($V_{C_1}(\tau) = 0$). From the first Equation in (3.5.14), it is required that $\alpha = e^{-\gamma\tau}$ at the end of the discharge of C_1. Since $\alpha < 1$, it is obvious that C_2 has to be greater than C_1 to achieve complete energy transfer.

Stellenbosch University http://scholar.sun.ac.za

The energy efficiency for the lossy transfer in terms of the capacitor value ratio α and damping coefficient γ at the end of the transfer cycle is given by

$$\eta = \frac{E_2(\tau)}{E_1(0)} = \frac{\frac{1}{2}C_2V_2^2(\tau)}{\frac{1}{2}C_1V_1^2(0)} = \alpha\left(\frac{1+e^{-\gamma\tau}}{\alpha+1}\right)^2. \tag{3.5.15}$$

The exponent term in Equation (3.5.15) is a function of the circuit parameter values R, L, C_1 and C_2. It is expressed as follows:

$$\gamma\tau = \gamma\frac{\pi}{\omega} = \pi\left(\frac{4L(C_1+C_2)}{R^2C_1C_2} - 1\right)^{-1/2}. \tag{3.5.16}$$

When designing pulsed power supplies based on a lossy transfer analysis, the loop inductance L and the resistor R are usually kept constant. This leaves a choice of varying only two parameters C_1 and C_2. However, the choice of which of these two parameters is to be varied, is adopted by considering two design approaches [51].

Design approach I: In this design approach, the input capacitor C_1 is initially charged to a voltage V_0, and it's capacitance value is fixed. The output capacitor C_2 is then chosen so as to maximize the resonant energy transfer efficiency. Equation (3.5.16) can then be expressed in terms of C_1 as:

$$\gamma\tau = \pi\left(\frac{4L(\alpha+1)}{R^2C_1} - 1\right)^{-1/2}, \quad \alpha = \frac{C_1}{C_2}\Big|_{C_1=\text{Constant}}. \tag{3.5.17}$$

Design approach II: In designing pulsed power supplies, specified output parameters like voltage and energy are normally required. Generally, the output voltage V_2 and the energy transferred to C_2 are specified and the capacitance value of C_2 is therefore fixed. The input capacitance C_1 is then varied to achieve these specifications with maximum energy transfer efficiency [49]. Under these design considerations, Equation (3.5.16) can be expressed in terms of C_2 as follows:

$$\gamma\tau = \pi\left(\frac{4L(\alpha+1)}{\alpha R^2C_2} - 1\right)^{-1/2}, \quad \alpha = \frac{C_1}{C_2}\Big|_{C_2=\text{Constant}}. \tag{3.5.18}$$

The transfer efficiencies and voltages across C_2 for the two design approaches are compared for a range of transfer losses. The calculations are based on Equations (3.5.14), (3.5.15), (3.5.17) and (3.5.18). The parameters used in the computation are $V_0 = 20\,\text{kV}$, $L_s = 0.1\,\mu\text{H}$ and output pulse energy of 5 J. In Figure 3.9, it can be seen that with no losses, the optimum capacitor ratio $\alpha = 1$ as it has already been indicated. However, with increasing losses, the optimal value is slightly shifted towards large values of α. In Figure 3.11, we can also notice a slightly higher voltage across C_2 at the end of the transfer cycle corresponding to smaller losses. On the other side, in design approach II, the optimal value shifts to small values of α as the losses increase as depicted in Figure 3.10. The calculated voltages across C_2 using the two design approaches are shown in Figures 3.11 and 3.12 respectively. The behaviour of the voltages is almost similar except that the voltages in design approach I are slightly higher than that in approach II.

Stellenbosch University http://scholar.sun.ac.za

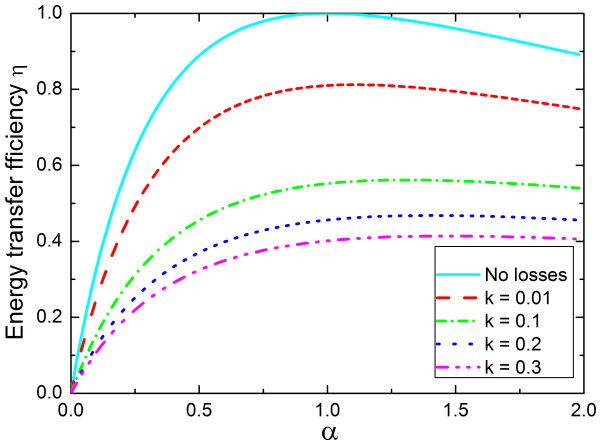

Figure 3.9: *Relative energy transfer efficiency for the design approach I. The efficiency is calculated for different losses in the transfer loop at constant C_1.*

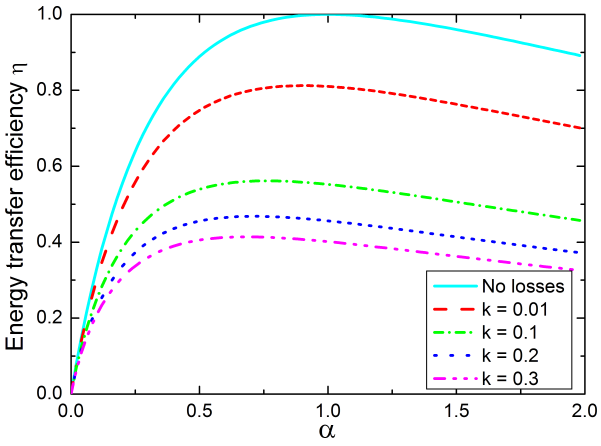

Figure 3.10: *Relative energy transfer efficiency for the design approach II. The efficiency is calculated for different losses in the transfer loop at constant C_2.*

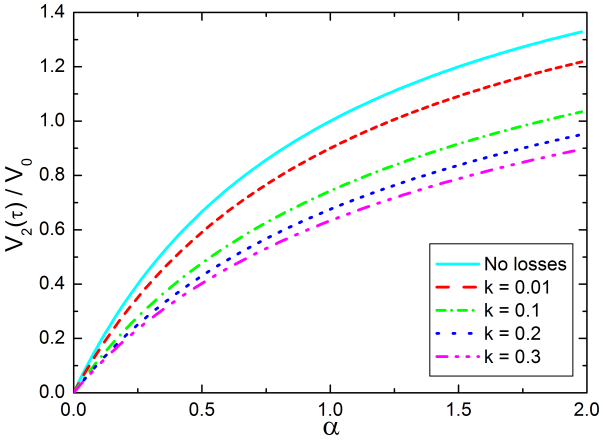

Figure 3.11: *Voltage across C_2 as a function of capacitor ratio for different losses based on design approach I.*

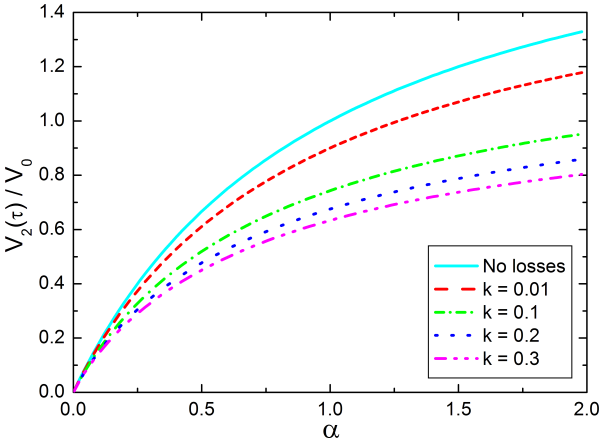

Figure 3.12: *Voltage across C_2 as a function of capacitor ratio for different losses based on design approach II.*

3.6 Pulser circuit topologies

High power pulsed discharge circuits are required to generate short pulses. TEA CO_2 lasers are invariably pumped using pulsers, which transfer the stored energy into the active medium. The pulsed power supply for the laser requires efficient switching of the stored energy into the discharge in a very short time and with a well-defined spatial and temporal profile [35]. This determines the discharge uniformity and stability, both of which influence the quality of the laser output. Such requirements impose constraints on designing a suitable pulsed power supply capable of generating the required peak currents and fast rising voltages. Moreover, the pulsed power supply has to be designed to closely match the dynamic behaviour of the gas discharge whose resistance is time dependent. There are various pulsing circuit topologies commonly employed in the excitation of gas lasers. These include the conventional capacitor–capacitor

Stellenbosch University http://scholar.sun.ac.za

(C–C) transfer circuit, the LC–inversion circuit, magnetic spiker circuits, etc. The operation of all these topologies is based on the concept of resonant energy transfer which has been discussed in the previous section. In this section, the first two topologies are discussed in detail.

3.6.1 C-C Transfer circuit

This is the conventional circuit topology used in the excitation of mini TEA CO_2 lasers. The circuit consists of the storage capacitor C_0 and the peaking capacitor C_p as shown in Figure 3.13. Initially, C_0 is charged to the required voltage and then discharged through the switch S and the inductor L_0. The stored energy is transferred from C_0 to C_p by the resonant energy transfer scheme. When the voltages across C_p and the discharge electrodes reaches the maximum value, the energy is then transferred to the discharge. This occurs when these voltages are close to the breakdown voltage of the gas between the electrodes. The inductor L_d is composed of the stray inductance of the discharge electrode system [35]. For fast high-rising voltage pulses and extreme power deposition into the laser discharge, L_d should be minimized.

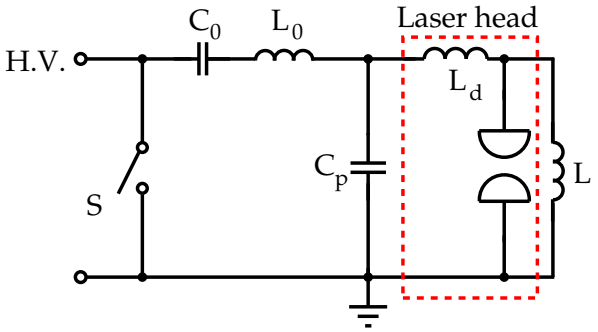

Figure 3.13: *Schematic circuit diagram of the conventional C–C transfer circuit.*

Undeniably, this type of topology is very simple to design and little investment is needed, but it requires a high voltage switching element capable of withstanding the demands of high peak voltage and current mentioned earlier. In fact the traditional high voltage switches employed in this circuit configuration are electric discharge switches like spark gaps and thyratrons. However, as it has been mentioned in Subsections 3.2.1 and 3.2.2, both switches suffer from low reliability, limited lifetime and repetition rate. Although improved thyratron designs and multi-paralleling techniques have been reported, the topology remains expensive and it also requires complex control and synchronization electronic devices. Moreover thyratrons are not readily available. In this case, one has to seek alternative measures to avoid these limitations. As an alternative, magnetic pulse compression (MPC) circuits have inspired especially in reducing the stress on the thyratrons to increase their lifetime [52, 53].

In MPC circuits, energy transfer generally involves a number of stages. The energy is transferred initially at a slow rate from the storage capacitor through an intermediate storage capacitor and then rapidly by a fast switch to the peaking capacitor. Since the initial energy transfer is slow, the stress on the electric discharge switch (e.g. thyratron) is minimized. This is because

Stellenbosch University http://scholar.sun.ac.za

the switch can be allowed to operate at lower rise time and peak current [35]. However, the progress in the development of ferromagnetic materials with very low losses and high relative permeability and semiconductor switches (like thyristors and IGBTs), have supplanted the use of electric discharge switches in many MPC circuits. Semiconductor switches have comparatively longer lifetime, are economical and readily available on the market. Furthermore, these switches do not need warm up time like in the case of thyratrons. Their shortcomings are low voltage ratings (2–5 kV) and longer switching times. In this case, a step-up voltage pulse transformer and pulse compression stages are incorporated in the circuit [21]. A detailed description of the concept of MPC is presented in the later sections.

3.6.2 LC-inversion circuit

This circuit topology resembles a C–C transfer circuit, except that two storage capacitors which are connected in series are used as the initial energy storage bank. Figure 3.14 shows the schematic circuit diagram of an LC-inversion circuit using a two stage MPC. Typically, the addition of one or more MPC stages in the LC-inversion circuit reduces the effect of increased switching currents at low voltages [35].

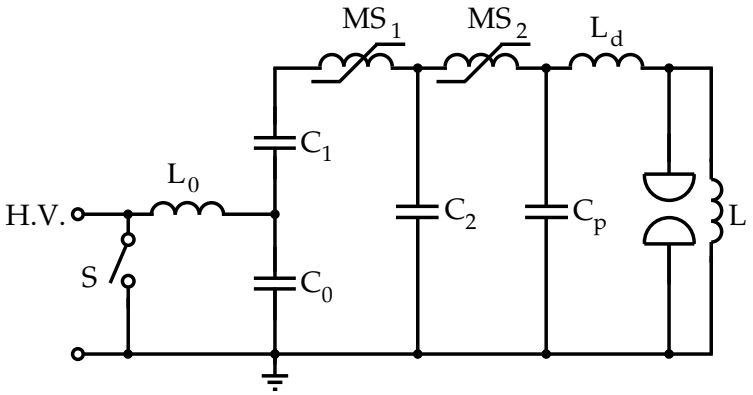

Figure 3.14: *Schematic diagram of an LC-inversion circuit with two stages of MPC [35].*

Capacitors C_0 and C_1 are initially charged to opposite polarities so that there is zero resulting voltage at the first magnetic switch MS_1. When the switch S is closed, the voltage across C_0 is resonantly inverted through the inductor L_0. The inversion leads to a series connection of the two input capacitors and the voltage across the combination is twice the input voltage. Because of this voltage doubling, the LC-inversion circuit topology offers a great advantage of halving the operating voltage for the primary switch [35]. The disadvantage of increased currents at lower operating voltage can be relieved by the addition of two or more MPC stages. In Figure 3.14, the magnetic switch MS_1 is designed to saturate at the point when the inversion is complete. This means that during the inversion, it presents a high impedance to the flow of current. Upon saturation, a normal C–C energy transfer between C_0/C_1 and C_2 is accomplished. The voltage hold-off time during inversion is longer than that during the energy transfer, i.e. $L_{MS_1}(\text{sat}) \ll L_0$. Consequently, this condition leads to pulse compression. All solid-state technology can also be

Stellenbosch University http://scholar.sun.ac.za

used effectively in this topology by adopting any of these two configurations: one is using several semiconductor switches and a pulse transformer [21, 54], the other consists of series and parallel stack of many semiconductor modules only [20, 22]. Stacking several switch modules has an advantage of compactness since the bulky transformer can be avoided. However, simultaneous switching of the stacked modules is sometimes a problem as discussed in Section 3.4.

3.7 Magnetic pulse compression

In the previous sections, the principle of magnetic switches and pulse transformers have been described. In this section, the concept of magnetic pulse compression (MPC) and design optimization strategies are addressed. All MPC circuits are based on C-C resonant energy transfer upon the saturation of magnetic switches as explained before. The most widely used MPC topology, also known as Melville line circuit [41] is the series magnetic pulse compressor. Other MPC topologies are the parallel MPC and the Melville transmission line MPC circuits. The former has an advantage of voltage gain, but the system is much more complicated while the latter is mainly used for output pulse shaping as well as compression of the energy transfer time.

3.7.1 Series MPC topology

The series MPC network consists of multiple C-C resonant energy transfer loops connected in series by magnetic switches, in which at every stage, the output capacitor delivers energy to the input capacitor of the next stage. Figure 3.15 shows the schematic circuit diagram of a series multi-stage MPC network.

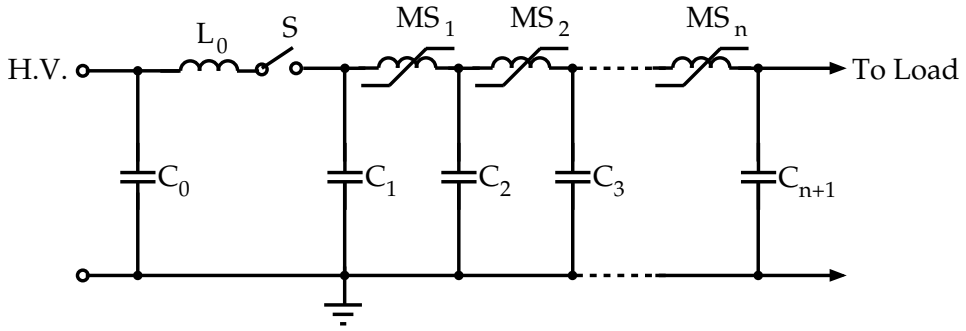

Figure 3.15: *Schematic circuit diagram of a multi stage MPC network.*

In the series MPC circuit shown in Figure 3.15, each magnetic switch is designed to saturate as soon as the preceding capacitor in the loop is fully charged. In that case, the voltage hold-off time of every stage is equal to the energy transfer time of the previous stage. For a lossless energy transfer and equal capacitor values, the voltage across the preceding capacitor will be equal to the initial charging voltage of the first capacitor (i.e. almost 100% energy transfer).

Stellenbosch University http://scholar.sun.ac.za

The condition of pulse compression is attained by effectively reducing the energy transfer time of each successive stage. This can be achieved by decreasing the saturated inductance of the preceding magnetic switch, which from Equation (3.2.10) can can be achieved by either reducing the number of turns or the magnetic cross-section of the inductor.

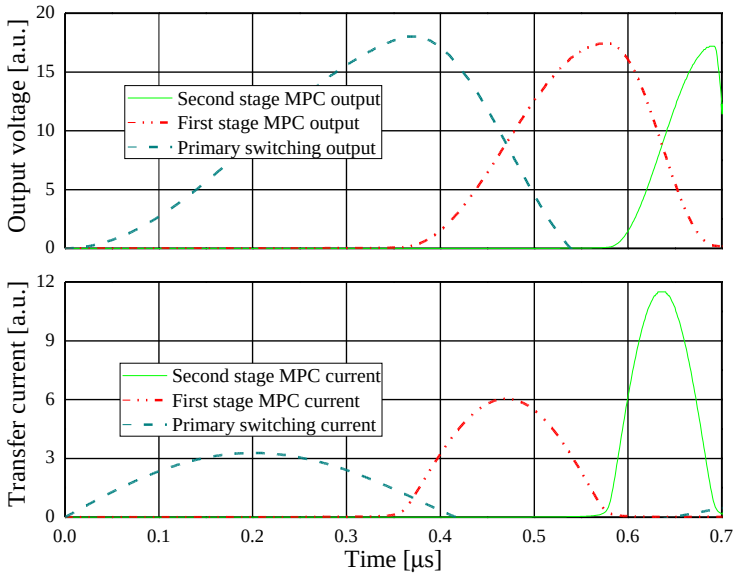

Figure 3.16: *Example of simulated voltage (top) and current (bottom) waveforms obtained in a two-stage series MPC circuit using micro-cap software.*

An example of the typical simulated voltage and current waveforms for a two stage series MPC circuit is given in Figure 3.16. The effect of pulse compression can be clearly noticed, where the low current, long duration pulse (primary switching current) is compressed to high current short duration pulse (second stage MPC current). The increase in peak current which corresponds to the decrease in current pulse duration can be quantified by the principle of conservation of charge in the MPC network. In series MPC networks, current gain is achieved, but at the expense of constant voltage. This necessitates a primary switch which can operate at high voltage but at reduced switching current requirements. In order to get voltage gain, a step-up pulse transformer is usually included in the circuit which enables the use of semiconductor switches at lower voltages for a reliable and high repetition rate pulsing circuit.

Let us now consider a single MPC stage shown in Figure 3.17. The C–C transfer loop in the figure is in principle identical to the C–C transfer loop described in Section 3.5, only that here the loop involves a magnetic switch instead of an active switch. In Figure 3.17, the magnetic switches are designed as explained before. The magnetic switch in the active loop is saturated with a small inductance. Under normal circumstances, the capacitors in the loop are of equal value so that nearly 100% energy transfer is realised. It can be shown that the voltage rise time of capacitor C_n after MS_{n-1} has saturated and the discharge time of C_n after MS_n has saturated are respectively given by [50]

$$\tau_n = \pi(L_{MS_{n-1}}C/2)^{1/2} \quad \text{and} \quad \tau_{n+1} = \pi(L_{MS_n}C/2)^{1/2}, \tag{3.7.1}$$

Stellenbosch University http://scholar.sun.ac.za

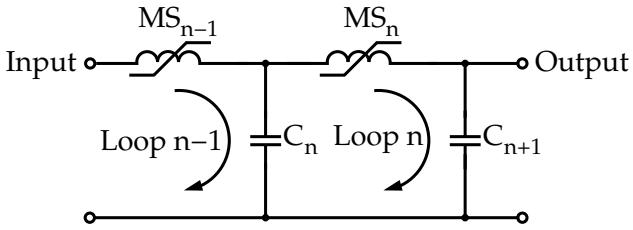

Figure 3.17: *Circuit diagram illustrating synchronization of transfer loops in a single MPC stage.*

where $L_{MS_{n-1}}$ and L_{MS_n} are defined by the second Equation in (3.2.1).

The gain of the nth MPC stage, simply defined as the ratio of the saturation time of stage n to discharge time of stage n, is given by

$$g_n = \frac{\tau_n}{\tau_{n+1}} = \left(\frac{L_{MS_{n-1}}}{L_{MS_n}}\right)^{1/2}. \tag{3.7.2}$$

3.7.2 Magnetic core volume optimization

Optimization of the total core volume is an essential tool in designing a cost effective, reliable and high repetition rate system using MPC circuits. It is well understood that an increase in the core volume does not only lead to increased capital investment but also increases the magnetic core losses. Therefore, one has to seek methods to minimize the magnetic core volume. Generally, there are two design parameters in the MPC unit which can be specified: these are the transfer energy E_0 and the stage gain g. The following assumptions are considered in the core volume optimization strategy: (1) we consider an ideal system with no losses, (2) we assume that the overall parasitic inductance is small and that its effect is negligible, (3) all the capacitor values in the MPC unit are chosen to be equal, and (4) the magnetic cores in the stages are identical, possessing the same magnetic and geometrical properties. Now using Equations (3.2.1), (3.2.6) and (3.7.1), it can be deduced that the volume of the nth magnetic core is expressed as follows:

$$\mathrm{Vol}_n = Al = \pi^2 \frac{\mu_0 \mu_{sat}}{(2p\Delta B)^2} g_n^2 E_0 \,. \tag{3.7.3}$$

Equation (3.7.3) is just an estimation of the core volume in a single stage since it is based on an approximation given in Equation (3.2.1). A more realistic expression for the magnetic core volume is determined by considering the core geometry, i.e. toroidal, U-shaped, strip-line, etc. Such an expression for toroidal magnetic cores has been derived by I. Druckmann, et al. [55], and is given by

$$\mathrm{Vol}_{n,\mathrm{toroid}} = \pi^2 \frac{\mu_0 \mu_{sat} E_0}{(2p\Delta B)^2} g_n^2 \frac{r_o + r_i}{2(r_o - r_i)} \ln\left(\frac{r_o + \Delta r}{r_i - \Delta r}\right), \tag{3.7.4}$$

where Δr is the winding clearance between the inductor windings and the toroidal core surface, and the other symbols carry the usual meaning as defined elsewhere in this thesis.

Analysing Equation (3.7.4), we notice that the magnetic core volume is proportional to the transfer energy. This means that the magnetic core volume can be scaled up with constant

Stellenbosch University http://scholar.sun.ac.za

energy transfer efficiency. Other MPC parameters which can also affect the magnetic core volume include: magnetic flux swing, saturated relative permeability and gain per stage of the MPC network. It should be remembered that magnetic core materials with high magnetic flux density have high losses as well. Therefore trade-offs have to be accepted. Nevertheless, since materials with reasonably high magnetic flux density such as Finemet are readily available, it turns out that gain per stage is the parameter which has the largest impact on the magnetic core volume. A strategy has to be developed to scale the gain per individual MPC stage.

The compression ratio (overall gain) is given by the product of the individual gains for each stage in the MPC network. For an N stage series MPC network, the compression ratio can be expressed as follows:

$$C_r = g_1 \cdot g_2 \cdot g_3 \cdots g_{\mathrm{N}} = \prod_{\mathrm{k}=1}^{\mathrm{N}} g_{\mathrm{k}}\,. \tag{3.7.5}$$

If the gain in each stage is constant, then the gain per stage is given by $g = C_r^{1/\mathrm{N}}$. The number of stages required to achieve a given compression ratio is then given by $N_{\mathrm{stages}} = \log_{\mathrm{gain}} C_r$. It can be shown theoretically [55] that the total magnetic core volume can be minimized when the optimized number of stages is given by

$$N_{\mathrm{opt}} = 2 \ln C_r, \quad \text{with } g_{\mathrm{opt}} = \sqrt{2} \approx 1.65, \tag{3.7.6}$$

where g_{opt} is the optimum gain per MPC stage required to obtain the minimum total magnetic core volume. The value of N_{opt} is obviously not an integer, thus the calculated value is approximated to the nearest integer. It is quite clear that the value of g_{opt} is relatively small and would result in a large number of MPC stages. For example if the design overall compression ratio $C_r = 36$, then it would require $N = 7$ MPC stages. A greater number of capacitor banks for the C-C energy transfer loops will be needed in such a compressor. This can be very expensive and also increases the complexity and physical dimensions of the MPC system. In addition, the overall losses in the system also increases resulting in low efficiency. On the other hand, if a small number of stages say $N = 4$ is chosen for the same compression ratio, the result is a 23% increase in the magnetic core volume. However, this increase is offset by the reduction in the number of capacitor banks, thus requiring low capital investment. Furthermore, the overall losses and complexity of the MPC circuit are reduced. In general, the number of stages in a magnetic pulse compressor is mainly an issue of reliability and cost optimization. In Figure 3.18, a graph of total core volume as a function of number of MPC stages for various compression ratios is given. As expected, the total core volume decreases as the number of stages increase.

It should be emphasised that in our optimization strategy, only magnetic core volume has been considered. However, it can also be interesting to consider the volume occupied by the energy storage capacitor banks and other hardware in the MPC circuit. Optimum gain per MPC stage by considering both magnetic core volume and storage capacitor volume has been studied elsewhere in [56]. Also to mention is that inserting a step-up voltage transformer at any stage of the magnetic pulse compressor does not affect the optimized number of MPC stages, nor does it

Stellenbosch University http://scholar.sun.ac.za

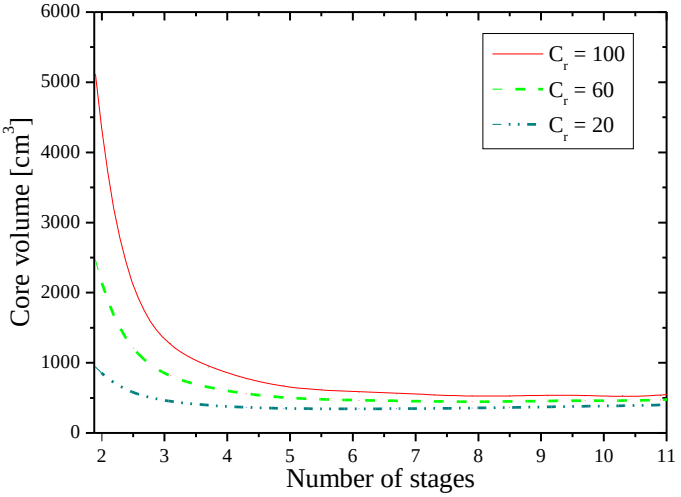

Figure 3.18: *Example of calculated total core volume versus the number of MPC stages for various compression ratios: dimensions of the magnetic core, Finemet (140–mm outer diameter, 89–mm inner diameter, and 10–mm height)*

change the size of the magnetic switches. The choice of the position of the pulse transformer in an MPC unit is a technical one, in which case trade-offs are necessary. For example, in an economical design, the pulse transfer is preferred to be introduced in the last stage of the MPC unit since the required transformer magnetic core volume is reduced due to shorter hold-off times. At the same time, designing a pulse transformer for very short pulses is a difficult task considering the capacitive coupling and leakage inductance.

3.8 Summary

In this chapter, we have evaluated and compared the common pulse circuit topologies capable of generating fast high-rising voltage pulses. Such voltage pulses are required to obtain stable operation of transversely excited gas discharge lasers. The choice of the pulser circuit topology mainly depends on the operation parameters of the main switch and the laser itself. In the conventional pulsers, spark gap and thyratron switches have been utilized. However, both have limited lifetime problems. Of recent, they are increasingly being replaced by semiconductor switches. Nevertheless, semiconductor switches also have power capacity limitations. Several techniques which can be used to relieve this drawback such as use of pulse transformers and MPC networks have been discussed. The principle of operation of magnetic switches and losses in these switches have been presented. A theoretical understanding of energy transfer in MPC networks has been presented using a lossy resonant energy transfer scheme. In order to design an efficient, reliable and cost effective pulsed power supply, a design optimization strategy has been formulated. Some of the ideas discussed in this chapter will be implemented in the next two chapters.

Stellenbosch University http://scholar.sun.ac.za

Chapter 4

Magnetic core parameter measurements

4.1 Introduction

Magnetic switches are the most important components in a pulsed power supply based on a magnetic pulse compression network. They are superior to gas discharge switches like spark gaps and thyratrons because of their high repetition rate capability, long lifetime and high stability switching characteristics. The characteristics of magnetic switches are dependent on the magnetic core material used. The desirable magnetic core materials must have the following characteristics: high effective magnetic flux density change (ΔB), high relative permeability, low magnetic core losses, good long-term stability and reliability, etc. For one to design an efficient pulsed power supply using magnetic switches, it is important to understand the behaviour of the magnetic core materials in advance. Although magnetic core manufacturers often provide datasheets for these materials, such data is usually unreliable. This is because of the fact that the data is based on standardised conditions (i.e. sine-wave voltage excitation) which are different from those mostly imposed to the material in pulsed power applications.

There have been intensive investigations of different magnetic core materials suitable for pulsed power applications in the recent years [46, 57, 58, 59]. In these studies, different forms of magnetic core excitation have been utilized, i.e. constant rate of magnetization (constant voltage), non-linear rate of magnetization, etc. Theoretical models, i.e. bar-domain and saturation-wave magnetization models have also been used to predict magnetic core losses [45]. However, with new magnetic materials being developed, it is very important to measure their magnetic properties. This provides us with a platform for comparing the performance of the new developed materials with the conventional ones with the viewpoint of selecting the best material. In this present chapter, we describe an experimental setup and procedures for measuring the magnetic properties of different magnetic core materials. The non-linear BH-curves, relative permeability, energy loss density, and other important parameters are calculated by numerical processing of the measured voltage and current waveforms.

4.2 Experimental test setup

The schematic of the magnetic core test setup is given in Figure 4.1. It consists of the following: a high voltage power supply, an electrical excitation circuit, the magnetic core under investigation and an oscilloscope for storing the measured voltage and current waveforms.

Stellenbosch University http://scholar.sun.ac.za

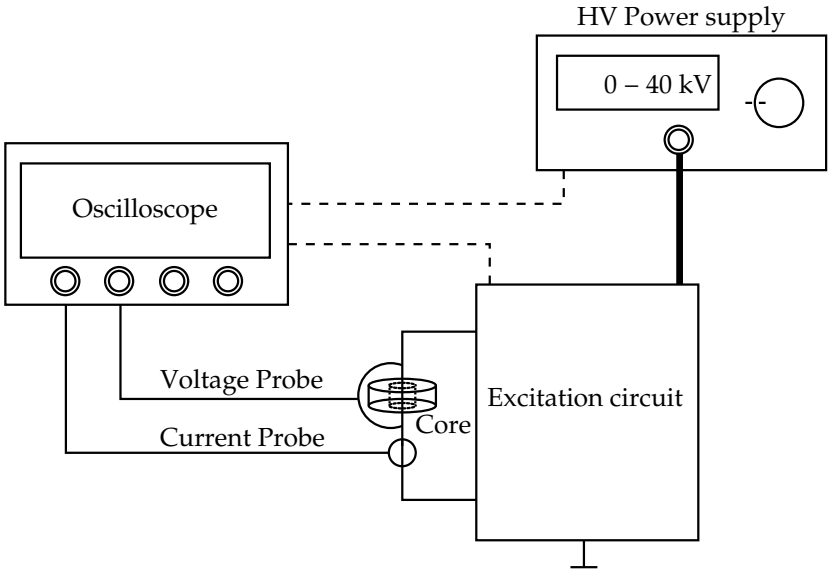

Figure 4.1: *Schematic overview of the magnetic core test setup*

4.2.1 High voltage excitation circuit

The schematic circuit diagram depicting the electrical excitation circuit of Figure 4.1 is shown in Figure 4.2. In order to demagnetize the core sample to the initial starting point (i.e. $H = 0\,\mathrm{A/m}$, $B = 0\,\mathrm{T}$) prior to each excitation process, a reset circuit capable of producing a DC current between 2.5 A and 5 A was used.

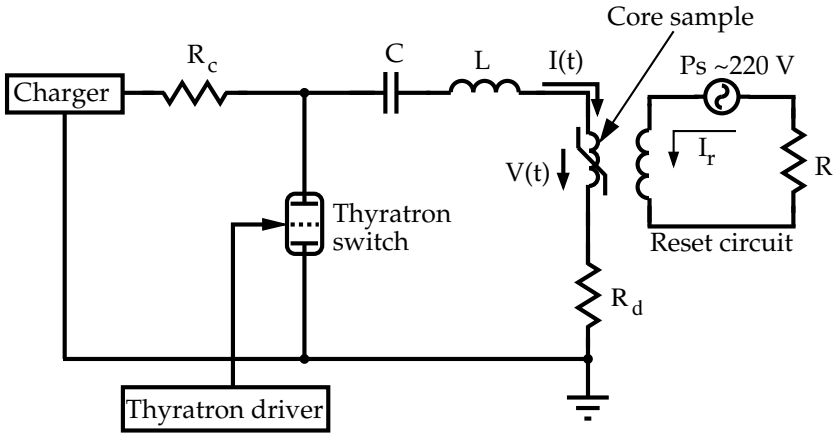

Figure 4.2: *Schematic circuit diagram of a simple low inductance electrical excitation circuit for measuring the magnetic core parameters: where* $R_c = 1.5\,k\Omega$, $C = 10\,\mathrm{nF}$, $L = 65\,\mathrm{nH}$ *and* $R_d = 5.5\,\Omega$.

In Figure 4.2 Ps is an adjustable stabilized laboratory reset power supply and R ($1\,\Omega/10\,\mathrm{W}$) is a current limiting resistor. The capacitor bank C was charged by a 40 kV power supply (Lambda EMI, Model 402L) through a high voltage charging resistor R_c. During the time of charging the thyratron switch (F–189, 35 kV max) is open. The charging current flows through the winding of the core sample, but since it is in the same direction as the reset current, the core remains in the reverse saturated state. After the capacitor is fully charged the thyratron is triggered by

Stellenbosch University http://scholar.sun.ac.za

an external pulse generator and at this time the energy stored in the capacitor is discharged through the winding of the core sample. This results in a constant voltage signal which rapidly develops across the magnetic sample. A low inductive 5.5 Ω dumping resistor was connected in series with the magnetic core winding to limit the current through the core sample after it has saturated. The whole set-up was enclosed by a Faraday shielding cage to reduce electromagnetic interference (EMI). To avoid overheating of the thyratron switch and the core sample, cooling fans were installed at the sides of the excitation circuit. The voltages across the magnetic core sample and the dumping resistor were monitored using a high-voltage probe (model: Tektronix P6015A). The magnetizing current flowing through the magnetic core winding was monitored using a fast Pearson pulse current transformer (model: 1025, 0.025 V/A sensitivity). The voltage and current waveforms were recorded using an oscilloscope (model: Tektronix TDS1012) and were then transferred to a personal computer for further calculations and analyses.

4.3 Magnetic core materials

Three magnetic core materials were evaluated: Fe-based nanocrystaline soft magnetic alloy (Finemet, FT–1H Hitachi), ferrite and amorphous alloy (VAC 6030Z, Vacuumschmelze). Both FT–1H and the VAC 6030Z cores were toroids made of metal ribbon tapes co-wound with Mylar insulating material, whereas the ferrite core is a solid oxide toroid. The dimensions of the magnetic cores and their static magnetic properties are given in Table 4.1.

Parameter	**FT–1H**	**VAC 6030Z**	**Ferrite**
Flux density change, ΔB [T]	2.53	1.6	0.6
Effective cross-sectional area [m^2]	2.09×10^{-4}	8.52×10^{-4}	7.92×10^{-4}
Average magnetic path length [m]	0.346	0.399	0.405
Packing factor	0.76	0.63	1
Tape thickness [μm]	18	25	NA

Table 4.1: *Summary of the dimensions and the static magnetic properties of the tested materials.*

For each material evaluated, the magnetic cores were wound with well distributed toroidal windings chosen to match the desired saturation time. For example in the evaluation of ferrite material two cores separated by a 45 μm-thick Mylar film were used with a 12-turn double winding of copper wire. Photographs of the double winding configuration are shown in Figure 4.3.

In general, the advantage of multiple winding configurations is that uniform magnetization of the entire magnetic core can be realised with small turn numbers. This reduces any effects due to non-uniform magnetization. Additionally, the high voltage and ground connections in this kind of configuration are well separated.

Stellenbosch University http://scholar.sun.ac.za

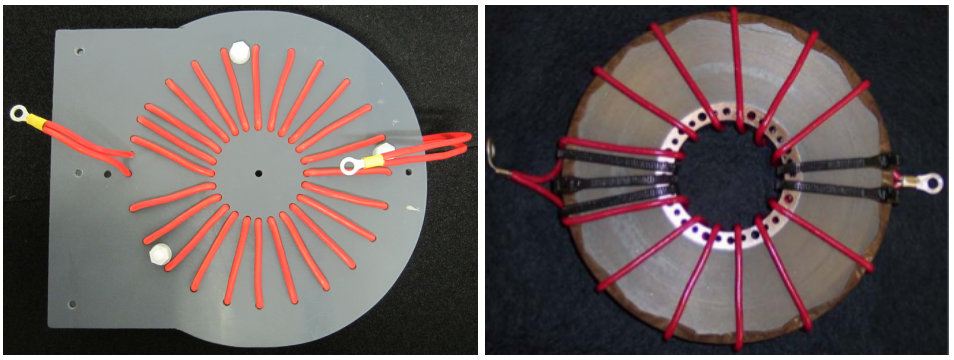

Figure 4.3: *Example of 12-turn double-wound (left) and (right) 6-turn double-wound magnetic core samples.*

4.4 Theory of the measurement and data processing

A python computer program was written to derive the initial B–H curves, determine the saturation time, core loss density, loss factor, and relative permeability of the magnetic cores. The input parameters were the dimensions of the magnetic core and the measured voltage and current waveforms. The B–H curves were generated using Equations (3.2.6) and (3.2.7), which for numerical integration can be re-written as follows:

$$\Delta B = \frac{1}{N_t A_e} \sum V_c(t) \Delta_t, \tag{4.4.1}$$

$$H = N_t \ln(r_0/r_i) I(t) / 2\pi(r_0 - r_i), \tag{4.4.2}$$

where Δ_t is the sampling time interval of the data points and A_e is the effective cross-sectional area of the material. Since the wound magnetic cores were connected in series with the dumping resistor R_d, the measured voltage across the winding of the magnetic core sample with respect to ground, i.e. $V(t)$, is the sum of the voltage across R_d, i.e. $V_{R_d}(t)$, and the voltage across the magnetic core, i.e. $V_c(t)$. Therefore, the voltage across the magnetic core alone was obtained as follows: $V_c(t) = V(t) - V_{R_d}(t)$. The half-cycle magnetic core losses U and the core loss density u were evaluated numerically using the following equations:

$$U(\mathrm{J}) = \sum_0^{\tau_s} V_c(t) I(t) \Delta_t \quad \text{and} \tag{4.4.3}$$

$$u(\mathrm{J/m^3}) = U(\mathrm{J}) / V_{\mathrm{eff}}, \tag{4.4.4}$$

where τ_s is the saturation time and V_{eff} is the effective magnetic core volume of the material. Because of the variations in the effective magnetic flux density, the required magnetic core volume for a given design varies greatly between materials (see Equation (3.7.3)). Therefore, knowing only the core loss densities of these materials is not enough to compare between them. In the past studies, a figure of merit, known as loss factor [60], has been used to effectively compare different materials, and the same figure of merit has been adopted in our study. By definition, the loss factor denoted as L_f, is the ratio of core loss density to the square of saturation flux density swing, given as

$$L_f = u(\mathrm{J/m^3}) / \Delta B^2. \tag{4.4.5}$$

Stellenbosch University http://scholar.sun.ac.za

It should be noted that Equation (4.4.5) does not include any non-material dependent parameter, therefore, it is suitable for core-to-core comparison. Precise determination of the saturation time in Equation (4.4.3) is important in order to calculate the magnetic core losses. However, because of current pulse distortion before saturation (see Figures 4.4 and 4.5(a)), it is always difficult to accurately determine the boundaries of the saturation time. In literature, different ways of determining this time have been suggested. For example, McDonald et al. [58] employed a B-dot probe placed close to the core under test to indicate the end of saturation time. The B-dot probe generates a signal which is proportional to the first derivative of the current through the magnetic core winding. In this way, one is able to detect any changes in the slope of the current signal which marks the end of saturation time. However, with this method, the probe has to be highly calibrated. Extreme care must also be taken not to over-volt the probe which would otherwise lead to oscillation of the excess voltage through the oscilloscope. Nakajima et al. [46] assumed a rectangular voltage pulse and used the full width at half maximum (FWHM) of the voltage pulse as the saturation time. However, as it can be seen in Figure 4.4, the voltage pulses are not really rectangular. In this study, a simple method of determining the boundary of the saturation time has been adopted, and is used throughout all our calculations. The saturation time has been defined as the time from voltage application ($t = 0$) to the extrapolated start of the saturation current, i.e. the point of intersection of the slope of the current pulse with the zero line (see Figure 4.5(a)). The overall errors in our measurements and numerical calculations are estimated to be around 5%.

4.5 Results and discussion

Figure 4.4 shows the voltage and current waveforms that were measured for Finemet material, with increasing number of magnetic cores. The applied excitation voltage was 8.5 kV and the reset current was set at 2.5 A. When the thyratron is triggered, the voltage across the magnetic core winding rises rapidly with rise time (10%–90%) in the range of approximately 25 to 28 ns. Due to the high inductance the core(s) present at the time of non-saturation, only a small amount of current (leakage current) flows through the magnetic core winding. This can be seen in Figure 4.4 as small oscillations in the current waveforms. At the time of core saturation the magnetization current rises and the voltage decreases rapidly. The calculated saturation times according to our definition of saturation time corresponding to 1 core, 2 cores and 3 cores were 249, 533 and 812 ns, respectively.

Stellenbosch University http://scholar.sun.ac.za

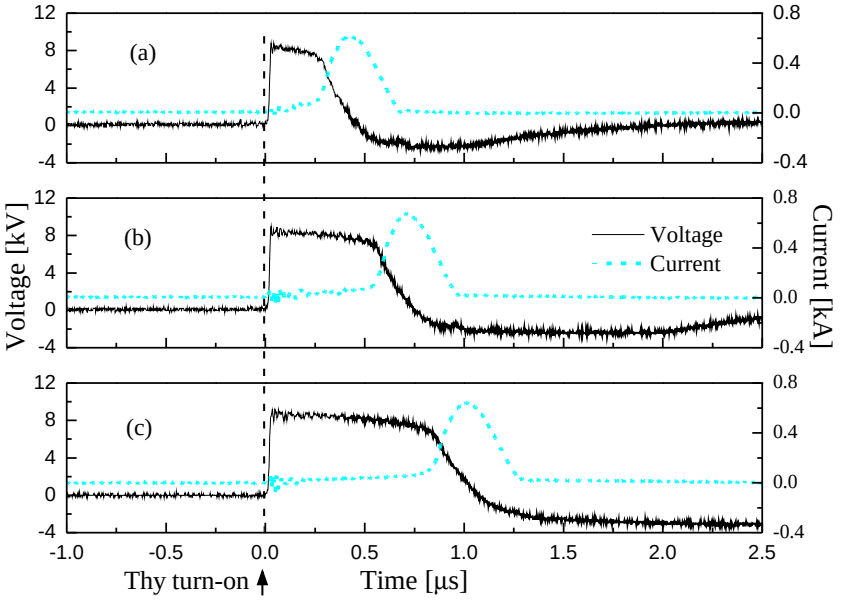

Figure 4.4: *Typical measured voltage and current waveforms for Finemet material, at charging voltage of* 8.5 kV *and reset current of* 2.5 A*: (a) 1 core, (b) 2 cores, and (c) 3 cores. The same number of turns ($N_t = 5$ double winding) for each measurement was used.*

The procedures of determining the saturation time and BH-curves are illustrated in Figures 4.5(a) and 4.5(b), respectively, where τ_s is the saturation time and τ_w is the current pulse width.

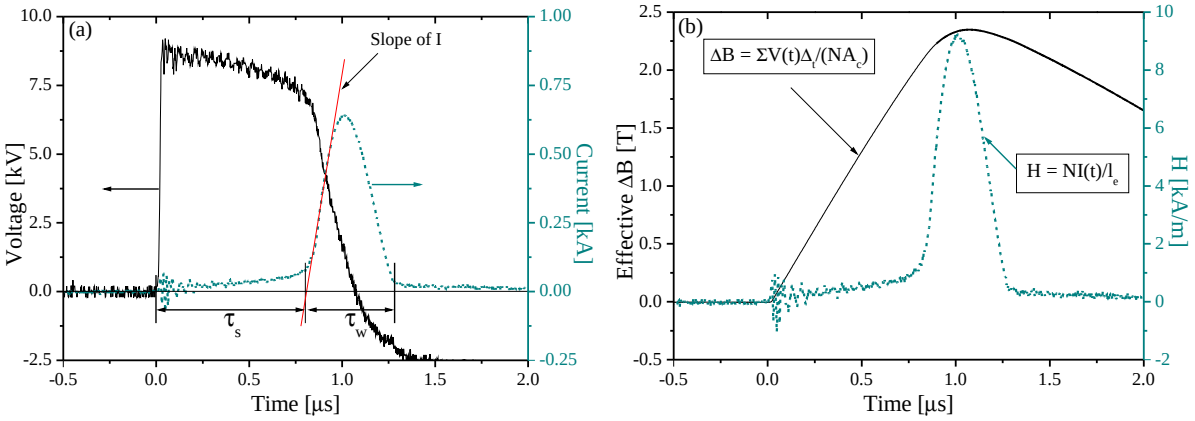

Figure 4.5: *Illustration of the procedure for determining (a) the saturation time, and (b) the BH-curve.*

In order to check the validity of our definition of saturation time, a graph of saturation time as a function of number of magnetic cores was plotted and is shown in Figure 4.6. For the same number of magnetic cores and turns, different saturation times were achieved by varying the excitation voltage as indicated by Equation (3.2.6). As expected, the saturation time increases linearly with increasing number of magnetic cores and it decreases as the excitation voltage increases. This variation also indicates that the saturation time is related to the inductance of the magnetic core(s) (see Equation (3.7.1)). The increase in the number of magnetic cores implies increased inductance and hence large impedance to the flow of the magnetizing current, i.e. longer time to saturation.

Stellenbosch University http://scholar.sun.ac.za

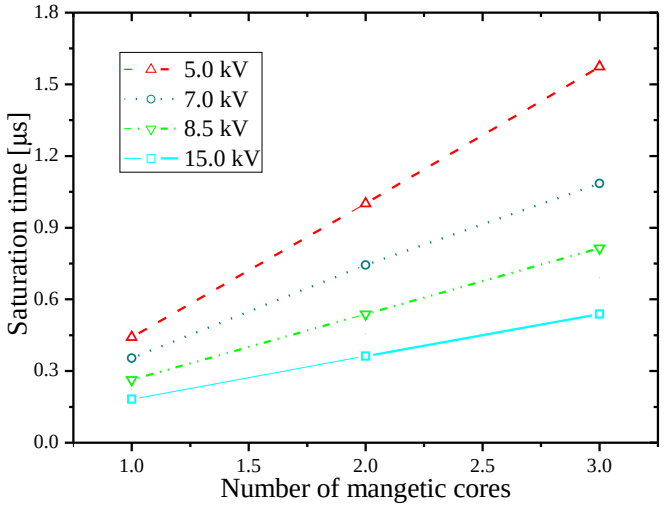

Figure 4.6: *Graphical illustration of the variation of saturation time with number of magnetic cores.*

The derived initial magnetization BH-curve for the Finemet magnetic core with different number of cores is shown in Figure 4.7. The BH-curves are calculated using Equations (4.4.1) and (4.4.2) as illustrated in Figure 4.5(b). The measured effective magnetic flux density change of the Finemet material is approximately 2.2 T, which corresponds to a magnetic field H of 6000 A/m.

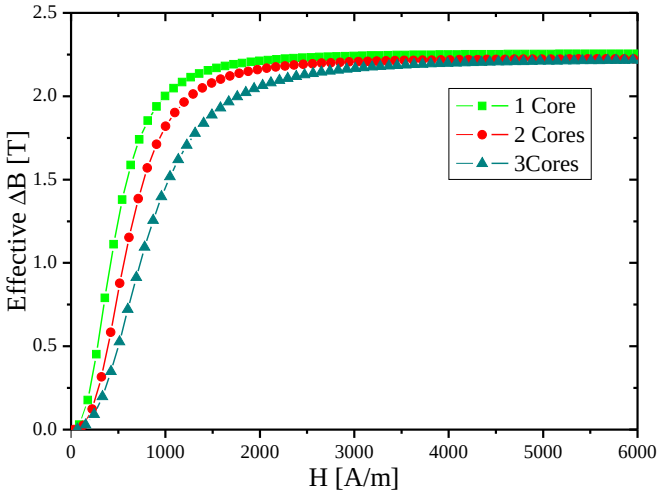

Figure 4.7: *Initial magnetization BH-curves for Finemet material with different number of magnetic cores.*

In Figure 4.7, as the number of magnetic cores increases, the magnetization curve rises, though at a slower rate. This behaviour can be explained as follows: as the number of magnetic cores increases, the magnetization force required to saturate the cores also increases. This is due to the fact that with the high number of magnetic cores, eddy current losses and magnetic viscosity effects are expected to be high. These have serious effects on magnetic core losses resulting in slight changes of the shape of the magnetization curve.

Figure 4.8 shows the relative permeability curves for different numbers of Finemet magnetic cores. The curves were derived from Equation (3.2.8) using the data in Figure 4.7. As the

Stellenbosch University http://scholar.sun.ac.za

number of magnetic cores increases, the relative permeability curves becomes higher, i.e. the permeability of 3 cores is higher than that of 2 cores, which in turn is higher than for 1 core. The relative permeability decreases to approximately 296 at a magnetic field of 6000 A/m.

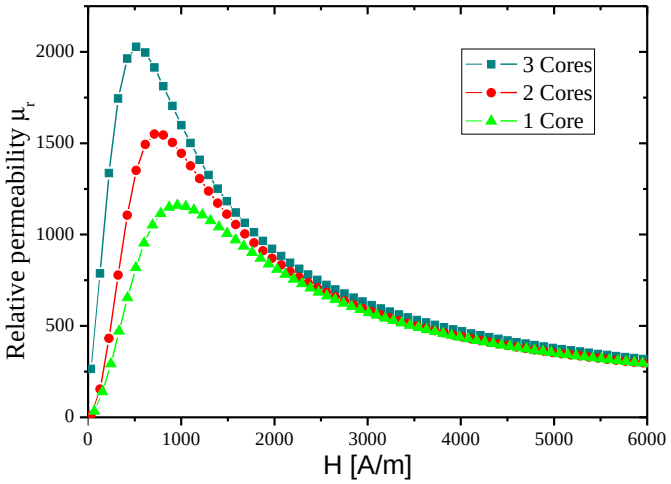

Figure 4.8: *Relative permeability curves for different number of magnetic cores calculated using the data in Figure 4.7.*

The energy transfer in circuits involving magnetic switches has part of the input energy consumed in the form of core losses, i.e. eddy current and hysteresis losses. Using Equation (4.4.3), we calculated the core losses over the first cycle of the experimental data for different number of Finemet magnetic cores. The half cycle core losses as well as the input charging energy as a function of saturation time with different number of cores is given in Figure 4.9. The input charging energy was evaluated using $E_{in} = \frac{1}{2}CV^2$, where $C \cong 10\,\text{nF}$. The charging voltage V across the capacitor was varied from ~ 5 to $\sim 15\,\text{kV}$. Varying the input charging voltage, we are able to obtain different saturation times. It can be seen in Figure 4.9 that part of the input energy is consumed as core loss. The core loss in the 3 core case is slightly higher than that of 2 cores, which in turn is higher than for 1 core. This is consistent with the fact that the initial BH-curve for the 3 cores is also broader.

Table 4.2 summarizes the typical measured properties of the three magnetic cores evaluated. In the table, it can be seen that FT-1H has the highest half cycle core loss density, however, it also has the lowest loss factor.

Parameter	**FT–1H**	**Ferrite**	**VAC 6030Z**
Effective magnetic flux swing, ΔB_{eff} [T]	2.2	0.51	1.42
Half cycle core loss density, P_c [Jm^{-3}]	430	70	335
Loss factor, L_f [$\text{Jm}^{-3}\text{T}^{-2}$]	101	272	156

Table 4.2: *Measured dynamic properties of the magnetic core materials at a saturation time of* 1.0 μs.

Stellenbosch University http://scholar.sun.ac.za

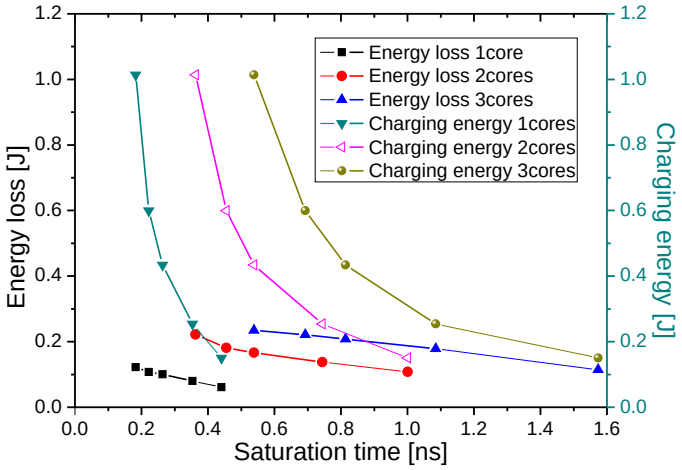

Figure 4.9: *Energy loss and charging energy as a function of saturation time for different number of magnetic cores.*

Figure 4.10 compares the measured BH-curves for the three studied magnetic core materials at a magnetization force of 6000 T.

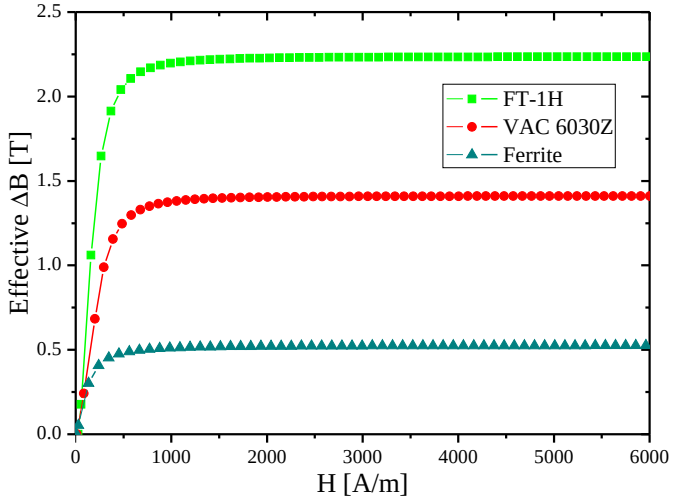

Figure 4.10: *Derived magnetization BH-curves for three different materials at a saturation time of* 1.0 μs.

The curves in Figure 4.10 have slightly different slopes due to the different leakage current characteristics (unsaturated state) and almost the same slopes during the saturated state. Using the data in Figure 4.10, the relative permeability curves for each material at a saturation time of 1.0 μs have been determined and the results are shown in Figure 4.11. As expected, the permeability curve of the Finemet FT–1H material is higher than that of VAC 6030Z, which in turn is higher than of ferrite. The ferrite curve, however, is reduced to a slightly lower value (approximately 70) than that of FT–1H.

Stellenbosch University http://scholar.sun.ac.za

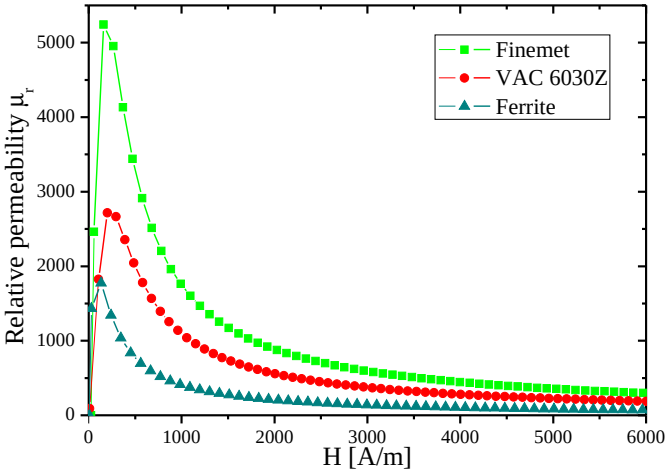

Figure 4.11: *Relative permeability curves for three different materials calculated using the data in Figure 4.10 at a saturation time of* 1.0 μs.

The variation of magnetic core loss per core volume (core loss density) as a function of saturation time over the first cycle of the experimental data for the three materials is given in Figure 4.12. For each material, the core loss density was calculated using Equation (4.4.4), and the saturation time was determined as explained in Section 4.4.

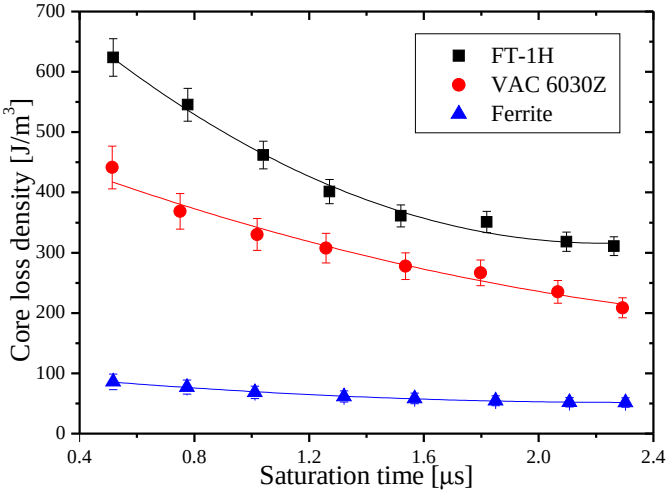

Figure 4.12: *Half cycle core loss density as a function of saturation time for different magnetic core materials.*

In Figure 4.12, all the materials show an inverse relationship between core loss density and saturation time. The Finemet material has a much higher core loss density than the other two materials. This behaviour can be explained by utilizing the eddy current loss formula given in Equation (3.2.14), i.e. $P_e \propto 1/\rho$ and the static data given in Table 3.1, wherein the resistivity of the Finemet material is much smaller than any of the other two materials.

Although Figure 4.12 shows that the FT–1H material has high core loss density, this result is not sufficient for comparison between competing materials. This is because the most important parameter, i.e. effective maximum flux density change ΔB, which is key to magnetic switching

Stellenbosch University http://scholar.sun.ac.za

is not taken into account. For example, it can be observed in Figure 4.10 that ΔB of Finemet material is approximately four times that of ferrite. Therefore, a parameter such as a loss factor which includes ΔB is more effective in core-to-core comparison. Figure 4.13 shows the graph of loss factor as a function of saturation time. In the figure, the Finemet material shows a lower loss factor as compared to the other materials. The lowest loss factor implies that Finemet FT-1H is the most efficient material amongst the three material studied in our experiments.

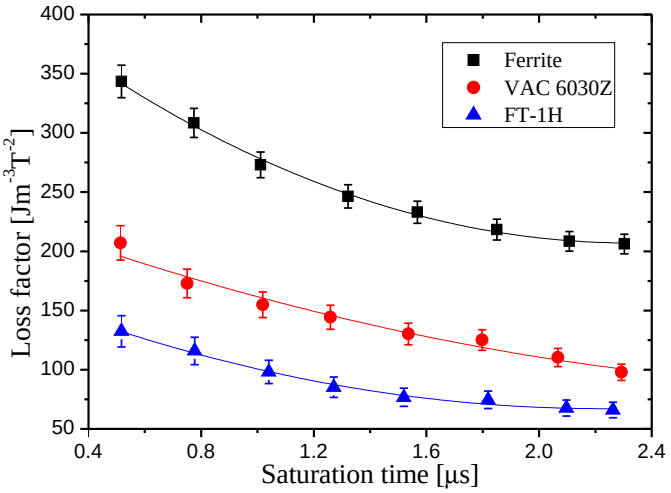

Figure 4.13: *Loss factor for material comparison.*

4.6 Summary

This chapter was set out to provide information about the different magnetic core materials that can be used in the development of magnetic pulse compressors for the excitation of TEA CO_2 lasers. The core loss measurements in our experiments have shown that Finemet FT-1H has the highest core loss density as compared to ferrite and amorphous metals. However, overall, FT-1H has clear advantages of the least loss factor as well as the highest available magnetic flux density change and relative permeability. By using these FT-1H cores, it is possible to design an optimized magnetic pulse compressor in terms of reduced total core losses and required core volume. In the next chapter, a pulsed power supply constructed using FT-1H magnetic cores will be described.

Stellenbosch University http://scholar.sun.ac.za

Chapter 5

Laser pulsed power supply

5.1 Introduction

In the previous chapters, we have already mentioned that thyratron or spark gap-based excitation circuits can no longer meet the demands of high repetition rate industrial TEA CO_2 lasers. This is because of the limited lifetime of both thyratron and spark gap switches. The use of solid-state switches is the only potential solution for obtaining long term reliability and lifetime expectancy of these new high power lasers. In this chapter, we describe an all solid-state switched excitation circuit for pumping a TEA CO_2 laser. The circuit was designed as a direct replacement of an existing thyratron-based excitation circuit. The chapter begins with a list of the design specifications of the excitation circuit. This is followed by the equivalent electrical circuit of the design topology. A brief description of the circuit components is given. The design procedures/results are given, and finally the initial test measurements of the pulsed power supply are presented towards the end of the chapter.

5.2 Electrical design specifications

Like any other scientific design project, there are projected design specifications and goals that must be met. The design specifications of the excitation circuit described in this study were obtained from the desired operation parameters of the main switch and the laser requirements, and are summarized in Table 5.1.

Parameter	**Value**	**Unit**
Peak voltage at the laser head	44	kV
Pulse energy delivered to the laser	13	J
Electrode voltage rise time (10%–90%)	<150	ns
Pulse repetition rate up to	600	Hz
Pulser timing jitter	< 50	ns
Thermal management	Oil cooled	NA

Table 5.1: *Design specifications of the TEA CO_2 laser excitation circuit.*

The excitation circuit components were designed using new materials (Finemet, FT-1H), to deliver the specified output pulse energy at minimum capital cost, and to minimize the complexity and physical dimensions of the circuit.

Stellenbosch University http://scholar.sun.ac.za

5.3 Excitation circuit topology

Several circuit topologies which can be used to pump a TEA CO_2 laser have been discussed in Section 3.6. An LC-inversion circuit topology with a fast step-up pulse transformer and two stages of magnetic pulse compression was used in this study. The topology offers many advantages. For example, it reduces the required primary switching voltage to half. The simplified equivalent electrical schematic diagram of the excitation circuit based on all solid-state switched technology is depicted in Figure 5.1. It consists of the following: a charging unit, an insulated gate bipolar transistor (IGBT) as the main switch with associated driver and protection circuits (i.e. snubbers and magnetic assist), low inductance energy storage capacitors (C_1, C_2, C_3 and C_p), a fast step-up pulse transformer (PT), reset circuit, two stages of magnetic pulse compression (MPC1 and MPC2) and the laser head. The working principle of the circuit is similar to that described in Section 3.6.

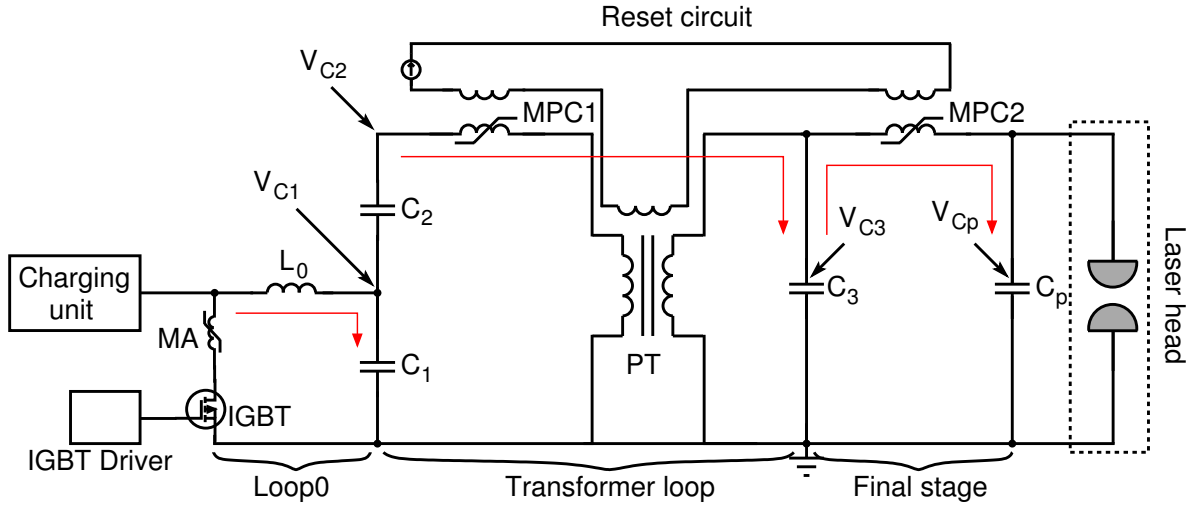

Figure 5.1: *Equivalent electrical schematic circuit design of a pulsed power supply topology based on all solid-state switched technology. The power supply consists of: a charging unit, resonant charging inductor L_0, magnetic assist MA, insulated gate-bipolar transistor IGBT, IGBT driver, 1:12 step-up pulse transformer PT, magnetic switches labelled MPC1 and MPC2; where $L_0 = 1.4\mu$H, $C_1 = 3.74\mu$F, $C_2 = 3.3\mu$F, $C_3 = 13.1$nF, $C_p = 13.4$nF.*

5.3.1 Charging unit

The storage capacitor bank charger is a conventional DC high-voltage power supply (TDK-Lambda, model: 202A–3 kV). It uses a resonant inverter topology for efficient generation of output power and has features of external command charging. The average charging rate of the charger is 2 kJ/s.

Stellenbosch University http://scholar.sun.ac.za

5.3.2 Capacitors

The storage capacitor bank was realized using two capacitors C_1 and C_2 assembled using snubber capacitors (Wima, 0.22 μF, 50 kV). The stage capacitor C_3 and the peaking capacitor C_p utilized ceramic capacitors (TDK, 50 kV, 1.7 nF). The peaking capacitor is identical to the one of the original thyratron-based power supply.

5.3.3 Main switch

The main switch used is the state-of-the-art IGBT (Infineon FZ1500R33HL3) rated for peak voltage of 3.3 kV and DC average current of 1.5 kA. The choice of an IGBT rather than fast switching MOSFETs was based on the fact that IGBTs have well balanced characteristics in terms of power capability and switching frequency. Moreover an IGBT switch has properties of both a power bipolar transistor and a power MOSFET [20]. The summary of the characteristics of the IGBT switch used are given in Table 5.2.

Parameter	**Specification**
IGBT module	Infineon FZ1500R33HL3
Hold-off voltage	3.3 kV
Peak switching current	1.5 kA
Turn-on delay time	0.50 μs
Turn-off delay time	4.10 μs
Turn-on energy losses per pulse	2.3 J
Turn-off energy losses per pulse	2.4 J

Table 5.2: *Summary of the IGBT switch ratings .*

The operating voltage level for the IGBT switch was designed at 2.3 kV to keep within the adequate safety margin of the switch and to generate pulse widths of 7.3 μs. Now, using the LC-inversion circuit, the voltage is doubled to 4.6 kV. This voltage is then stepped up by a fast pulse transformer with a 1:12 turn ratio to achieve the desired voltage level across the laser head. Since the switch has a slower switching time (turn-on delay time) than the specified electrode voltage rise time (150 ns or less), at least two stages of MPC are necessary. To reduce the turn-on losses in the IGBT, a magnetic assist (MA) was used. A single magnetic core (toroidal shape) was utilized to fabricate the MA with 10-turn double winding using solid copper wire. The magnetic core material is Finemet FT-1H. The core has the following dimensions; outer diameter 140 mm, inner diameter 89 mm, height 10 mm and packing factor 0.76.

5.3.4 Magnetic pulse compressor

The magnetic switches for the two compression stages are denoted by MPC1 and MPC2 for the first stage and second stage, respectively. The design parameters of each of the magnetic

Stellenbosch University http://scholar.sun.ac.za

switches were determined according to the principle outlined by Druckmann et al [55] and using a spreadsheet-aided design procedure [49]. The design results are given in details in Section 5.4. The magnetic switch for each stage was fabricated using Finemet FT-1H magnetic cores. The dimensions and static properties of the core are summarised in Table 5.3.

Parameter	**Specification**
Type	Finemet FT-1H
Saturation flux density, B_{sat}	1.265 T
Outer core radius, r_o	10.5 cm
Inner core radius, r_i	5.1 cm
Core height, h	2.5 cm
Core packing factor, p	0.76
Magnetic core volume, V_{mag}	661.6 cm^3

Table 5.3: *Dimensions and static properties of the Finemet (FT-1H) magnetic core material.*

The magnetic switch MPC1 utilized a single magnetic core with windings of 4 turns. The resulting compression ratio of the switch is 4.5. The second magnetic switch MPC2 with windings of 5 turns utilized two magnetic cores which are identical to the one used in MPC1. The compression ratio of the second magnetic switch is 10, giving the overall compression ratio of 45. This results in a current transfer time of 7.3 μs and a peak current of $\sim$ 1.52 kA for the IGBT switch. These values are well within the switch specifications.

5.3.5 Pulse transformer

The high peak voltage level required across the laser head (see Table 5.1) can be reached by employing a fast step-up pulse transformer or several series connected switches or combinations of both as was mentioned in Section 3.6. However, because of the resulting circuit complexity, series connected switches were avoided and instead a pulse transformer was used. In Figure 5.1, the pulse transformer was inserted after the first MPC stage. This arrangement yields several advantages. For example, the requirements for the magnetic core material of the transformer are minimized because of the shorter hold-off time. Additionally, it also fulfils the desire to operate some of the circuit components at the lowest voltages possible. Since the pulse time is reduced (short hold-off time), a low leakage inductance design of the transformer is required. Therefore, the transformer described here was developed based on a novel design which ensures low leakage inductance as well as sufficient voltage insulation. The primary and secondary windings were constructed on printed circuit boards (PCBs). Such a design makes the construction easy. Two separate boards were used for the primary side and the secondary side of the transformer to achieve sufficient voltage insulation. The transformer consists of 12 parallel primary turns and 12 secondary turns connected in series, which yields a transformer ratio of 1 : 12. It uses a single magnetic core of the same parameters as those utilized in MPC1 and MPC2. This material

Stellenbosch University http://scholar.sun.ac.za

has relatively high flux density (2.53 T), hence less magnetic core volume of the transformer is required.

5.3.6 Reset circuit

After each excitation process, the magnetic cores of MPC1, MPC2 and the pulse transformer must be returned to their initial state on the BH-curve prior to the next excitation process. In order to make use of maximum ΔB of the materials and minimize the required magnetic core volume, the cores should be reset into reverse saturation. A DC reset circuit which couples each of the magnetic cores with a central copper tube was used. The tube serves as a single non-contacting turn through the magnetic cores. The voltage applied to the magnetic core by the reset circuit drives the core into reverse saturation. Once in reverse saturation, the magnetic core is biased at this point by the magnetic field generated by the DC reset current. The central copper tube was designed to serve two purposes. First as a single turn reset winding, and also to provide forced oil flow for cooling the magnetic cores.

5.3.7 Thermal management

The high voltage components C_1, C_2, C_3 and C_p, MA, L_0, MPC1, MPC2 and voltage pulse transformer are immersed in transformer oil contained in a rectangular Al enclosure for high voltage insulation and to keep the temperature of the components as low as possible. An oil-to-water heat exchanger is used to remove heat from the transformer oil. Well designed cooling channels into the magnetic switches and the pulse transformer were used to provide easy flow of oil across the magnetic cores.

5.4 Design procedure

The most simple and effective design procedure of MPC circuits is by using a spreadsheet in an iterative mode [49]. In a spreadsheet-aided design, the circuit parameters such as stage voltage, current, inductance, etc., can be easily calculated. The design starts from the final output parameters (i.e. pulse energy, output voltage and voltage rise time) and then works backwards. Subsequently starting from the output stage, the parameters of each of the connected input stages are calculated successively back to the primary switch loop. This design procedure is similar to the MPC design algorithm of Druckmann et al [55]. The design parameters calculated using a spreadsheet-aided design procedure for our proposed circuit topology in Figure 5.1 are summarized in Table 5.4.

The gray shaded cells in Table 5.4 show the design input parameters. The primary switch loop, the transformer loop and the final stage loop are represented by the columns loop0, transformer, and final stage, respectively, as depicted in Figure 5.1. Optimization of the parameters in the spreadsheet has been done using design approach II discussed in Section 3.5. The design

Stellenbosch University http://scholar.sun.ac.za

Circuit parameters	Symbol	Unit	Final stage	Transformer	Loop0
Output pulse energy	E_{out}	J	13.0	13.68	7.20
Output voltage	V_{out}	V	-44000	-45726	-3960
Transfer time	τ_{n}	s	152.0E-9	1.53E-6	7.3E-6
Output capacitance	C_{n}	F	13.4E-9	13.1E-9	3.67E-6
Input pulse energy	E_{in}	J	13.68	14.40	7.58
Input voltage	V_{in}	V	-45726	-3960	2031
Input capacitance	$C_{\text{n-1}}$	F	13.09E-9	1.84E-6	3.67E-6
Losses in the loop	P	%	5.0	5.0	5.0
Dumping coefficient	α	1/s	168.73E+3	16.74E+3	3.51E+3
Equiv loop resistance	R	Ω	0.240	0.018	0.020
Total loop inductance	L_{n}	H	353.15e-9	255.74e-9	1.47e-6
Parasitic stray inductance	L_{par}	H	70.0E-9	20.0E-9	NA
Saturated inductance	L_{sat}	H	283.15E-9	75.74E-9	NA
Core parameter (toroidal)					
Core material	NA	NA	Finemet	Finemet	Air core
Number of cores	N_c	NA	2	1	NA
Outer core radius	r_o	m	0.105	0.105	NA
Inner core radius	r_i	m	0.051	0.051	NA
Core height	h	m	0.025	0.025	NA
Inter core clearance	dh	m	0.003	0.003	NA
Radial clearance	dr	m	0.005	0.002	NA
Packing factor	p	NA	0.76	0.76	NA
Max flux density swing	ΔB	T	2.53	2.53	NA
Saturation permeability	μ_{sat}	NA	1	1	1
Saturation flux density	B_{sat}	T	1.26	1.26	NA
Magnetic x-section	A_{mag}	m^2	2.05E-3	1.03E-3	NA
Magnetic core volume	V_{mag}	m^3	1.32E-3	661.62E-6	NA
Volt-second product	Φ	Vs	25.96E-3	10.38E-3	NA
Number of turns	N	NA	5	4	NA
Transformer parameters					
Core material	NA	NA	NA	Finemet	NA
Number of cores	N_c	NA	NA	1	NA
Transformer ratio	n	NA	NA	12	NA
Outer core radius	r_o	m	NA	0.105	NA
Inner core radius	r_i	m	NA	0.051	NA
Core height	h	m	NA	0.025	NA
Packing factor	p	NA	0.76	0.76	NA
Max flux density swing	ΔB	T	NA	2.53	NA
Magnetic x-section	A_{mag}	m^2	NA	1.03E-3	NA
Magnetic core volume	V_{mag}	m^3	NA	661.62E-6	NA
Leakage inductance	L_{leak}	H	NA	160.0E-9	NA
Miscellaneous					
Pulse compression ratio	C_{r}	NA	10.08	4.77	NA
Peak current	I_{peak}	A	2938	3542	1525
Voltage rise-time (10%–90%)	t_{rise}	s	108.20E-9	1.1E-6	5.2E-6
Max rate of current rise	dI/dt	A/s	121.45E+9	1.21E+9	1.311+9

Table 5.4: *Spreadsheet-aided design parameters for the LC-inversion pulsing circuit.*

Stellenbosch University http://scholar.sun.ac.za

results from the spreadsheet are very promising, with output current pulse durations of 152 ns corresponding to a voltage rise time (10%–90%) of 108 ns, which is even much faster than the specified value. It should be noted that some of the input parameters such as parasitic stray capacitance, loop losses, etc., are very difficult to predict in advance. These can be better estimated after finalising the construction details of the pulsed power supply. However, to facilitate the spreadsheet-aided design calculation, these parameters have been roughly estimated. For example the total losses, including magnetic core and conduction losses can be estimated to be approximately 5% of energy transferred in a particular stage.

5.5 Pulse transformer measurements

Three parameters of the pulse transformer were measured. These are the total leakage inductance, the primary magnetization inductance and the secondary magnetization inductance. The test set-up for measuring the total leakage inductance is shown in Figure 5.2.

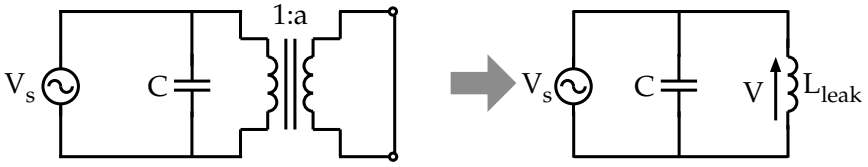

Figure 5.2: *Test setup for measuring the leakage inductance of the pulse transformer; a is the transformer ratio.*

A capacitor C is connected in parallel with the primary side of the transformer, and the secondary side is short-circuited. The equivalent circuit inductance in parallel with the capacitor is the total leakage inductance, denoted as L_{leak}. The assumption here is that the total leakage inductance of the transformer is much smaller than the magnetization inductance. A function generator is used to generate sinusoidal signals, which drives the circuit with a resonant frequency given by $f_0 = 1/(2\pi\sqrt{L_{\text{leak}}C})$. At f_0 the impedance of the resonant circuit is maximum, thus the voltage across the primary side of the transformer is maximum. The measured value of f_0 is then used to calculate the total leakage inductance. The test set-up for measuring the magnetization inductance is the same as that in Figure 5.2, except that in this case one side of the transformer is left open instead of short circuiting. For example, to measure the primary magnetization inductance, the secondary side is left open and vice-versa. The equivalent circuit inductance which is in parallel with the capacitor is the magnetization inductance with reference to the side were the capacitor is connected. As before, the magnetization inductance is determined from the measured resonant frequency, using the equation $f_0 = 1/(2\pi\sqrt{L_{\text{mag}}C})$. The summary of the calculated values of the total leakage inductance and the primary and the secondary magnetization inductances are given in Table 5.5.

The total leakage inductance (140 nH) is close to the one estimated in Table 5.4 using a spreadsheet-aided design procedure. This value is very low, which confirms that the design used in the pulse transformer is good.

Stellenbosch University http://scholar.sun.ac.za

Parameter	Value
Total leakage inductance	140 nH
Primary magnetization inductance	40 μH
Secondary magnetization inductance	5.7 mH

Table 5.5: *Summary of the transformer measurements.*

5.6 Electrical measurements and discussion

The power supply was tested with a commercial TEA CO_2 laser head, previously run by a thyratron-based pulsed power supply. A pulse repetition rate of 3 Hz, optimized gas mixture of 5:1:4 (He:N_2:CO_2) and gas pressure of 0.983 bar were used. The voltage at different points of the power supply as indicated in Figure 5.1 and the inversion current were monitored using a high voltage probe (model: Tektronix P6015A) and a fast Pearson pulse current transformer (model: 1025, sensitivity 0.025 V/A). The data was recorded with an oscilloscope (model: Tektronix TDS1012) and then transferred to a personal computer for calculations and analyses. The preliminary test measurements and discussion are presented in this section.

5.6.1 IGBT voltage and current measurements

The voltage across the IGBT switch and the current through the IGBT at the time of turn-on were measured for two cases, i.e. without magnetic assist and with a magnetic assist. The voltage and current waveforms in both cases are shown in Figure 5.3. The switching voltage was set to 1.9 kV giving rise to a current pulse width 7.2 μs.

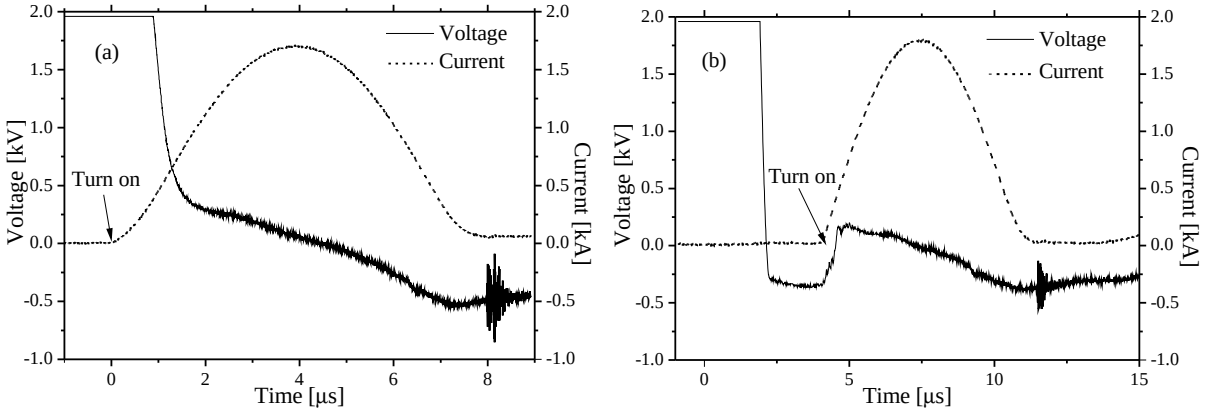

Figure 5.3: *Typical measured IGBT voltage and current waveforms: (a) without magnetic assist, and (b) with magnetic assist.*

In the case without a magnetic assist, it can be seen in Figure 5.3(a) that the current starts rising when the switch is still not fully turned on and the switch voltage is still high. In that case, the power dissipated in the IGBT during turn-on can be very high, hence high turn-on losses. The turn-on losses can be evaluated by integrating the product of the voltage and current through

Stellenbosch University http://scholar.sun.ac.za

the switch over the whole range of the measurement period. The results of the IGBT turn-on loss calculation using the waveforms in Figure 5.3 are summarized in Table 5.6.

Parameter	**Without magnetic assist**	**With magnetic assist**
Hold-off time [μs]	0	3.85
IGBT loss [mJ/pulse]	1300	345
Magnetic assist loss [mJ/pulse]	0	278
Total losses [mJ/pulse]	1300	623

Table 5.6: *Calculated IGBT turn-on losses and that expended in the magnetic assist.*

As expected, the losses are larger in the case without a magnetic assist. The magnetic assist holds off the current for about 3.85 μs during which time the switch voltage reduces to a lower value and this minimizes the turn-on losses in the switch. The magnetic assist loss is estimated using the method described Section 4.4. In Figure 5.3(b), voltage oscillation after turn-on of the switch can be observed. This could be as a result of increased inductance of the switch loop. The inductance of the switch loop was reduced and the voltage drop also reduced significantly as shown in Figure 5.4 at a switching voltage of 2.0 kV. The estimated magnetic assist loss in this case is about 125 mJ and the overall losses are reduced.

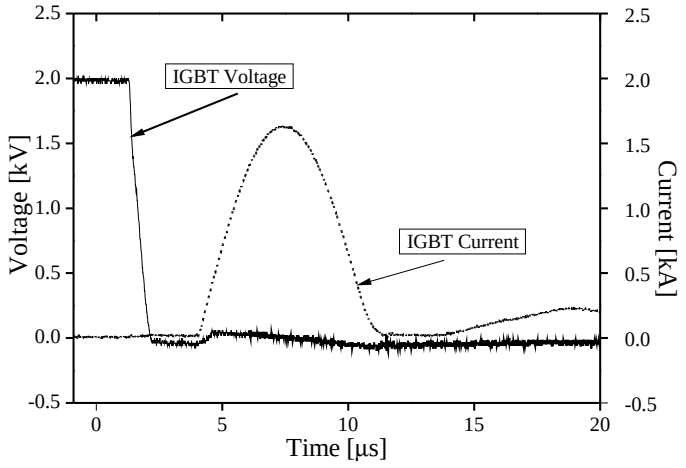

Figure 5.4: *IGBT voltage and current waveforms with low inductance magnetic assist.*

5.6.2 MPC voltage and current measurements

The voltages were monitored across the capacitors C_1, C_2, C_3 and C_p (i.e. electrode voltage). Only the inversion current (current through the IGBT switch) could be measured because of the difficulty in inserting the current monitor in the power supply loops. The measured voltage and current waveforms are shown in Figure 5.5. The charging voltage was set at 1.9 kV. The voltage across C_1, C_2, and the current through the IGBT switch were scaled by a factor of 10. When the IGBT switch was triggered, the voltage across C_1 was inverted by the current I_{INV} and that across

Stellenbosch University http://scholar.sun.ac.za

C_2 almost doubled the charging voltage (approximately 3.76 kV) but with negative polarity. The voltage inversion time was about 6.0 μs. During this time, the magnetic switch MPC1 was unsaturated, thus presenting large impedance to the flow of current in the circuit. After the voltage inversion was complete, MPC1 turned on and the energy stored in both C_1 and C_2 was transferred to C_3 with a transfer time of about 1.1 μs. The peak voltage across C_3 was about 42 kV which is a result of voltage amplification by the pulse transformer (turn ratio = 1:12). Upon saturation of the second magnetic switch MPC2, C_3 rapidly transfers its energy to the peaking capacitor C_p in a time less than 0.2 μs.

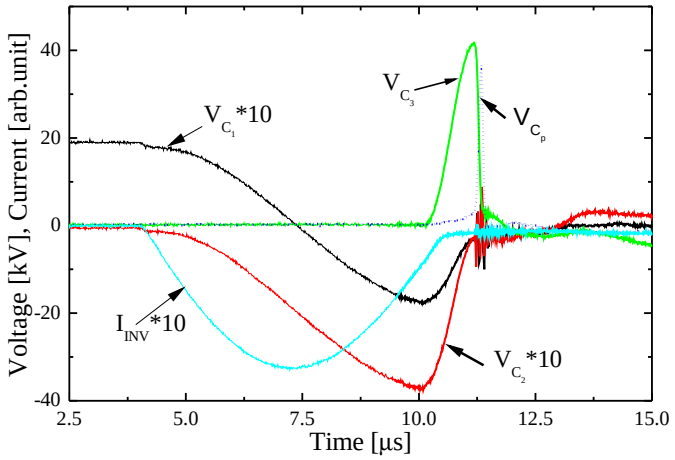

Figure 5.5: *Typical measured voltage and current waveforms at a charging voltage of* 1.9 kV. *The voltages across C_1 and C_2, and the inversion current I_{INV} are scaled by a factor of 10 for clarity.*

Figure 5.6 shows the voltage waveform across the discharge electrodes which in principle is the same as that across the peaking capacitor. The peak electrode (breakdown) voltage is approximately 37 kV and the electrode voltage rise time (10%–90%) is about 110 ns. This value is very close to that calculated in Table 5.4 ($\sim$ 108 ns).

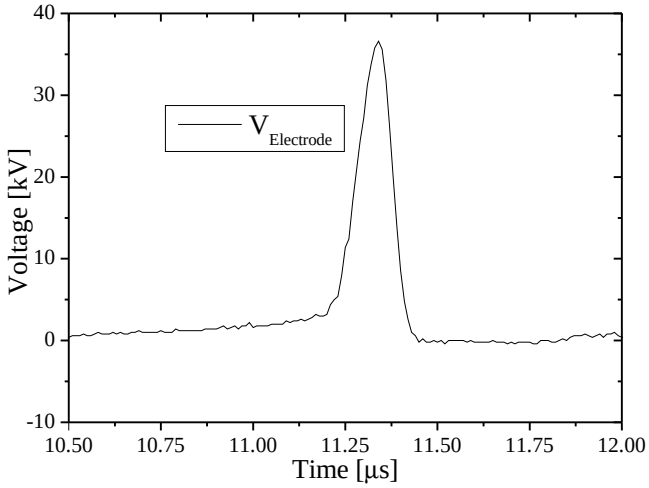

Figure 5.6: *Measured electrode voltage pulse with an applied charging voltage of* 1.9 kV.

Stellenbosch University http://scholar.sun.ac.za

Higher peak voltage could be obtained by increasing the charging voltage up to 2.0 kV. For the initial test measurements, the power supply was operated at somewhat lower parameters than the design specifications in order to ensure safe operation of the system. The summary of the measured operating parameters of the power supply at a charging voltage of 1.9 kV is given in Table 5.7. The energy stored in the capacitors and the energy transfer efficiency have been calculated using $E = \frac{1}{2} C_i V_{Ci}^2$ and $\eta = \frac{1}{2E_0} C_i V_{Ci}^2$, respectively, where $i = 1, 2, 3, p$, and E_0 is the initial input energy.

Parameter	C_1	C_2	C_3	C_p
Charging time [μs]	6.05	6.0	1.06	0.18
Discharge time [μs]	1.08	1.1	0.18	0.11
Peak voltage [kV]	1.9	3.76	42.0	37.0
Stored energy [J]	6.75	23.3	11.6	9.17
Energy transfer efficiency [%]	100	98	93	74

Table 5.7: *Measured operating parameters of the of the excitation circuit at a charging voltage of* 1.9 kV.

Due to impedance mismatch between the excitation circuit and the laser head, some of the energy can be reflected back into the system. The reflected energy is indicated by the oscillations in the voltage and current waveforms as can be seen in Figure 5.5. In principle, this energy should be damped out before the arrival of the next pulse to prevent potential damage of the system. In order to check the validity of this assumption, measurements of voltage and current were taken at longer time scales and the results are shown in Figure 5.7. It can be noticed that the oscillations are reduced after approximately 63 μs, which is shorter than the inter-pulse time at maximum repetition rate of 600 Hz.

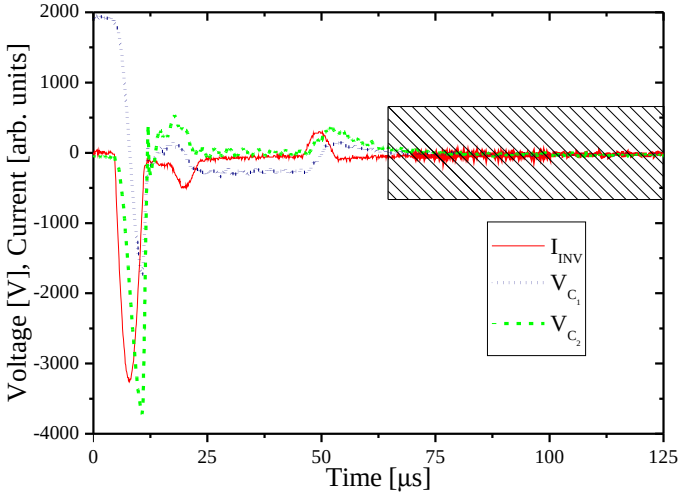

Figure 5.7: *Typical voltage and current waveforms across C_1 and C_2, measured at longer time-scale. The shaded region indicates the area without oscillations.*

Stellenbosch University http://scholar.sun.ac.za

5.7 Summary

In this chapter, we have reported on the initial test measurements of an all solid-state switched pulsed power supply for exciting the TEA CO_2 laser. The system was operated at a pulse repetition frequency of 3 Hz with a laser gas mixture of 5:1:4 (He:N_2:CO_2) and gas pressure of 0.983 bar. According to the initial test measurements, the power supply is capable of matching the expected values based on the numerical design procedure in Table 5.4. Though no laser output measurements are included in this thesis because of patent reasons [61], more electrical test and laser output measurements have been conducted at the Laser Centre of Excellence (PaR Systems Ltd). We have obtained a good report about the system operation even at the full pulse repetition frequency of 600 Hz.

Stellenbosch University http://scholar.sun.ac.za

Chapter 6

Evaluation of a surface corona preionized mini TEA CO_2 laser

6.1 Introduction

In Chapter 2, the common preionization techniques used in the excitation of TEA CO_2 were discussed. It was concluded that corona preionization offers more advantages in the excitation of these lasers. In the present chapter, a miniature TEA CO_2 laser preionized by surface-wire corona discharge is evaluated and compared to the same system preionized by spark preionization. The corona preionizer is constructed using a ceramic tube (AL_2O_3) with a fine wire stretched along the surface of the tube. By applying this extremely efficient yet inexpensive preionizer to the TEA CO_2 laser and varying a number of parameters such as charging voltage, gas pressure, gas mixture and inter-electrode spacing, the performance of the laser was investigated. The results and discussion are presented in this chapter.

6.2 Experimental setup

Figure 6.1 shows the schematic overview of the experimental set-up. It consists of the laser head mounted inside a vacuum-tight laser vessel, an excitation circuit (high voltage pulsed power supply), a DC high-voltage power supply, gas system, laser output measuring diagnostics and a control system. The control system is used to regulate the charging voltage and pulse repetition frequency. It is based on a micro-processor chip which has the facility to handle feedback error from the primary switch driver through fibre-optic cables. The DC high-voltage power supply (TDK-Lambda, model: 202A–3 kV) is used to power the excitation circuit. The excitation circuit and the laser head are described in more detail in Subsections 6.2.1 and 6.2.2, respectively. The output pulse energy was measured with the help of an energy meter (ScienTech joule meter, model: PHD50, sensitivity 2.03 V/J). A fast photon-drag detector (model: B749, Hamamatsu Photonics Ltd) was used to monitor the laser pulse waveform. The discharge voltage was monitored using a high voltage probe (model: Tektronix P6015A, 1×1000). The discharge voltage, output pulse energy and laser pulse signals were all displayed and recorded using a Tektronix-type oscilloscope (model: TDS1012).

Stellenbosch University http://scholar.sun.ac.za

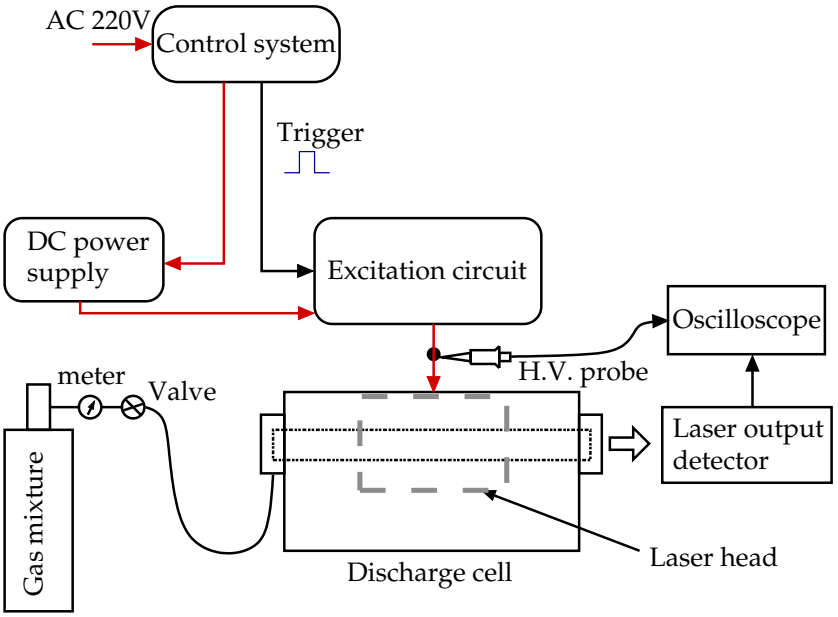

Figure 6.1: *Schematic overview of the experimental setup.*

6.2.1 Excitation circuit

The schematic diagram of the excitation circuit is shown in Figure 6.2. The circuit was developed by Timo Stehmann [62], initially for pumping a spark array preionized mini TEA CO_2 laser. It consists of a DC high-voltage power supply, a storage capacitor bank C_0, a charging inductor L_0, an IGBT switch of similar ratings as the one used in Chapter 5, a step-up voltage pulse transformer (turn ratio = 1:14) and two stages of magnetic pulse compression (MPC) network. The peaking capacitor C_p is connected in parallel and close to the laser head.

As soon as C_0 is resonantly charged to a maximum voltage from the DC high-voltage power supply, the IGBT switch is triggered, and the energy stored in C_0 is transferred to the input capacitor C_1 of the first MPC stage through the pulse transformer. The voltage build up across C_1 saturates MPC1, and the energy stored in C_1 is transferred to C_2. This process is repeated at MPC2, whereby C_2 transfers energy to C_p upon saturation of MPC2, which eventually discharges into the laser medium. This excitation circuit can generate peak voltages up to 30 kV across the discharge electrodes at a charging voltage of 2.2 kV depending on the gas mixture and pressure.

As already indicated in the previous chapters, the energy transfer from the storage capacitor to the laser medium involve losses in the different circuit elements. These losses reduce the overall efficiency of the laser system. Comparing the input energy into charging the capacitor C_0 to the output pulse energy yields the over-all efficiency of the laser as will be shown later.

6.2.2 The laser head

As shown schematically in Figure 6.3, the laser head is housed in a vacuum-tight discharge cell which also includes the gas circulation fan, heat exchanger and externally mounted optics. The

Stellenbosch University http://scholar.sun.ac.za

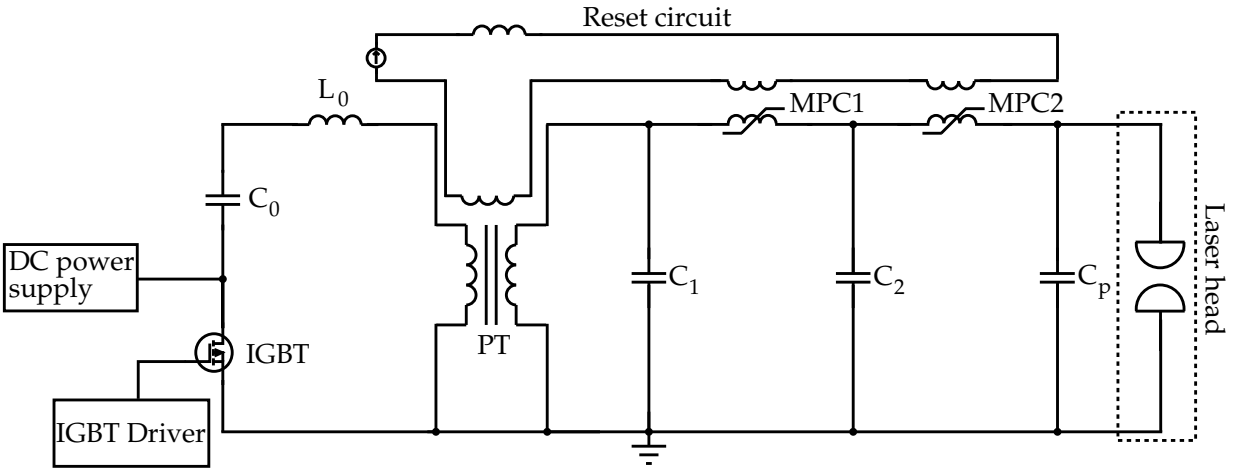

Figure 6.2: *The equivalent electrical excitation circuit of a mini TEA CO_2 laser.* $L_0 = 2.14\,\mu$H, $C_0 = 1.88\,\mu$F, $C_1 = 10.72\,$nF, $C_2 = 11.2\,$nF, $C_p = 3.68\,$nF, *and PT turn ratio = 1:14.*

laser head comprises of two main discharge electrodes and two corona rods which act as the corona preionizer. The electrodes are made of brass and are profiled according to Stappaerts profile [63], with dimensions 200 mm by 25 mm ($l \times w$). The use of such uniform field electrodes allows us to place the corona preionizer close to the discharge region. In our experiment, two corona rods were arranged symmetrically on both sides of the cathode at a distance of 3 mm, and 2.5 mm from the centre line halfway between the electrodes. The inter-electrode separation was initially set at 8 mm thus defining a discharge volume of approximately 40 cm^3. The laser head, consisting of discharge electrodes and corona prionizer assembly, has dimensions of $250 \times 115 \times 65\,$mm^3.

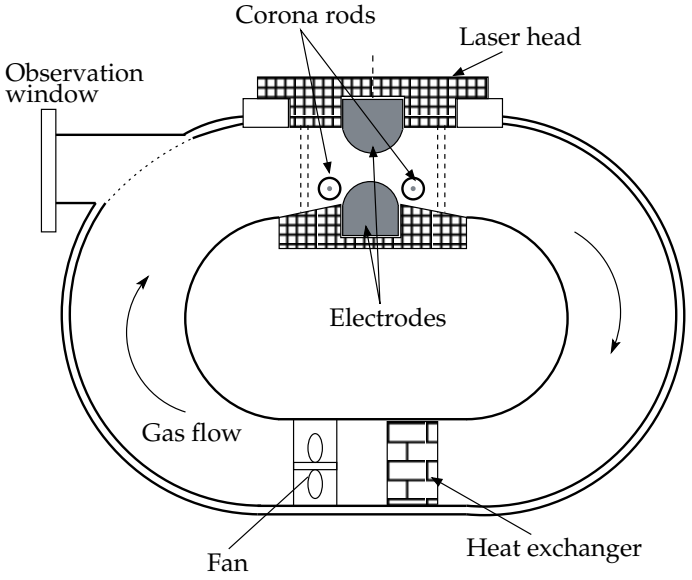

Figure 6.3: *Layout of the mini TEA CO_2 laser discharge cell.*

Preionization of the discharge volume was accomplished by means of uv radiation generated by

Stellenbosch University http://scholar.sun.ac.za

corona discharge at the surface of the corona rods. Figure 6.4 shows the schematic diagram of a surface wire corona rod. It is formed from a ceramic tube (Al_2O_3) of internal diameter 6 mm, wall thickness 1.5 mm and length 225 mm. A copper rod to which a high voltage pulse is applied was inserted inside the ceramic tube and a fine wire (guitar string), electrically grounded and of diameter 200 μm was stretched over the surface of the tube and glued at both ends. When a fast-rising high-voltage pulse is applied across the inner copper rod and the fine wire, a large number of closely spaced surface streamers are developed [23]. This results in a dense corona discharge which spread over the entire surface of the ceramic tube, and is capable of preionizing the laser gas in the discharge volume. Ceramic was employed in this preionizer because it is relatively cheaper and was available in the small size that was needed. In addition to the advantages mentioned earlier in Section 2.3, this kind of preionization has very low energy consumption and is in fact self synchronized, i.e. no additional timing circuit between preionization and main discharge is needed.

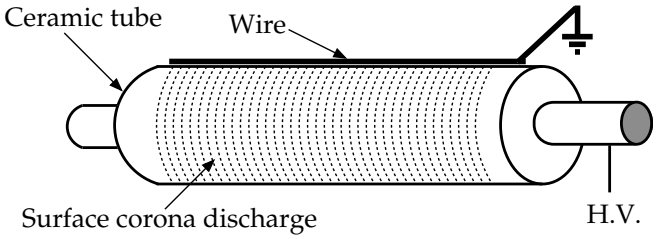

Figure 6.4: *Schematic diagram of a surface-wire corona rod.*

The laser resonator cavity consists of a flat molybdenum mirror of 100% reflectivity and a 15 m curved ZeSe output coupler with 70% reflectivity. The distance between the back reflector and the output coupler (i.e. the optical cavity length) is 51 cm.

6.3 Results and discussion

6.3.1 Discharge voltage and laser pulse waveforms

The laser was initially operated at a pulse repetition rate of 3 Hz with inter-electrode separation of 8 mm. Stable arc-free laser discharges were achieved when the laser was operated within a specified range of charging voltages for a given gas pressure and laser gas mixture. For example, at a gas pressure of 1.0 bar, arc-free discharges could be obtained for charging voltages from 1.4 to 2.04 kV in a gas mixture of 3:1:1 (He:CO_2:N_2). Slightly below or above this voltage range, the discharge tended to be unstable with occasional arcing and in worst cases, multiple arcs were observed. The explanation for this behaviour is as follows: at voltages below threshold, the applied voltage across the discharge electrodes is not enough to cause a fast gas breakdown, while higher voltages results in excess input energy loading into the discharge volume–thus leading to glow-to-arc transition in both cases. For a gas mixture of 8:1:1 (He:CO_2:N_2), the stable operating region was between 1.2 and 1.7 kV at a gas pressure of 1.0 bar. It should be noted

Stellenbosch University http://scholar.sun.ac.za

that the breakdown voltage increases with gas pressure and inter-electrode separation and is significantly higher for rich gas mixtures of 3:1:1 than for the lean 8:1:1 mixture. Figure 6.5 shows the image of an intense bluish uniform glow discharge that was observed in the whole region between the electrodes with the laser operating in stable conditions. The image was recorded by a digital camera.

Figure 6.5: *Visual appearance of the laser discharge, as observed through a side glass window at a gas pressure of* 1.0 bar *(He:CO_2:N_2 = 3:1:1) and charging voltage of* 2.0 kV.

Figure 6.6 shows the discharge voltage and laser pulse waveforms with a rich laser gas mixture of 3:1:1 (He:CO_2:N_2) and gas pressure of 1.0 bar. The discharge voltage reached a value of 24.2 kV with a rise time (10%–90%) of approximately 92 ns. The electrical noise signal at the beginning of the laser pulse in Figure 6.6 is due to the fact that both the voltage and the laser pulse waveforms were recorded simultaneously. The laser discharge is initiated when the electrode voltage reaches the breakdown voltage. In Figure 6.6, the laser oscillation is observed 0.32 μs after the start of the main discharge. The output pulse consists of an initial spike induced by gain-switching, followed by a slowly decaying tail. The output pulse energy was 195 mJ with pulse duration of 73 ns (FWHM) for the tail and total laser pulse length of approximately 1.82 μs.

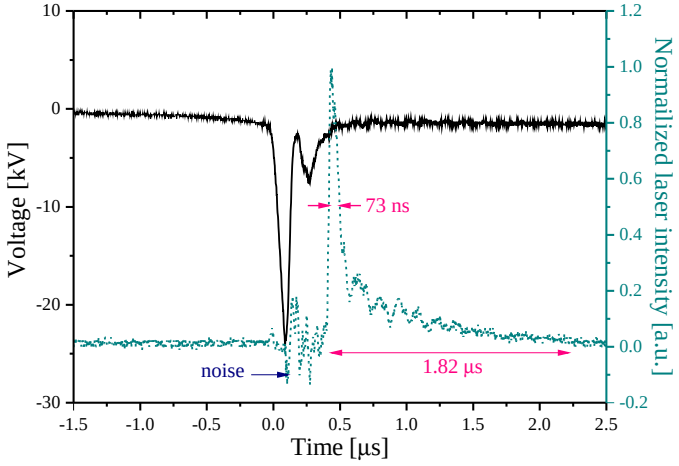

Figure 6.6: *Typical discharge voltage and laser pulse waveforms at a gas pressure of* 1.0 bar *(He:CO_2:N_2 = 3:1:1). Solid and dashed lines represented the discharge voltage and laser pulse, respectively. The charging voltage V_c = 2.04 kV and electrode separation d = 8 mm.*

To investigate its effect on the laser discharge, the gas pressure was increased while keeping the gas mixture and charging voltage constant. Figure 6.7 shows the discharge voltage and laser pulse waveforms with a laser gas mixture of 3:1:1 (He:CO_2:N_2) and pressure of 1.5 bar. The discharge voltage reached is 29.6 kV with a rise time of 129 ns. As expected, the discharge

Stellenbosch University http://scholar.sun.ac.za

voltage increases at the high gas pressure. After the start of the main discharge, it takes 0.42 μs for the laser oscillation to build up. Under these conditions, the output pulse energy was 215 mJ. The FWHM of the initial laser pulse is 62 ns and the length of the pulse about 1.52 μs.

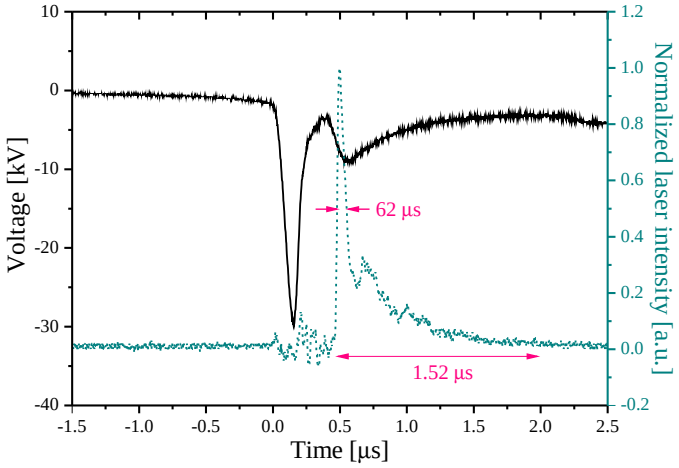

Figure 6.7: *Typical discharge voltage and laser pulse waveforms at a gas pressure of* 1.5 bar *($He:CO_2:N_2$ = 3:1:1). Solid and dashed lines represented the discharge voltage and laser pulse, respectively. The charging voltage V_s = 2.04 kV and electrode separation d = 8 mm.*

Figure 6.8 shows the discharge voltage and laser pulse waveforms with the lean gas mixture of 8:1:1 ($He:CO_2:N_2$) at a gas pressure of 1.5 bar. The discharge voltage voltage reached is 24.6 kV with a rise time of 109 ns under the same switching voltage condition as before. The discharge voltage in the lean gas mixture is lower than that in the previous case. In Figure 6.8, the laser oscillation took place after 0.51 μs from the start of the main discharge. The output pulse energy measured was 180 mJ with pulse duration of 128 ns (FWHM) and total pulse length of 1.89 μs.

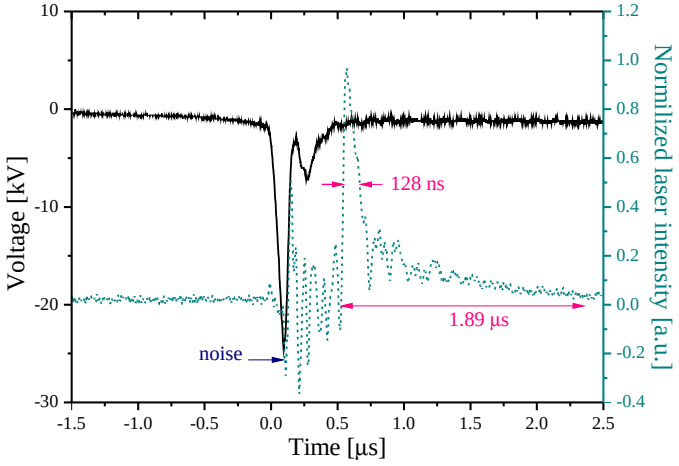

Figure 6.8: *Typical discharge voltage and laser pulse waveforms at a gas pressure of* 1.5 bar *($He:CO_2:N_2$ = 8:1:1). Solid and dashed lines represented the discharge voltage and laser pulse, respectively. The charging voltage V_c = 2.04 kV and electrode separation d = 8 mm.*

Stellenbosch University http://scholar.sun.ac.za

6.3.2 Output pulse energy and efficiency

The output performance of the laser with respect to pulse energy was monitored under different conditions. In these investigations, the laser gas mixture was replaced after every 20 min of laser operation. This way, gas degradation due to possible dissociation products and air leaks in the discharge cell can be reduced. In addition, before changing the gas mixture, the laser discharge cell was evacuated. Figures 6.9 and 6.10 show the dependence of the output pulse energy on the charging voltage at various gas pressures with laser gas mixtures 3:1:1 and 8:1:1 (He:CO_2:N_2), respectively. Overall, it can be seen that the output pulse energy increases linearly with increasing charging voltage due to the increase in the input energy. However, when the input energy was increased beyond a maximum threshold, the laser discharge tended to become unstable and at times could turn into arcs resulting in reduced energy output. Similar observations were made at very low input energies (i.e. low charging voltages).

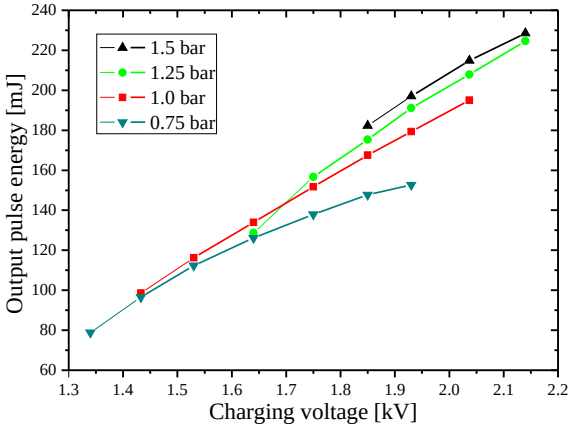

Figure 6.9: *Dependence of the output pulse energy on the charging voltage for a gas mixture of He:CO_2:N_2 = 3:1:1 at various pressures.*

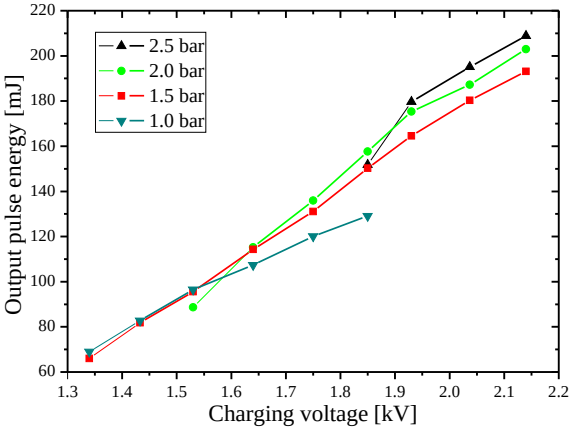

Figure 6.10: *Dependence of the output pulse energy on the charging voltage for a gas mixture of He:CO_2:N_2 = 8:1:1 at various pressures.*

Figures 6.11 and 6.12 show the electro-optical efficiency of the laser for both gas mixtures. The efficiency has been calculated with respect to the input energy E_i using the expression: $\eta = E_o/E_i = 2E_o/C_0V_0$, with E_o the output pulse energy and V_0 the charging voltage as given in Figures 6.9 and 6.10. The input storage capacitor $C_0 = 1.88\,\mu$F. As can be seen in Figures 6.11 and 6.12, the laser efficiency initially increases towards a maximum and then decreases as the input energy increases. This behaviour can be expected due to inefficient energy transfer especially at higher input energy densities. As an example, in a 3:1:1 (He:CO_2:N_2) gas mixture, the maximum efficiency which can be achieved in our parameter space is about 5.5% at a gas pressure of 1.25 bar. It should be noted, however, that the maximum extractable pulse energy at this pressure is 220 mJ and it takes place at an efficiency of 5.2%.

Figures 6.13 and 6.14 show the dependence of the output pulse energy on the gas pressure at various charging voltages. The energy output increases with increase in pressure. The

Stellenbosch University http://scholar.sun.ac.za

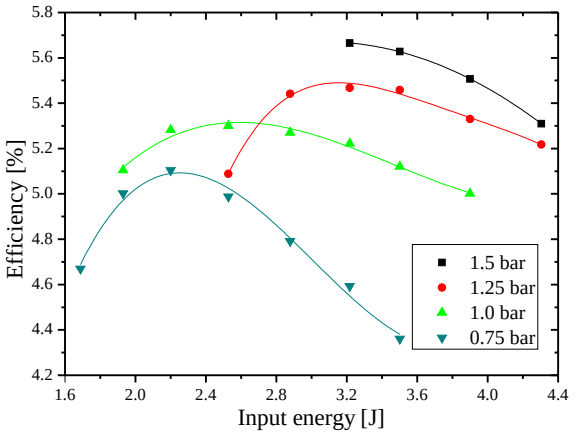

Figure 6.11: *Dependence of electro-optical efficiency on input energy for He:CO_2:N_2 = 3:1:1 gas mixture at various pressures.*

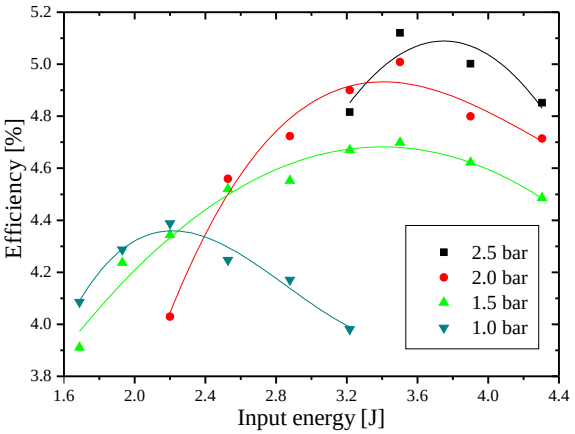

Figure 6.12: *Dependence of electro-optical efficiency on input energy for He:CO_2:N_2 = 8:1:1 gas mixture at various pressures.*

measurements were limited at the extremes of gas pressure by occasional glow-to-arc discharge formation due to lack of voltage. The maximum output energy at a charging voltage of 2.04 kV is approximately 218 mJ. The overall errors introduced by the measuring diagnostics and the numerical calculations are estimated to be around 4%.

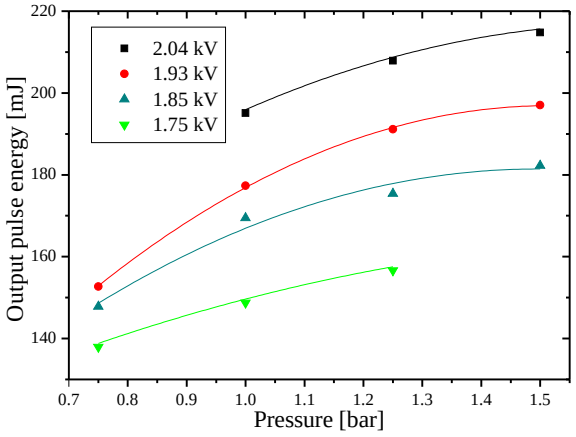

Figure 6.13: *Dependence of output pulse energy on gas pressure for He:CO_2:N_2 = 3:1:1 gas mixture at various charging voltages.*

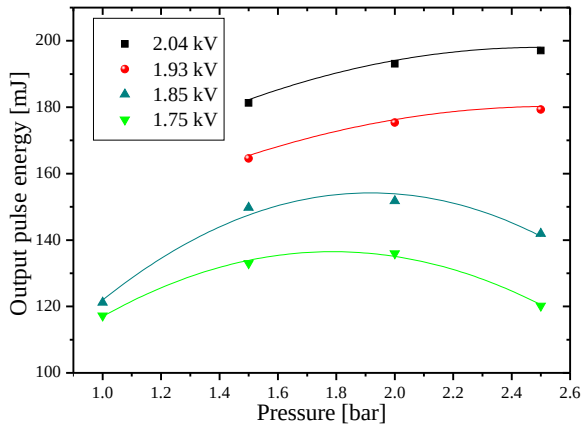

Figure 6.14: *Dependence of output pulse energy on gas pressure for He:CO_2:N_2 = 8:1:1 gas mixture at various charging voltages.*

6.3.3 Pulse repetition rate

So far, all the results presented were taken at a low pulse repetition rate of about 3 Hz. The output performance of the laser was now monitored at a pulse repetition frequency up to 250 Hz. Figure 6.15 shows the variation of the output pulse energy and average power with the pulse repetition frequency. The average power is calculated from the average laser energy per pulse

Stellenbosch University http://scholar.sun.ac.za

and the repetition rate. The measurements were taken at a gas pressure of 1.0 bar and gas mixture of He:CO_2:N_2 = 3:1:1.

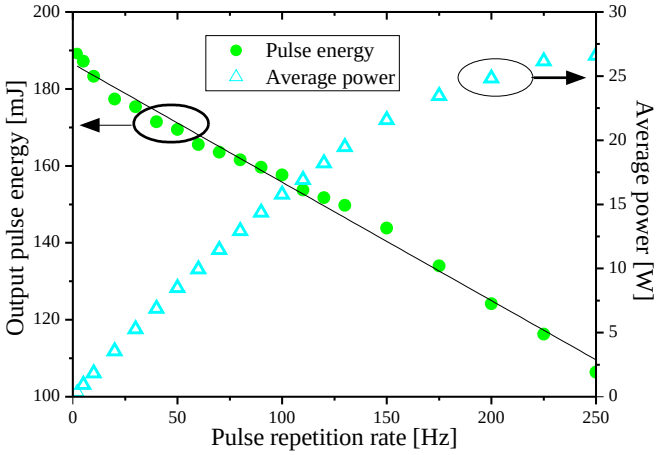

Figure 6.15: *Variation of the output pulse energy and calculated average power of the laser with the pulse repetition rate. Gas pressure* = 1.0 bar *(He:CO_2:N_2 = 3:1:1), inter-electrode separation d* = 10 mm, *input energy* = 3.5 J.

The output pulse energy decreases as the pulse repetition rate increases while the average power increases throughout. One can see that the average power increases linearly up to about 150 Hz and then starts to flatten off. The gradual reduction in the pulse energy is partly due to the inability of the excitation circuit to transfer the same amount of electrical energy to the discharge volume at higher pulse repetition rates. The other reason could be that since the laser does not have a catalytic converter, the dissociated CO_2 is not recovered, which means reduction in CO_2 in the mixture. It should be noted here that the measurements were taken in short bursts of several seconds for pulse repetition rate above 20 Hz to avoid excessive gas heating that may in turn lead to a reduced laser efficiency.

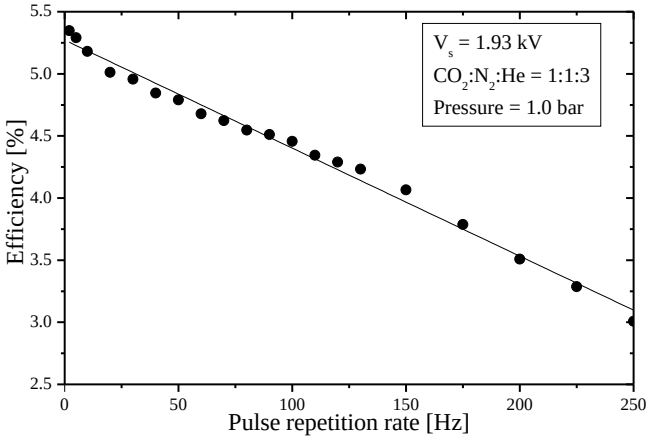

Figure 6.16: *Dependence of efficiency on the pulse repetition rate: inter-electrode separation d* = 10 mm.

Figure 6.16 shows the dependence of the electro-optical efficiency of the laser on the pulse repetition rate. The efficiency reduces as the pulse repetition rate is increased. However, it is worth noting that even up to 250 Hz, the discharge appeared to be still of very good quality.

Stellenbosch University http://scholar.sun.ac.za

6.3.4 Spark versus corona preionization

Comparison of the performance of the laser obtained here using corona preionization by double preionizer rods and measurements obtained previously with a single rod and by spark array preionization was made. Figure 6.17 shows the results obtained in all the three cases at a gas pressure of 1.0 bar (He:CO_2:N_2 = 3:1:1). The pulse energy slightly increased when two corona rods were arranged on both sides of the discharge electrodes. Moreover the discharge stability was also observed to improve.

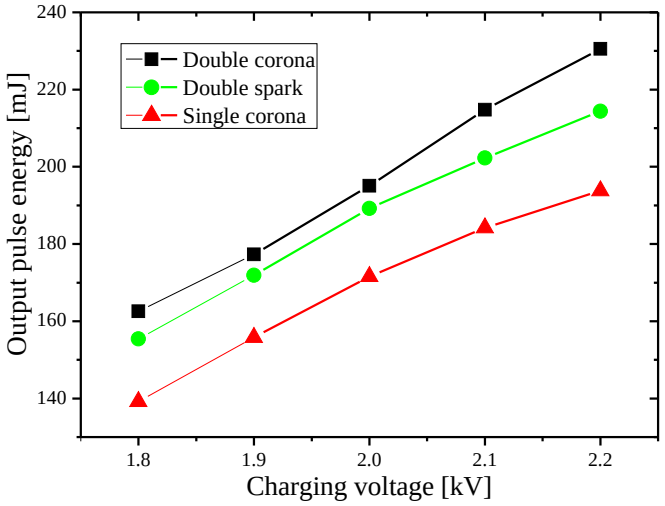

Figure 6.17: *Comparison of output pulse energy for corona and spark preionized lasers: gas pressure* = 1.0 bar *(He:CO_2:N_2 = 3:1:1), inter-electrode separation d* = 10 mm.

6.4 Summary

In this chapter, a mini TEA CO_2 laser preionized by surface-wire corona discharge has been evaluated. The corona preionization rods were constructed from ceramic tubes and a fine wire stretched along the surface of the tubes. Two laser gas mixtures were used in the experiment and as expected, more energy output was obtained with a rich gas mixture of 3:1:1 (He:CO_2:N_2) than the lean gas mixture of 8:1:1. However, a linear relation between the output pulse energy and charging voltage at various gas pressures was obtained in both gas mixtures. The laser was also operated at pulse repetition frequencies of up to 250 Hz. An increase in average power as the pulse repetition frequency increases was observed, however, at a gradual reduction in both output pulse energy and efficiency. The possible explanation for this behaviour was offered. Overall, the output performance and discharge stability with this kind of preionization system significantly improved compared to the earlier configurations using spark preionization. It can therefore be expected that if for example four corona rods would be used, more pulse energy could be extracted from the laser.

Stellenbosch University http://scholar.sun.ac.za

Chapter 7

Conclusion

7.1 Conclusion

In this thesis, the development of an efficient all solid-state switched excitation circuit for pumping a TEA CO_2 laser was described. The circuit overcomes the limitations of the thyratron-based excitation circuits. It employs an LC-inversion circuit topology with two stages of magnetic pulse compression (MPC) and a fast pulse transformer. Due to the lack of reliable data about the commercially available magnetic core materials often used in the fabrication of MPC networks and pulse transfers, three magnetic core materials were evaluated. Amongst the properties studied which are very important in magnetic switching are the magnetic flux density (ΔB) and relative permeability (μ_r). It turned out that Finemet FT-1H was the best candidate with the highest effective ΔB and μ_r as well as the lowest loss factor which means that in fact it's an efficient material. In addition, the material was available in different sizes. Therefore, because of these judicious advantages, it was used in the developments of the excitation circuit. According to the initial test measurements of the circuit with a TEA CO_2 laser head, good matching between the measured electrical parameters and the predicted numerical values was achieved. Long term tests have been conducted at the Laser Centre of Excellence (PaR systems Ltd) and the system operation is excellent even at the full pulse repetition frequency of 600 Hz.

Preionization by surface-wire corona discharge was also investigated using an existing miniature TEA CO_2 laser. The preionizer was constructed using two ceramic tubes with thin wires stretched along their length. These materials were of low-cost, making the preionization system very inexpensive. In spite of the simplicity and low-cost, when applied to the laser, the overall performance was found to improve drastically as compared to the previous measurements using a spark preionizer. In fact, pulse energies of up to 252 mJ were achieved at a pressure of 1.5 bar with a rich gas mixture. This provides additional proof that corona preionization results in superior performance compared to the conventionally employed spark preionization.

Stellenbosch University http://scholar.sun.ac.za

List of References

[1] A. J. Beaulieu. Transversely excited atmospheric pressure CO_2 lasers. *Journal of Applied Physics Letters*, 16:504–505, 1970.

[2] B.V. Kaludjerovic, M.S. Trtica, B.B. Radak, J.M. Stasic, S.S. Krstic Musovic, and V.M. Dodevski. Analysis of the interaction of pulsed laser with nanoporous activated carbon cloth. *Journal of Materials Science and Technology*, 27(11):979–984, 2011.

[3] A. Khumaeni, Z. Lie, H. Niki, K. Kurniawan, E. Tjoeng, Y. Lee, K. Kurihara, Y. Deguchi, and K. Kagawa. Direct analysis of powder samples using transversely excited atmospheric CO_2 laser-induced gas plasma at 1 atm. *Analytical and Bioanalytical Chemistry*, 400:3279–3287, 2011.

[4] C.G. Parigger, J.O. Hornkohl, and L. Nemes. Time-resolved spectroscopy diagnostic of laser-induced optical breakdown. *International Journal of Spectroscopy*, 2010:7 pages, 2010.

[5] E. Ronander and E.G. Rohwer. Multikilowatt TEA CO_2 laser system for molecular laser isotope separation. In *Proc. SPIE, 9th International Symposium on Gas Flow and Chemical Lasers*, pages 49–52, 1993.

[6] Q. Jiayin, Z. Xingshi, L. Xizhang, H. Xiao, and L. Yikun. Study on spectral characteristics and operating parameters of optically pumped NH_3 FIR cavity laser. *IEEE Journal of Quantum Electronics*, 34(1):32–39, 1998.

[7] Y. Qu, Z.H. Kang, T.J. Wang, Y. Jiang, Y.M. Andreev, and J.-Y. Gao. The detection of carbon monoxide by the second harmonic generation of CO_2 laser. *Laser Physics Letters*, 4(3):238–241, 2007.

[8] S. Dixon, C. Edwards, and S.B. Palmer. Generation of ultrasound by an expanding plasma. *Journal of Physics D: Applied Physics*, 29:3039–3044, 1996.

[9] A. Forbes, L.R. Botha, N. Du Preez, and T.E. Drake. Design and optimisation of a pulsed CO_2 laser for laser ultrasonic applications. *South African Journal of Science*, 102:75–80, 2006.

[10] H. Tanaka, A. Matsumoto, K. Akinaga, A. Takahashi, and T. Okada. Comparative study on emission characteristics of extreme ultraviolet radiation from CO_2 and Nd:YAG laser-produced tin plasmas. *Applied Physics Letters*, 87:041503, 2005.

[11] Y. Ueno, T. Ariga, G. Soumagne, T. Higashiguchi, S. Kubodera, I. Pogorelsky, I. Pavlishin, D. Stolyarov, M. Babzien, K. Kusche, and V. Yakimenko. Efficient extreme ultraviolet plasma source generated by a CO_2 laser and a liquid xenon microjet target. *Applied Physics Letters*, 90(19):191503, 2007.

[12] J. Coutouly, P. Deprez, F. Breaban, and J-P. Longuemard. Optimisation of a paint coating ablation process by CO_2 TEA laser: Thermal field modelling and real-time monitoring of the process. *Journal of Materials Processing Technology*, 209(17):5730–5735, 2009.

[13] A. Chajchir and I. Benzaquen. Carbon dioxide laser resurfacing with fast recovery. *Aesthetic Plastic Surgery*, 29:107–112, 2005.

[14] T.Y. Chang. Improved uniform-field electrode profiles for TEA laser and high-voltage applications. *Review of Scientific Instruments*, 44(4):405–407, 1973.

Stellenbosch University http://scholar.sun.ac.za

[15] G.J. Ernst. Compact uniform field electrode profiles. *Optics Communications*, 47(1):47–51, 1983.

[16] E.Y. Chu and A. Trippe. Power conditioning improves performance of discharge lasers. *Laser Focus World*, 28(2):127–134, 1992.

[17] P. K. Bhadani and R. G. Harrison. Novel discharge circuit for a multijoule TEA CO_2 laser. *Review of Scientific Instruments*, 65(3):563–566, 1994.

[18] R.S. Taylor and K.E. Leopold. Magnetic-spiker excitation of gas-discharge lasers. *Applied Physics B: Lasers and Optics*, 59:479–508, 1994.

[19] K. Yasuoka, A. Ishii, T. Tamagawa, and I. Ohshima. Newly developed excitation circuit for kHz pulsed lasers. In *Proc. SPIE, Gas and Metal Vapor Lasers and Applications*, volume 1412, pages 32–37, 1991.

[20] H. Hatanaka, K. Midorikawa, M. Obara, and H. Tashiro. 5 kw transversely excited atmospheric CO_2 laser driven by a solid state exciter employing insulated gate bipolar transistors. *Review of Scientific Instruments*, 64(11):3061, 1993.

[21] H. Tanaka, H. Hatanaka, M. Obara, K. Midorikawa, and H. Tashiro. High-efficiency, all-solid-state exciters for high-repetition-rated, high-power TEA CO_2 lasers. *Review of Scientific Instruments*, 61(8):2092–2096, 1990.

[22] K. Midorikawa, H. Hatanaka, M. Obara, and H. Tashiro. A 1 khz repetition-rate 500 w CO_2 TEA laser employing solid-state pulse power conditioning. *Measurement Science and Technology*, 4(3):388–391, 1993.

[23] R. Marchetti and E. Penco. A new type of corona-discharge photoionization source of gas lasers. *Journal of Applied Physics*, 56(11):3163–3168, 1984.

[24] A.J. Palmer. A physical model on the initiation of atmospheric pressure glow discharges. *Applied Physics Letters*, 25(3):138–149, 1974.

[25] P.R. Yuri. *Gas Discharge Physics*. Springer, 1991.

[26] D. Mathew. *Discharge instabilities in high-pressure Fluorine based excimer laser gas mixtures*. Phd, University of Twente, 2007.

[27] S. Suzuki, Y. Ishibashi, M. Obara, and T. Fujioka. Dependence of laser output on initial photoelectron density in TEA CO_2 laser. *Applied Physics Letters*, 36(1):26–28, 1980.

[28] C. Tallman. Preionization techniques for discharge lasers. In *Proc. SPIE, Pulse Power for Lasers II*, volume 1064, pages 2–14, 1989.

[29] R. Marchetti, E. Penco, E. Armandillo, and G. Salvetti. Ultraviolet preionized CO_2 TEA laser with high output power density utilizing nonconventional electrode profile. *IEEE Journal of Quantum Electronics*, 18(2):170–172, 1982.

[30] G.A. Mesyats, V.V. Osipov, and V.F. Tarasenko. *Pulsed Gas Lasers*. SPIE Optical Engineering Press, 1995.

[31] R.K. Garnworthy, L.E.S. Mathias, and C.H.H. Carmichael. Atmospheric-pressure pulsed CO_2 laser utilizing preionization by high-energy electrons. *Applied Physics Letters*, 19(12):506–508, 1971.

Stellenbosch University http://scholar.sun.ac.za

[32] D.J. Biswas and J.P. Nilaya. Repetitive transversely excited gas laser pulsers. *Progress in Quantum Electronics*, 26(1):1–63, 2002.

[33] H. J. J. Seguin, D. McKen, and J. Tulip. Photon emission and photoionization measurements in the CO_2 laser environment. *Applied Physics Letters*, 28(9):487–489, 1976.

[34] R. Babcock, I. Liberman, and W. Partlow. Volume ultraviolet preionization from bare sparks. *Quantum Electronics, IEEE Journal of*, 12(1):29–34, 1976.

[35] D. Basting and G. Marowsky. *Excimer Laser Technology*. Springer, 2005.

[36] Gautam C. Patil, J. Padma Nilaya, and D. J. Biswas. Repetitive operation of switchless transverse flow transversely excited atmosphere CO_2 lasers. *Review of Scientific Instruments*, 82(9):093107, 2011.

[37] H.M. von Bergmann, P. Baricholo, and T. Stehmann. Direct comparison of spark and corona preionization in a small size, solid-state switched high repetition rate CO_2 TEA laser. Unpublished, 2009.

[38] A. K. Laflamme. Double discharge excitation for atmospheric pressure CO_2 lasers. *Review of Scientific Instruments*, 41(11):1578–1581, 1970.

[39] H.M. Lamberton and P.R. Pearson. Improved excitation techniques for atmospheric pressure CO_2 lasers. *Electronics Letters*, 7(5):141–142, 1971.

[40] H. Bluhm. *Pulsed Power Systems, Principles and Applications*. Springer, Germany, 2006.

[41] W.S. Melville. The use of saturable reactors as discharge devices for pulse generators. In *Proceeding of IEE Radio Section*, volume 98, pages 185–204, 1951.

[42] J. Choi. Introduction of the magnetic pulse compressor (MPC), fundamental review and practical application. *Journal of Electrical Engineering and Technology*, 5(3):484–492, 2010.

[43] B.W. Williams. *Principles and Elements of Power Electronics: Devices, Drivers, Applications and Passive Components*. B W Williams, 2006.

[44] K. Takayama. *Induction Accelerators*. Springer, 2011.

[45] C.H. Smith. Applications of amorphous magnetic materials at very-high magnetization rates (invited). *Journal of Applied Physics*, 67(9):5556–5561, 1990.

[46] S. Nakajima, S. Arakawa, Y. Yamashita, and M. Shiho. Fe-based nanocrystalline FINEMET cores for induction accelerators. *Nuclear Instruments and Methods in Physics Research Section A: Accelerators, Spectrometers, Detectors and Associated Equipment*, 331(3):318–322, 1993.

[47] Hitachi. *Nanocrystalline soft magnetic material, Catalog No. HL-FM-9-C, Hitachi Metals*. 2007.

[48] C.T. Mclyman. *Transformer and Inductor design*. Marcel Dekker, 3rd edition, 2004.

[49] P.H. Swart and H.M. von Bergmann. Spreedsheet design, numerical simulations and practical evaluation of a lossy pulse compressor. In *Proc. 6th IEEE Pulsed Power Conference*, pages 680–683, 1987.

[50] H.M. von Bergmann. *Laser techniques lecture notes*. University of Stellenbosch, 2011.

Stellenbosch University http://scholar.sun.ac.za

[51] H.M. von Bergmann and T. Stehmann. Energy efficiency of the lossy series magnetic pulse compressor. In *SAIP Conference*, 2002.

[52] S.V. Nakhe, B.S. Rajanikanth, and R. Bhatnagar. Energy deposition studies in a copper vapour laser under different pulse excitation schemes. *Measurement Science and Technology*, 14(5):607–612, 2003.

[53] H.M. von Bergmann. Design of high power CO_2 TEA lasers and applications. *AIP Conference Proceedings*, 1047(1):42–47, 2008.

[54] M.J. Torkamany, M. Kavian, and M. Zand. Experimental study of sealed off operation of a high repetition rate TEA CO_2 laser. *Laser Physics Letters*, 3:480–484, 2006.

[55] I. Druckmann, S. Gabay, and I. Smilanski. A new algorithm for the design of magnetic pulse compressors. In *Conference Record of the Twentieth Power Modulator Symposium*, pages 213–216, 1992.

[56] D.P. Kumar, S. Mitra, K. Senthil, D.K. Sharma, R.N. Rajan, A. Sharma, K.V. Nagesh, and D.P. Chakravarthy. A design approach for systems based on magnetic pulse compression. *Review Of Scientific Instruments*, 79(4):045104, 2008.

[57] R. Burdt and R.D. Curry. Magnetic core test stand for energy loss and permeability measurements at a high constant magnetization rate and test results for nanocrystalline and ferrite materials. *Journal of Applied Physics*, 79(9):094703, 2008.

[58] K. McDonald, R. Curry, R. O'Connell, P. Melcher, R. Ness, and C. Huang. Evaluation of magnetic materials and insulation systems for repetition-rate pulse compression applications. In *Pulsed Power Conference, 2003. Digest of Technical Papers. PPC-2003. 14th IEEE International*, volume 1, pages 603–606, 2003.

[59] M. Watanabe, M. Nakajima, M. Shiho, K. Horioka, K. Takayama, and J. Kishiro. Magnetic core characteristics for high rep-rate induction modulator. *Review of Scientific Instruments*, 73(4):1756–1760, 2002.

[60] M. Greenwood, J. Gowar, and B.M. Bird. A comparability parameter for amorphous magnetic materials. In *1989 7^{th} IEEE International Pulsed Power Conference Digest of Technical papers*, pages 186–189, 1989.

[61] N. C. Du Prez and H. M. von Bergmann. SSS R & D project update report. Private and confidential communication, PAP Systems Centre of Excellence for SDI lasers, 2012.

[62] T. Stehmann. Development and Optimisation of a Solid-state Pulsed Power Supply for a CO_2 TEA Laser. Master's thesis, University of Stellenbosch, 2003.

[63] E.A. Stappaerts. A novel analytical design method for discharge laser electrode profiles. *Applied Physics Letters*, 40(12):1018–1019, 1982.